ANALYSIS OF CERVICAL TUMOR METABOLISM AND DESIGN OF MAGNETIC RESONANCE IMAGING SEQUENCES FOR ABDOMINAL AND PELVIC TISSUE/TUMOR HYPOXIA STUDIES

APPROVED BY SUPERVISORY COMMITTEE

_____
Roderick W. McColl, Ph.D. (Mentor)

_____
Ralph P. Mason, Ph.D.

_____
Dawen Zhao, M.D. PH.D.

_____
Robert Lenkinski, Ph.D.

_____
Matthew A. Lewis, Ph.D. (Chairman)

DEDICATION

I would like to thank my mentor Dr. Roderick McColl for his help and support for my thesis research work. I also want to thank Dr. Paul Weatherall, the former director of Rogers MR Imaging Center, for his consistent help and support since the first day I joined in Rogers center. I want to appreciate the members of my Graduate Committee for their support and guidance and all the people and my family who have given me help, especially those who shared my happiness and sadness.

This research was supported in part by The Mary Kay Ash Foundation and Harold C Simmons Cancer Center through 1 P30 CA142543.

ANALYSIS OF CERVICAL TUMOR METABOLISM AND DESIGN OF MAGNETIC RESONANCE IMAGING SEQUENCES FOR ABDOMINAL AND PELVIC TISSUE/TUMOR HYPOXIA STUDIES

By

Yao Ding

DISSERTATION

Presented to the Faculty of the Graduate School of Biomedical Sciences

The University of Texas Southwestern Medical Center at Dallas

In Partial Fulfillment of the Requirements

For the Degree of

DOCTOR OF PHILOSOPHY

The University of Texas Southwestern Medical Center at Dallas

Dallas, Texas

December, 2012

ANALYSIS OF CERVICAL TUMOR METABOLISM AND DESIGN OF MAGNETIC RESONANCE IMAGING SEQUENCES FOR ABDOMINAL AND PELVIC TISSUE/TUMOR HYPOXIA STUDIES

Yao Ding, Ph.D.

The University of Southwestern Medical Center at Dallas, Dec 2012

Supervising Professor: Roderick W. McColl, Ph.D.

Tumor oxygenation is increasingly recognized as an important factor to enhance the efficacy of chemo- and radiotherapy. MRI is becoming a widely accepted diagnostic imaging modality for investigation of tumor oxygenation. Research to improve the effectiveness of MR techniques for detection of oxygenation biomarkers (T_1 and T_2*) in the tissue/tumor hypoxia studies mainly includes efforts to improve sensitivity, efficiency and accuracy of measurements and to minimize scan duration. This dissertation mainly focuses on the

development of novel combined multi-parametric techniques to obtain both BOLD and TOLD images simultaneously.

A novel approach (ms-mGEPI-$T_{1,2*}$) is developed to simultaneously measure both T_1- and T_2*-weighted signal changes, as well as and T_1- and T_2*-maps serially during a single dynamic MRI scan. This method has also been validated in both phantom and human abdominal tissue experiments and both in vitro and in vivo results are in good agreement with those obtained using conventional methods and the literature. The ms-mGEPI-$T_{1,2*}$ has been found to provide sensitive BOLD and TOLD responses under an oxygen challenge.

Two enhanced versions of the ms-mGEPI-$T_{1,2*}$ technique with higher temporal resolution (SR-based sequence) or more accurate relaxation time estimation (IR-based sequence) are developed and validated in phantom and 3 volunteer studies. Relaxation times measured by these novel methods were in good agreement with those obtained using conventional pulse sequences. A pulse sequence which combines all three methods was developed for use on Philips MR user interface and has great potential in clinical MR examinations.

TABLE OF CONTENTS

PRIOR PUBLICATIONS

Journal

1. Peng Q, McColl RW, **Ding Y**, Wang J, Chia JM, Weatherall PT. Automated Method For Accurate Abdominal Fat Quantification On Water-Saturated Magnetic Resonance Images. J Magn Reson Imaging. 2007 Sep; 26(3): 738-46
2. Geethanath S, Baek H, Ganji S, **Ding Y**, Maher E, Sims R, Choi C, Lewis M, Kodibagkar V. Compressive sensing could accelerate ^{1}H MR metabolic imaging in the clinic. Radiology 2012; 262(3):985-994
3. Hallac RR, **Ding Y**, Yuan Q, McColl RW, Lea J, Sims RD, Weatherall PT, Mason RP. Oxygenation in Cervical Cancer and Normal Uterine Cervix assessed using BOLD MRI at 3 T. NMR in Biomedicine 2012; 25(12): 1321-30
4. **Ding Y**, McColl RW, Mason RP, Yuan Q, Hallac RR, Lea J, Sims RD, Weatherall PT. Simultaneous Measurement of TOLD and BOLD Effects in Abdominal Tissue Oxygenation Level Studies, JMRI (in revision)

Abstracts:

1. Weatherall PT, Peng Q, **Ding Y**, McColl RW, Tripathy D, Chia JM, Mason RP. "Breast Cancer Evaluation using Diffusion Weighted MR-Imaging – Prior to and Following Chemotherapy Can DWI Predict Chemotherapeutic Response", ISMRM 14th, Seattle, WA, 2006: 2880.
2. Weatherall PT, **Ding Y**, DeFatta AL, Peng Q, Adams W. "Measurement of Breast

Prosthesis Contour Irregularities", ISMRM 15th, Berlin, Germany, 2007: 2797.

3. **Ding Y**, Zhou A, McColl RW, Weatherall PT, Peng Q. "RF Phase-Cycling Water-Saturated 3D b-SSFP for Fast Abdominal Fat Imaging", ISMRM 16th, Toronto, Ontario, Canada, 2008: 1387.
4. Zhou A, **Ding Y**, McColl RW, Weatherall PT, Peng Q. "Fully-Automated Abdominal Fat Quantification on Water-Saturated MRI", ISMRM 16th, Toronto, Ontario, Canada, 2008: 1518.
5. Peng Q, Zhou A, **Ding Y**, McColl RW, Weatherall PT. "Visceral Fat Quantification on MRI: The Impact of Partial Volume Effect", ISMRM 16th, Toronto, Ontario, Canada, 2008: 3042.
6. **Ding Y**, Sims RD, Lea J, Weatherall PT, Mason RP. "Assessment of Radiotherapy Treatment in Cervical Cancer Using Proton Magnetic Resonance Spectroscopy At 3 Tesla: A Pilot Study", ISMRM 17th, Honolulu, HI, 2009: 4212.
7. **Ding Y**, Mason RP, Yuan Q, Hallac RR, McColl RW, Sims RD, Weatherall PT. "Interleaved T1- and T2*-weighted Imaging Can Evaluate Dynamic Oxygen Challenge: A Feasibility Study," ISMRM 18th, Stockholm, Sweden, 2010: 1094.
8. Yuan Q, **Ding Y**, Hallac RR, Weatherall PT, Sims RD, Boike T, Timmerman R, Mason RP. "Feasibility of BOLD Magnetic Resonance Imaging of Lung Tumors at 3T", ISMRM 18th, Stockholm, Sweden, 2010: 1093.
9. Hallac RR, **Ding Y**, Yuan Q, McColl RW, Lea J, Sims RD, Weatherall PT, Mason RP. "Oxygenation in Cervical Cancer and Normal Uterine Cervix assessed using BOLD MRI at 3 Tesla: Initial Experiences", ISMRM 18th, Stockholm, Sweden, 2010:

163.

10. **Ding Y**, Yuan Q, Hallac RR, Mason RP, McColl RW, Sims RD, Weatherall PT. "Interleaved T1- and T2*-mapping for Dynamic Abdominal Tissue Oxygenation Applications", ISMRM 19th,Montreal, Quebec, Canada, 2011: 2951.
11. Geethanath S, Baek H, Ganji S, **Ding Y**, Sims RD, Choi C, Kodibagkar VD. "Fast 1H metabolic imaging of cancer", ISMRM 19th, Montreal, Quebec, Canada, 2011: 145.
12. **Ding Y**, McColl RW, Mason RP, Sims RD, Lea J, Weatherall PT. "Quantification of Cervical Tumor Choline Concentration by Proton MR Spectroscopy at 3 Tesla: a Pilot Study", ISMRM 20th, Melbourne, Australia, 2012: 4398.

LIST OF FIGURES

LIST OF TABLES

LIST OF APPENDICES

LIST OF DEFINITIONS

MRI – Magnetic Resonance Imaging

BOLD – Blood Oxygen Level Dependent

TOLD – Tissue Oxygen Level Dependent

SI – Signal intensity

B0 – the main magnetic field

B1 – Radio frequency

Cho – Choline

Lac – Lactate

T_1 – Longitudinal relaxation; Spin–lattice relaxation

T_2 – Transverse relaxation; Spin-spin relaxation

T_2* – Effective transverse relaxation

PaO_2 – Arterial partial pressure of oxygen

SaO_2 – Arterial oxyhemoglobin saturation

SvO_2 – Venous oxyhemoglobin saturation

PO_2 – Partial pressure of oxygen

DCE – Dynamic contrast enhancement

IR HASTE – Inversion recovery half-Fourier single shot turbo spin echo

TSE – Turbo spin echo scan

GRE – Gradient-recalled echo

bSSFP – the balanced steady-state free precession

TE – Echo time

ΔR_1 – The change in the longitudinal relaxation rate

ΔR_2* – The change in effective transverse relaxation rate

2D – Two-dimensional

TI – Inversion time

SPGR – Spoiled gradient recalled echo

FA – Flip angles

2D SS-EPI – 2D single shot EPI

SV – Single-voxel

HIPAA – The Health Insurance Portability and Accountability Act

IRB – The Institutional Review Board

PRESS – Point-resolved spectroscopy sequences

CHESS – Chemical shift selective saturation

BASING – Band selective inversion with gradient dephasing

FID – Free induction decays

VOI – Volume of interest

FWHM – Full width at half-maximum

SCC – Squamous cell carcinoma

DCE-MRI – Dynamic contrast-enhanced magnetic resonance imaging

ms-mGEPI-$T_{1,2^*}$ – multi-shot multiple gradient-echo EPI sequence to acquire interleaved

T_1 and T_2* maps

VEGF –Vascular endothelial growth factor

HIF – Hypoxia inducible factor

CHAPTER ONE

OVERVIEW

1.1 Introduction

Tumor oxygenation is increasingly recognized as an important factor to enhance the efficacy of chemo- and radio-therapy (Hall 1994). The presence of hypoxia, or low oxygen concentration, in tumor cells is considered to be one of the major reasons for failure to control tumors, because ionizing radiation and some chemotherapeutic agents are less effective at low oxygen levels (Thomlinson and Gray 1955; Tatum, Kelloff et al. 2006). In order to tailor therapy to allow for hypoxia, or indeed to exploit hypoxia in therapy, there is a clear need to develop markers that reveal the presence and temporal spatial extent of hypoxia. With the development of both advanced hardware and imaging techniques (pulse sequences) on modern MR scanners, MR techniques are playing an increasingly important role for investigation of tumor oxygenation on both diagnostic and therapeutic purposes. Research to improve the effectiveness of MR techniques for detection of oxygenation biomarkers (T_1 and T_2*) in the tissue/tumor hypoxia studies mainly includes efforts to improve sensitivity and accuracy of measurements (enhanced contrast change, reduced artifacts and distortion) and to minimize scan duration (high temporal resolution). My thesis will mainly focus on combined multi-parametric techniques for oxygen-sensitive MR imaging to obtain both BOLD and TOLD images. Correspondingly, two novel oxygen-

sensitive multi-parametric MR imaging techniques will be discussed in detail. In addition to create BOLD and TOLD quantification images (T_1 and T_2* maps) in an interleaved mode, the first technique, an IR-based multi-parametric imaging technique, employs inversion recovery technique to magnify oxygen-induced TOLD contrast changes, and the second technique, a SR-based multi-parametric imaging strategy, provides higher temporal resolution. Additionally, a quantitative strategy for estimation of total choline compound (tCho) levels in malignant cervical tumors by ^{1}H MRS will also be discussed. Both phantom and human experiments will be performed to validate the feasibility of these multi-parametric imaging techniques in tissue/tumor oxygenation studies.

1.2 Outline

Some basic principles about physiology and measurement methodologies of tissue/tumor oxygenation are briefly discussed in Chapter 2. The main contribution of this thesis is divided into three parts. First, the feasibility of measuring the concentration of tCho by ^{1}H MRS is established and validated in human cervical cancer studies, which is covered in Chapter 3. Second, an interleaved BOLD and TOLD sequence programmed under Philips pulse programming environment and validated in phantom and human kidney studies under an oxygen challenge is discussed in Chapter 4. Third, two enhanced versions of this new technique with higher temporal resolution are proposed, and validated in phantom and human abdominal experiments without oxygen challenge. This is discussed in Chapter 5.

This thesis is organized as follows:

Chapter 2: Introduction

Basic concepts of physiology of tissue oxygenation and tumor hypoxia are explained. To provide a foundation for the following chapters, a brief discussion of traditional tumor oxygenation measurement methods and principles, including the electrode pO_2, the oxygen-sensitive MRI and the hypoxic-related biomarker MRS, is also presented.

Chapter 3: tCho Level Quantification in Cervical Tumors

An absolute quantification MRS method for the determination of tCho concentration in cervical tumors is employed. First, phantom studies are performed with known tCho concentrations to validate the quantification procedure. Second, in order to correct for relaxation time effects, *in vivo* T_1 and T_2 relaxation times of tCho in the normal cervix system at 3T are determined. Third, the quantification procedure is tested in a group of cervical cancer patients to obtain tumor tCho concentration changes after therapy. Moreover, the measurement of relaxation time rate changes under oxygen challenges is performed on cervical tumors.

Chapter 4: BOLD/TOLD MRI: Method Validation

A novel approach is presented to simultaneously measure both T_1- and T_2*-weighted signal changes, as well as and T_1- and T_2*-maps serially during a single dynamic MRI scan with respect to an oxygen challenge. This respiratory-triggered, free-breathing, interleaved TOLD and BOLD acquisition technique was validated on phantoms and 7 healthy volunteers with respect to oxygen breathing challenge. Measurements of both in vitro and in vivo

relaxation times were in good agreement with those obtained using conventional pulse sequences and the literature. The interleaved sequence was able to measure oxygen-induced contrast/relaxation time changes in human abdominal organs.

Chapter 5: BOLD/TOLD MRI: Rapid Acquisition Strategies

Two enhanced versions of this new technique with higher temporal resolution are developed and validated in phantom and 3 volunteer experiments without oxygen challenge. Relaxation times measured by the new methods were in good agreement with those obtained using conventional pulse sequences. A pulse sequence which combines all the new methods was developed under the Philips MR pulse programming system.

Chapter 6: Summary and Future Directions

The work presented in the previous chapters is summarized with recommendations for future directions in each area.

CHAPTER TWO

INTRODUCTION

2.1 Physiology of Tissue Oxygenation

Oxygen is fundamental in maintaining cellular vitality. Tissue oxygenation is an important physiological parameter and may also be an indicator of tissue perfusion and metabolism. In the respiratory cycle, most oxygen molecules quickly enter the red blood cells and bind to hemoglobin molecules, and only a small fraction of oxygen molecules (~1.5%) is freely dissolved in the arterial plasma. The dissolved and hemoglobin-bound oxygen are in dynamic equilibrium such that higher concentration of dissolved oxygen leads to increased oxyhemoglobin saturation. Normal subjects breathing room air (approximately 21% O_2) have around 98% arterial oxyhemoglobin saturation (SaO_2) and 70% venous oxyhemoglobin saturation (SvO_2) (West 2005). According to the characteristic sigmoid shape of the oxyhemoglobin dissociation curve (Figure 2.1) (Sidwell, Munch et al. 1938), changing the breathing gas to 100% oxygen has an evident effect on SvO_2, which rises to 80% in healthy subjects compared with little or no effect on the SaO_2. However, since the arterial partial pressure of oxygen (PaO_2), which is directly proportional to the concentration of dissolved oxygen, closely matches the partial pressure of alveolar oxygen (PO_2), a six-fold increase in the concentration of dissolved oxygen in arterial plasma occurs during inhalation of 100% oxygen (Roughton and Severinghaus 1973), while the amount of free oxygen in venous plasma only increases by 20%. The presence of controlled changes in SvO_2 in venous

systems and dissolved oxygen in arterial systems due to the modulation of hyperoxic gas inhalation has been utilized to investigate blood/tissue oxygenation in various in vivo studies, such as brain functional studies (Ogawa, Tank et al. 1992), myocardial studies (Li, Dhawale et al. 1996), kidney functional studies (Sadowski, Fain et al. 2005) and tumor hypoxia studies (Howe, Robinson et al. 2001).

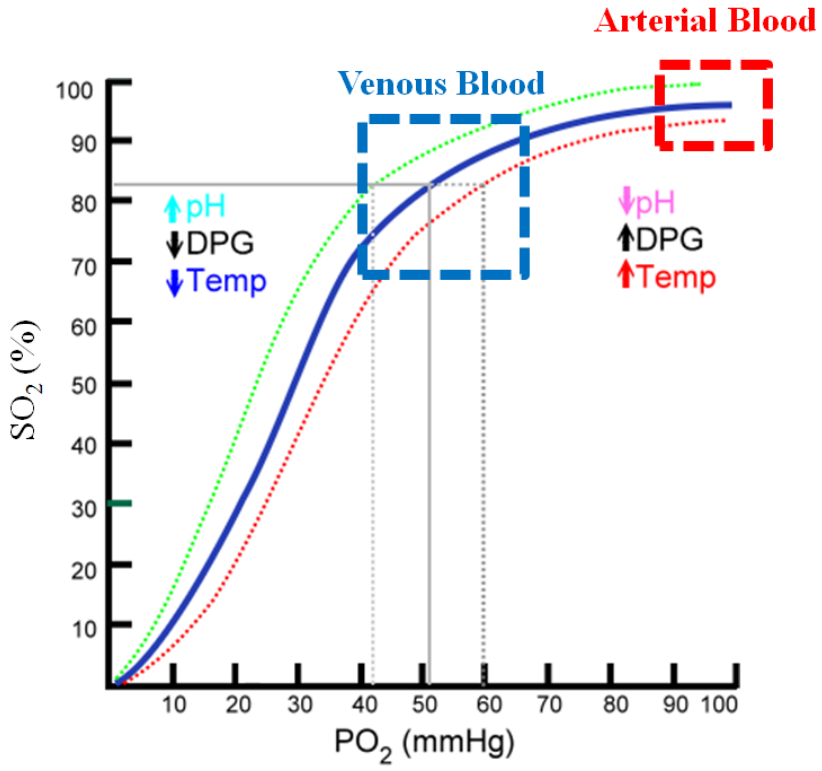

Figure 2.1 A basic oxy-hemoglobin dissociation curve.

2.2 Hypoxia in Tumors

Hypoxia is a pathological condition in which tissues lack the oxygen supply for cells to metabolize normally. Hypoxic areas occur as a result of an imbalance between the supply and consumption of oxygen. In normal tissue, the oxygen supply matches metabolic requirements. However, in up to 50-60% of locally advanced solid tumors, the oxygen consumption rate of tumor cells may exceed the oxygen supply which may then exhibit locally low oxygen levels (Vaupel and Mayer 2007). Hypoxia in solid tumors is mainly due to rapid proliferation and vascular abnormalities (Hu and Polyak 2008). Tumor microvessels have severe structural and functional abnormalities which lead to perfusion-limited oxygen delivery (Fukumura and Jain 2007). This type of hypoxia is usually transient and therefore, also called "acute hypoxia". Correspondingly, expanded diffusion distances in tumors may also limit oxygen and nutrients delivery and then cause "diffusion-limited hypoxia", also called "chronic hypoxia" (Vaupel and Mayer 2007). More factors such as adverse diffusion geometry and tumor-associated and/or therapy-induced anemia may also cause hypoxia. In solid tumors, hypoxia has been shown to have two contrasting aspects. On the one hand, it is associated with restrained proliferation and with differentiation, apoptosis, and necrosis. On the other hand, it stimulates adaptive processes leading to tumor aggressiveness, progression, and acquired resistance to treatment (Tatum, Kelloff et al. 2006).

2.2.1 Hypoxia in Tumor Biology

Adaptation to tumor hypoxia results in the transcriptional induction of a series of genes that participate in angiogenesis (Carmeliet, Dor et al. 1998), glucose metabolism (Seagroves, Ryan et al. 2001), and cell proliferation/survival (Feldser, Agani et al. 1999). The primary

factor mediating these responses is the hypoxia inducible factor 1 (HIF-1), an oxygen-sensitive transcriptional activator (Seagroves, Ryan et al. 2001). HIF-1 consists of a constitutively expressed subunit HIF-1β and an oxygen-regulated subunit HIF-1α (or its paralogs HIF-2α and HIF-3α). The HIF-1, specifically the HIF-1α (Zhong, De Marzo et al. 1999), activates genes involved in increasing oxygen delivery in cells under hypoxic conditions (Wang, Jiang et al. 1995) or in helping cells to survive oxygen deprivation (Semenza 1999). Under normoxic conditions, HIF-1α is rapidly degraded by the ubiquitin-proteasomal pathway, whereas exposure to hypoxia prevents its degradation (Salceda and Caro 1997; Huang, Gu et al. 1998). Overexpression of HIF-1α and HIF-2α has been found in various human cancers, probably as a consequence of intratumoral hypoxia or genetic alteration (Zhong, De Marzo et al. 1999). Immunohistochemical analyses demonstrated that there are detectable levels of HIF-1α protein in benign tumors, elevated levels in primary malignant tumors, and a marked amount in tumor metastases, in contrast to its absence in normal tissues (Zhong, De Marzo et al. 1999; Harris 2002). Moreover, HIF-1α effects may combine with other changes in gene expression in cancer cells. For example, in early stage cancer, hypoxia may exert its effects through HIF-1α, but in later stages, additional genetic alterations may lead to constitutive activation of HIF-1α, as well as other pathways, in the absence of hypoxia (Krieg, Haas et al. 2000; Brune and Zhou 2003; Wakisaka and Pagano 2003).

2.2.2 Warburg Effect

In 1920s, Warburg discovered that in contrast to normal cells, which rely primarily on oxidative phosphorylation to generate the energy needed for cellular processes, most cancerous cells instead rely on aerobic glycolysis (Warburg 1956). The recent investigations of HIF-1α have implicated a possible molecular mechanism for the Warburg effect in malignant tumors (Semenza and Wang 1992; Seagroves, Ryan et al. 2001). HIF-1α combines with HIF-1β to form a heterodimeric transcription factor that regulates the expression of glycolytic and angiogenic proteins. Overexpression of HIF-1α in malignant tumor cells stimulates some of the cellular adaptations including the upregulation of red blood cell production (Bartrons and Caro 2007), increased transcription of vascular endothelial growth factor (VEGF) (Bartrons and Caro 2007), and increased production and membranal localization of a glucose transporter, GLUT-1 (Chen, Pore et al. 2001). The greater rate of aerobic glycolysis and lower rate of oxidative respiration in tumor cells leads to increased intracellular levels of glycolytic metabolites, specifically pyruvate (Warburg 1956). Pyruvate promotes the production and stability of HIF-1α thus creating a positive feedback loop that bolsters the proliferation of cancer cells (Lu, Forbes et al. 2002). Recently, it was calculated that 62% of all known cancers show a Warburg effect (Altenberg and Greulich 2004).

2.2.3 Radioresistance of Hypoxic Tumor Cells

Tumor hypoxia is a well-established and accepted mechanism of radioresistance and correlates with treatment failure in radiation therapy (Brizel, Sibley et al. 1997). The radioresistance of cancer cells is influenced by both oxygen concentrations , “DNA damage repair pathway” (Bindra, Crosby et al. 2007), and HIF-1 activity, “cell death/survival

signaling pathway" (Harada and Hiraoka 2010). Radiation chemistry studies have elucidated that the depletion of oxygen results in the inefficient formation of DNA strand breaks by ionizing radiation, and moreover, prevents the damage from being repaired (Thomlinson and Gray 1955; Brown and Wilson 2004). Therefore, DNA damage, especially irreparable double stranded breaks, is significantly less severe in the absence of molecular oxygen, leading to hypoxia-related radioresistance of cancer cells.

Meanwhile, radiation biology studies have revealed that HIF-1 plays a pivotal role in hypoxia-related tumor radioresistance (Moeller, Cao et al. 2004; Moeller and Dewhirst 2006; Harada and Hiraoka 2010). An attractive model of this role was proposed and supported recently; 1) radiation activates HIF-1 in a solid tumor, 2) HIF-1 induces the expression of VEGF which protects endothelial cells from the cytotoxic effects of radiation, and 3) the radioprotected tumor blood vessels assure the supply of oxygen and nutrients to tumor cells and promote tumor growth (Gorski, Beckett et al. 1999; Moeller, Cao et al. 2004; Zeng, Ou et al. 2008; Harada, Itasaka et al. 2009). Thus, hypoxic tumor cells have been recognized as a major obstacle to radiation therapy (Brown and Wilson 2004).

2.2.4 Hypoxia in Cervical Tumor Therapy

In cancer patients, hypoxia may predict response to treatment and ultimately the outcome of the disease. The most extensive studies have been applied to cervical cancer, revealing both extensive hypoxia and more rapid rates of recurrence for large hypoxic tumors in node negative patients (Hockel, Schlenger et al. 1996; Rofstad, Sundfor et al. 2000; Fyles, Milosevic et al. 2002). Patients with recurrent cervical cancer experience dismal survival

rates, and therefore there is a need to measure tumor hypoxia in assessing the aggressiveness of tumor and predicting the outcome of therapy.

2.3 Measuring Tumor Hypoxia

A number of invasive and minimally invasive techniques have been exploited to measure tissue/tumor oxygenation, including polarographic needle electrodes (Hockel, Vorndran et al. 1993; Brizel, Sibley et al. 1997), immunohistochemical (IHC) staining (Evans and Koch 2003; Ljungkvist, Bussink et al. 2007), radionuclide imaging (positron emission tomography [PET] (Rasey, Koh et al. 1996) and single-photon emission computed tomography [SPECT] (Davda and Bezabeh 2006)), MRI (Zhao, Jiang et al. 2009; Padhani 2010), optical imaging (bioluminescence and fluorescence) (Harada, Kizaka-Kondoh et al. 2005; Zhao, Jiang et al. 2009), and so on.

2.3.1 Gold Standard Method

Being regarded as the clinical gold standard for many years, the invasive polarographic electrode pO_2 measurements have been extensively used in easily accessible tumors such as head and neck cancer, cervical cancer, prostate cancer, and breast cancer (Hockel, Vorndran et al. 1993; Powell, Collingridge et al. 1999; Nordsmark and Overgaard 2000). These measurements have been used to develop profiles that can be illustrated by pO_2 histograms reflecting the oxygenation status of a given tissue. The average pretreatment median pO_2 was

11.2 mmHg (range 0.4-60 mmHg) (Brizel, Sibley et al. 1997), and values obtained by such measurements can predict treatment response and the metastatic potential of tumors.

Tumor hypoxia is a spatially and temporally heterogeneous phenomenon, resulting from the combined effect of many factors, including tumor type and volume, disease site (specific organ or tissue), regional microvessel density, blood flow, oxygen diffusion and consumption rates (Serganova, Humm et al. 2006). Although the polarographic electrode can provide relatively accurate measurement of tumor oxygenation, insertion of an electrode into the tumor disrupts tissues and only identifies partial information in the whole tumor region. Moreover, this technique has selection bias and therefore requires great expertise and has a large interobserver variability and cannot measure change during oxygen challenges. Recent reports suggest that no universal gold standard exists at present (Olive, Banath et al. 2001; Tatum, Kelloff et al. 2006).

2.4 Measuring Tumor Hypoxia - MRI Methods

There has been a growing interest in the use of noninvasive functional imaging techniques which are sensitive to tissue/tumor oxygenation, provide quantitative measurements, are clinically safe, of adequate resolution and ease of use. MR method has a potential to fulfill the majority of these requirements satisfactorily.

2.4.1 Mechanisms of BOLD and TOLD

As a non-invasive imaging technique, oxygen-sensitive MR imaging has been increasingly used in clinical research to investigate neuronal activation, kidney function and tumor hypoxia (Tadamura, Hatabu et al. 1997; Howe, Robinson et al. 2001; Taylor, Baddeley et al. 2001; Jones, Ries et al. 2002; Matsumoto, Bernardo et al. 2006; Garcia-Eulate, Garcia-Garcia et al. 2011; Glover 2011). Two different mechanisms involved in oxygen-induced MR effects are: 1) tissue oxygen-level dependent (TOLD): T_1 relaxation time changes affected by paramagnetic T_1-shortening properties of molecular O_2 in tissues (Matsumoto, Bernardo et al. 2006; O'Connor, Jackson et al. 2007; O'Connor, Naish et al. 2009), and 2) blood oxygen-level dependent (BOLD): susceptibility-related T_2* increase created by decreased concentration of intravascular deoxyhemoglobin upon breathing 100% O_2 (Ogawa, Lee et al. 1990; O'Connor, Naish et al. 2009).

Paramagnetic molecular oxygen (O_2) modulates T_1 values; the presence of an increased amount of dissolved oxygen leads to a reduction in the longitudinal relaxation (T_1) of the plasma and tissue fluid and increased signal intensity on T_1-weighted sequences, but has relatively little or no effect on the effective transverse relaxation (T_2*) values (Neuhaus 1989). This effect provides a mechanism for monitoring both intravascular blood and extravascular fluid oxygenation status which are important for the effectiveness of radio- and chemo-therapy.

This approach is distinct to the BOLD mechanism of contrast. Hemoglobin, the oxygen carrier in blood, will present as deoxyhemoglobin in oxygen-deficient states. Paramagnetic deoxyhemoglobin in blood creates magnetic susceptibility gradients near blood vessels which can decrease local T_2* values in the surrounding tissues and, in turn, influence the MRI

signal of T_2*-weighted images. In tissue oxygenation studies, a reduction in the fraction of deoxyhemoglobin through breathing a hyperoxic gas leads to an increase in T_2* signal intensity in venous systems, while having little effect on T_1 (Ogawa, Lee et al. 1990). Thus, BOLD MRI contrast has been utilized to non-invasively evaluate regional blood flow and/or intravascular tissue oxygenation.

2.4.2 Qualitative BOLD and TOLD

Tissue TOLD effects can be qualitatively evaluated by analyzing signal changes in T_1-weighted MR images acquired before and during hyperoxic gas inhalation (Chen, Jakob et al. 1998; Jones, Ries et al. 2002). The SI change is calculated as:

$$\Delta SI = \frac{SI_{oxy} - SI_{air}}{SI_{air}} \times 100\% \qquad [2\text{-}1]$$

Where SI_{oxy} is the mean signal intensity with oxygen inhalation and SI_{air} is the mean baseline signal intensity during air breathing.

However, compared to T_1-weighted dynamic contrast enhancement (DCE) results, the oxygen-induced signal change is too weak to be detected using conventional T_1-weighted spin echo sequences. Therefore, an inversion recovery half-Fourier single shot turbo spin echo (IR HASTE) imaging sequence with optimal delay time has been applied in kidney and lung oxygenation investigations (Hennig and Friedburg 1988; Listerud, Einstein et al. 1992; Chen, Jakob et al. 1998; Jones, Ries et al. 2002). This approach offers magnified T_1 weighting with clinically acceptable spatial and temporal resolutions. However, only a limited range of tissue T_1 changes can be detected effectively.

BOLD effects can be observed using gradient-echo sequences. The conventional approach for detecting blood oxygenation changes with MRI is to measure signal changes (Eq. 2-1) in T_2*-weighted gradient-recalled echo (GRE) images acquired at a fixed echo time (TE) (Griffiths, Taylor et al. 1997; Rostrup, Law et al. 2000; Kastrup, Kruger et al. 2001; Baudelet, Cron et al. 2006). Higher temporal resolution can be achieved by using EPI acquisition which may produce geometric distortion (Feinberg, Turner et al. 1990; Wheeler-Kingshott, Parker et al. 2002). Recently, the balanced steady-state free precession (bSSFP) sequence has been investigated as an alternative to conventional BOLD MRI. bSSFP image has good image quality and less geometric distortion. However, the contrast of bSSFP images depends jointly on the R_1/R_2 ratio which does not typically reflect BOLD effects (Scheffler and Lehnhardt 2003), although with long TE and TR, the bSSFP signal may show a considerable T_2* contrast (Miller, Smith et al. 2007).

BOLD/TOLD contrast imaging techniques are sensitive to tissue/tumor oxygenation and can yield a series of dynamic images with adequate temporal and spatial resolutions. Analysis of contrast changes is also straightforward and effective. However those qualitative imaging methods have inherent limitations. First, the data values are MR sequence- and system-dependent and limit the reproducibility and comparability of results. Second, it is nonspecific to T_1/T_2* contrast changes, because it may also be affected by T_2*/T_1 contrast changes and inflow effects slightly. Third, only a small range of tissue T_1/T_2* contrast changes can be measured accurately. Therefore, more investigators are using quantitative MR imaging methods to measure tumor hypoxia (O'Connor, Naish et al. 2009).

2.4.3 Quantitative BOLD and TOLD

TOLD-MRI methods

In TOLD-MRI studies, the change in the longitudinal relaxation rate (ΔR_1) is proportional to the change in the tissue oxygen concentration (ΔpO_2) (Nestle, Baumann et al. 2003). Therefore, measurement of the R_1 values can reflect the tissue oxygenation level quantitatively. Various techniques have been proposed for the measurement of R_1 *in vivo*. Most are classified into two categories: 1) sampling of the saturation or inversion recovery curve with various delay times and 2) excitation using various flip angles.

Sampling of the inversion recovery curve is obtained by repeatedly performing a two-dimensional (2D) inversion recovery fast-spin sequence, e.g. IR HASTE sequence, with multiple delay times (Jones, Ries et al. 2002). Accurate T_1 maps can be generated by fitting IR HASTE image signal intensity to inversion time (TI) with the equations below.

$$M_Z(TI) = M_0\left(1 - 2 \cdot e^{-TI/T_1}\right) \quad [2\text{-}2]$$

$$R_1 = 1/T_1 \quad [2\text{-}3]$$

Where M_Z is the longitudinal magnetization and M_0 is the equilibrium magnetization. This method may be considered as the gold standard for computing T_1 *in vivo* (Steen, Gronemeyer et al. 1994). However it cannot be practically used for high spatial resolution and dynamic studies due to its long acquisition time and lack of three-dimensional (3D) capability. An alternative technique, i.e. saturation recovery, can reduce the acquisition time at the cost of reduced tissue T_1 contrast changes (Zaharchuk, Busse et al. 2006).

3D spoiled gradient recalled echo (SPGR) imaging with variable flip angles (FA) can be performed rapidly with a large 3D coverage (Deoni, Rutt et al. 2003). The measured SPGR signal intensity (S_{SPGR}) is a function of the longitudinal relaxation time, T_1, repetition time, TR, flip angle, α, and a factor which is proportional to the equilibrium longitudinal magnetization , M_0:

$$S_{SPGR}(\alpha) = \frac{M_0(1-E_1)\sin(\alpha)}{1-E_1\cos(\alpha)} \quad [2\text{-}4]$$

$$E_1 = e^{-(TR/T_1)} \quad [2\text{-}5]$$

By fixing TR constant and incrementally increasing α, a curve characterized by T_1 is yielded. However, this method of calculating T_1 can produce measurement errors due to inaccurate flip angles (Venkatesan, Lin et al. 1998). Moreover, insufficient spoiling of transverse magnetization after each acquisition and a noise bias for low SNR may generate considerable systematic errors in T_1 estimation (Cheng and Wright 2006; Preibisch and Deichmann 2009). Thus, additional sequences, e.g. B_1 map, are required to generate reference images to make corrections (Cheng and Wright 2006).

Several other methods for T_1 mapping have been suggested, including 2D single shot EPI (2D SS-EPI) and variants (Look-Locker EPI, IR-EPI) which achieve better spatial and temporal resolutions (Look 1970; Gowland and Mansfield 1993). However, the spatial resolution using these rapid imaging techniques is limited by susceptibility artifacts and additional corrections are required to achieve true T_1 values because of their inherent bias in data acquisition (Farzaneh, Riederer et al. 1990; Cohen and Weisskoff 1991).

BOLD MRI methods

In BOLD-MRI studies, the change in effective transverse relaxation rate (ΔR_2^*) is related to Δ[dHb] in blood (Ogawa, Lee et al. 1993) and can be obtained through monoexponential fitting of the multi-echo signal decay generated by the mGRE sequence. The equation of mGRE signal intensity (S_{mGRE}) can be simplified as the following:

$$S_{mGRE}\ (TE) = S_0 \cdot e^{-TE/T_2^*} \qquad [2\text{-}6]$$

$$R_2^* = 1/T_2^* \qquad [2\text{-}7]$$

These multiple S_{mGRE} values can be sampled in the same excitation with different TE values. Therefore, the calculation of R_2^* values is independent from R_1 changes. Compared with the T_2^*-weighted EPI sequence or bSSFP sequence which acquires multi-slice or 3D information in BOLD-MRI studies, the mGRE R_2^* quantification sequence usually produces a series of 2D maps to ensure adequate temporal resolution.

The measurement of the changes of the relaxation rate ($\Delta R_1/\Delta R_2^*$) using quantitative imaging methods overcomes the limitations of qualitative methods (Baudelet and Gallez 2002; Rijpkema, Kaanders et al. 2002; Rodrigues, Howe et al. 2004; Ziyeh, Rick et al. 2005; O'Connor, Naish et al. 2009). After subtraction of the baseline maps from the oxygen challenge maps, ideally, MR sequence- and system-dependent errors of $\Delta R_1/\Delta R_2^*$ can be cancelled out to ensure only oxygenation related information is left. However, a significant disadvantage of the BOLD/TOLD mapping techniques is their longer acquisition time, not suitable for dynamic scans, especially when such techniques are applied along with

respiratory compensation techniques, e.g. breath-hold, respiratory triggering and gating techniques found in human abdominal/pelvic organ oxygenation studies.

2.4.4 Current strategies for BOLD and TOLD

It was recently reported that measurement of R_2* alone was insufficient to reflect renal function in chronic kidney disease and thus there is increasing interest in measuring additional parameters (Michaely, Metzger et al. 2012). Concurrent use of tissue oxygen-level dependent (TOLD) and blood oxygen-level dependent (BOLD) contrast MRI may provide a more informative index of tissue oxygenation than either alone.

Recently, combined MR investigations presented both dynamic BOLD and TOLD response in animal models (rats and rabbits) showing complementary information about tumor and normal tissue oxygenation (Pacheco-Torres 2008; Winter, Akens et al. 2011). Pacheco-Torres applied two individual BOLD and TOLD weighted (T_1W and T_2*W) sequences in an interleaved mode to monitor and analyze carbogen-induced signal changes in the four different groups of tumors qualitatively. The temporal resolution was 30 sec for both BOLD and TOLD acquisitions which was adequate for investigating tumor response to hyperoxic gas breathing. In Winter's experiments, quantitative T_1 and T_2* maps calculated by SPGR and MGRE methods were collected during each gas challenge with a temporal resolution of 3 min. Mean changes in T_1 (ΔT_1) and T_2* (ΔT_2*) were calculated from regions of interest in each organ.

More recently, these principles have been applied to measure quantitative changes in brain oxygenation under respiratory challenges, using a simultaneous T_1 and T_2* mapping

method (Remmele S 2008). The combination of SPGR sequence and mGRE sequence with preceding baseline B_1 and R_1 quantification were employed to achieve simultaneous and dynamic $\Delta R_1/\Delta R_2$* estimation in brain functional MRI investigations. The technique delivered accurate ΔR_1 and ΔR_2* values with high temporal resolution (5 sec). However, when this technique is used for assessment of human abdominal/pelvic organs it may be significantly hindered by motion (respiration, peristalsis) and severe local susceptibility issues in dynamic abdominal organ oxygenation studies.

2.5 Measuring Tumor Metabolites –Choline

As an important application of MR, magnetic resonance spectroscopy (MRS) has the ability to provide chemical information about tissue metabolites (Shah, Sattar et al. 2006). Nuclei can resonate at slightly different frequencies after absorbing radio frequency in the magnetic fields, therefore MRS can be used to detect the resonance spectra of molecules revealing the chemical and molecular composition of tissues. Over the past two decades, MRS has been used extensively to investigate lesions in a number of areas including brain, breast, and prostate. (Preul, Caramanos et al. 1996; Rudkin and Arnold 1999; Del Sole, Falini et al. 2001; Katz-Brull, Lavin et al. 2002; Doran, Falk et al. 2003; Swindle, McCredie et al. 2003; Cho, Lee et al. 2005; Gluch 2005).

The Cho signal is generally unresolved with in vivo NMR and includes free choline (3.19 ppm), phosphocholine (3.21 ppm), glycerophosphocholine (3.22 ppm), phosphoethanolamine (3.23 ppm), glucose (3.24 ppm), taurine (3.25 ppm), and myo- inositol

(3.27 ppm) (Gribbestad, Sitter et al. 1999; Sitter, Bathen et al. 2004). These contributions can be separated in *ex vivo* MR studies, but *in vivo*, especially at the lower field strengths (1.5T or 3T) applied for clinical studies, these multiple resonances cannot be resolved and therefore they appear as a single peak, referred to as total choline-containing compounds (tCho). Elevation of the tCho level is believed to represent an increased biosynthesis of membrane phospholipids and to be an active marker for cellular proliferation (Ruiz-Cabello and Cohen 1992; Negendank 1995). Therefore, the tCho compounds are detected in various malignant tumors using the ^{1}H MRS technique (Longo, Pollesello et al. 1995; Mukherji, Schiro et al. 1997; Kim, Kim et al. 1998; Kvistad, Bakken et al. 1999). The primary component contribution to the elevated tCho peak is phosphocholine, a known precursor of cell membrane synthesis (Gribbestad, Fjosne et al. 1993; Ting, Sherr et al. 1996; Aboagye and Bhujwalla 1999). However, the precise cause is still being investigated. Mechanisms postulated so far include increased activity of Cho kinase (Ramirez de Molina, Rodriguez-Gonzalez et al. 2004), increased phospholipase C expression (Glunde, Jie et al. 2004), upregulated Cho transporter concentrations (Glunde, Jie et al. 2004), and increased activation of phospholipase A2 (Guthridge, Stampfer et al. 1994) and phospholipase D (Noh, Ahn et al. 2000).

Metabolism of Cho in cancer cells is known to be sensitive to its microenvironment. Some investigators also observed Cho level was decreased in hypoxic cancer cells (Hara, Bansal et al. 2006; Bansal, Harris et al. 2012). This decreased Cho accumulation is primarily due to decrease in Cho phosphorylation. Reduction in Cho kinase expression, activity, and reduced ATP levels in hypoxic cells contributes to the decrease in Cho phosphorylation.

Decreases in Cho kinase expression in hypoxia are likely mediated by HIF-1α (Bansal, Harris et al. 2012). Therefore, it is important to consider the potential impact of tumor hypoxia on Cho phosphorylation in the phospholipid synthesis pathway when choline-based cancer therapy and imaging applications are pursued.

2.6 Technical issues in MR studies

2.6.1Technical issues regarding ^{1}H MRS

Internal referencing method

A MR spectrum shows a series of peaks corresponding to different metabolites, with the integral of the peak being proportional to the actual concentration of the metabolite in the tissue. Early investigations of metabolisms such as tCho in various tumors have focused on the qualitative assessment of the presence of metabolite peaks in ROIs or a relative quantification of the metabolite of interest, e.g. reporting metabolite SNR (Allen, Prost et al. 2001; Wang, Li et al. 2004; Fayad, Bluemke et al. 2006). However, such methods are limited due to many factors, including pulse sequence efficiency, magnetic field strength, coil positioning and type, and tumor size and location.

To overcome these limitations, a number of metabolite quantification techniques have been proposed for determining metabolite concentration by MRS. These techniques involve the calibration of metabolite signals from a volume of interest (VOI) by comparison with an external or internal reference (Roth, Hubesch et al. 1989; Fatouros, Heath et al. 2000). In an external reference method, the spectra are acquired separately from the tissue and the

reference sample, e.g. a known concentration phantom, and the results are compared to estimate the concentration of the metabolite of interest. The accuracy of this method can be affected by variations in coil geometry and RF homogeneity. Moreover, the set-up of the external reference is time-consuming and labor-intensive, therefore it is impractical for clinical applications.

On the other hand, the internal referencing method relies on comparison of a known endogenous compound with a defined concentration. For example, the water peak from a non-suppressed spectrum from the same voxel can be used as an internal reference. Compared with the external referencing technique, the internal referencing method is simpler and automatically corrects for several important coil-related factors. Indeed, both methods have been utilized in brain, breast, cervix and muscle MRS (Helms 2000; Bolan, Meisamy et al. 2003; Mahon, Cox et al. 2004). The metabolite concentration can be calculated by comparing the metabolite of interest and water signal intensities with correction of the differences in relaxation time, signal averaging, and system gain. This ratio can then be converted into an arbitrary unit or a molar unit.

Fitting error estimation

The fitting error of the quantification method in MRS applications is commonly estimated using the Cramer-Rao minimum variance bound ($CRMVB_A$) of the signal amplitude (Bolan, Meisamy et al. 2003).

$$\mathrm{CRMVB_A} = \frac{\sigma^2_{\mathrm{noise}}}{\int_{\omega_0+\delta\omega}^{\omega_0-\delta\omega} \frac{\partial}{\partial A}[\mathrm{FFT}\{s_{\mathrm{model}}\ (t)\}]\mathrm{d}\omega} \qquad [2\text{-}8]$$

Where $\sigma^2_{\mathrm{noise}}$ is the variance of white, Gaussian noise. CRMVB is not actually an estimate of the fitting error, but it reflects a theoretical minimum limit for the estimation accuracy (Cavassila, Deval et al. 2001). Therefore, the error is often expressed as a normalized standard deviation (SD): $\sigma_A = \sqrt{\mathrm{CRMVB}}$ / A. This parameter estimation must not contain systematic errors, which may lead to underestimation errors. Furthermore, SNR degradation and increases in line width, which may lead to systematic errors, are not necessarily reflected in CRMVB estimates (Kreis and Boesch 2003).

Concentration expression

Some medical tests give results in millimoles per kilogram (mmol/kg). A mole is an amount of a substance that contains 6.02×10^{23} molecules or atoms and a millimole is one-thousandth of a mole. Given the weight of a mole of water is about 18.02 grams and a kilogram of water is 1000 grams, the concentration of water can be expressed as 55.5×10^3 mmol/kg. The reciprocal of this value, $MW_{H20} \approx 18 \times 10^{-6}$ kg/mmol, can be applied as a water reference parameter for the estimation of metabolite concentration (mmol/kg) in MR spectroscopy experiments. For example, choline concentrations, in units of mmol/kg, were estimated using the nonsuppressed water peak as an internal reference compound, a method described elsewhere for lesions of the breast and brain (Soher, Hurd et al. 1996; Bolan,

Meisamy et al. 2003; Baik, Su et al. 2006), and adapted for use in normal skeletal muscle with fat tissue correction (Fayad, Wang et al. 2010).

Spectrum preprocessing (truncation / zerofilling)

The receiver bandwidth (= N/T, N: number of sampling; T: period of sampling) is kept wide enough to detect all spectral frequencies, but narrow enough to minimize the noise contribution to the signal. Period T should be long enough to collect signals from the beginning of the FID but short enough to avoid collecting background noise from the end of FID. An alternative approach to increasing N in the data collection period and minimizing the noise contribution is to truncate late FID signal (truncation) and then append additional data points of zero amplitude at the end of truncated FID to improve the spectral resolution (zero-filling). If FID has not completely decayed to noise level, an abrupt change of a step in signal amplitude will occur. After Fourier transformation, a truncation artifact which appears as "wiggles" will be produced. In practice, an apodization filter will eliminate this step-like discontinuity.

2.6.2 Technical issues regarding MRI

SENSE

Parallel imaging is a technique that enables to reduce scan time in magnetic resonance imaging (MRI) considerably. Parallel imaging exploits the difference in sensitivities between individual coil elements in a receiver array to reduce conventional Fourier encoding.

Pruessmann et al. presented a general formulation and performance analysis of the image domain sensitivity encoding method (SENSE) (Pruessmann, Weiger et al. 1999).

In 2D Fourier imaging with common Cartesian sampling of k-space, sensitivity encoding enables to reduce the number of Fourier encoding steps by increasing the distance of sampling position in k-space. The factor by which the number of k-space samples is reduced is referred to as the SENSE factor. However, reducing the sampling density results in the reduction of the FOV (aliasing artifacts). In order to unfold this aliasing image, accurate knowledge of the individual coil sensitivities is required. Element-wise division of the array references by the body coil reference yields raw sensitivity maps. Thus, the homogeneity of the body coil is implicitly made the basis of the homogeneity correction carried out by SENSE reconstruction.

Sensitivity encoding is a promising concept in view of physiological and technical speed limits in k-space. SENSE imaging has been successfully performed in combination with FFE, TSE, and half-Fourier EPI.

mGRE

A gradient echo is generated by using a pair of bipolar gradient pulses. In the pulse sequence timing diagram, the basic multiple gradient echo sequence (mGRE) is illustrated in Figure 2.2. There is no refocusing 180° pulse and the data are sampled during different gradient echoes to generate different echo time images. The excitation pulse is termed the alpha pulse α. It tilts the magnetization by a flip angle α, which is typically between 0° and 90°. Gradient echo imaging is typically accomplished by examining the FID, and T_2* is the

characteristic decay time constant associated with the FID. Therefore, mGRE sequence can be used to estimate the T_2* values of tissues.

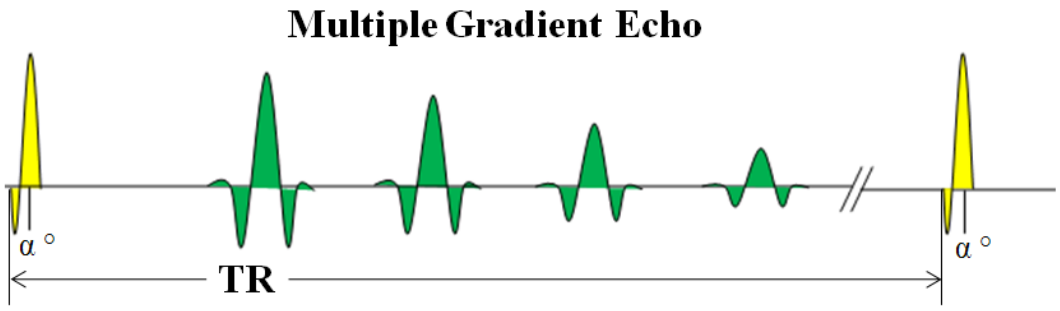

Figure 2.2 Conventional multiple gradient echo acquisition sequence. Multiple gradient echo images are acquired with even spacing echo times during multiple TRs.

IR-HASTE; TURBO; ETL

As shown in Figure 2.3, 90° pulse flips magnetization to horizontal plane and then a number of consecutive 180° pulses are applied per excitation resulting in multiple echoes or profiles. For turbo/fast spin echo scan (TSE), multiple shots are acquired at regular intervals (TR) until completion. The echo train length (ETL) is the number of profiles measured per excitation (shot). Therefore, it is a measure of the scan time acceleration. Half-Fourier acquisition single-shot turbo spin-echo (HASTE) pulse sequence can be used to achieve ultra fast scans. IR-HASTE is a pulse sequence with data acquisition after an initial preparation pulse (inversion recovery) for contrast enhancement with the use of a very long echo train (single shot TSE). This technique is a heavily T_2 weighted, high speed sequence with partial

Fourier technique, a great sensitivity for fluid detection and a fast acquisition time of about 1 sec per slice. This advantage makes it possible for using breath-hold with excellent motionless MRI, e.g. used for abdominal and lung imaging.

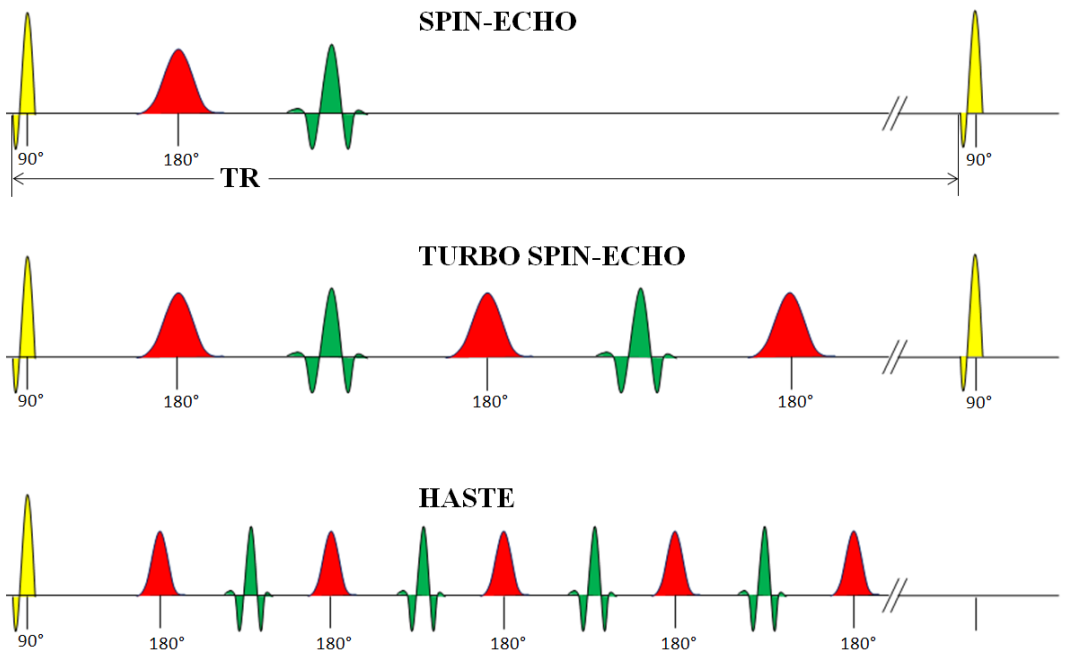

Figure 2.3 Difference between conventional spin-echo, turbo spin-echo, and HASTE imaging shows multiple 180° pulse echoes with a shortened inter-echo spacing to acquire all the imaging data during a TR with HASTE imaging.

Zebra artifact/Moiré fringes

Moiré fringes are an interference pattern most commonly seen when doing gradient echo images (Figure 2.4 indicated by the arrow). This artifact creates a strange and characteristic banding on the image leading to its alternative name of zebra artifact. The appearance of Moiré fringes can be caused by a variety of reasons, e.g., inhomogeneity of the main

magnetic field (B0), interferences of aliased signals at different phases, and interferences of echoes from different excitation modes (stimulated echoes). Improving B0 homogeneity and minimizing wrap of signal, e.g., applying suppression or defining large FOV, may reduce zebra artifact.

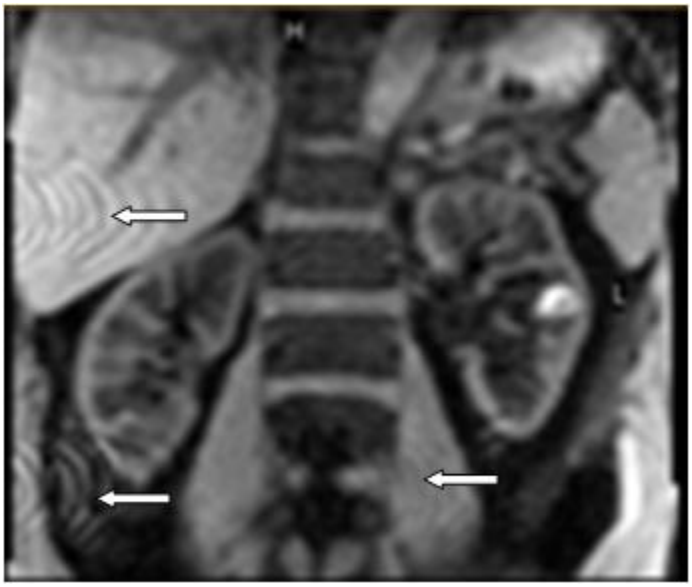

Figure 2.4 Example of moiré interference fringes observed in this coronal abdomen image. Moiré fringe artifacts are indicated by the arrows.

Respiratory compensation techniques

Respiratory Compensation techniques such as respiratory triggering and navigator reduce ghosting artifacts caused by respiratory motion. Typical applications are abdomen, pelvis, thorax and shoulder MR examinations.

Respiratory triggering makes use of the respiratory sensor to detect patient respiration through either abdominal or chest wall motion (Fig. 2.5 a). A trigger signal is generated when

the respiratory signal indicates the beginning of the expiration phase and image data acquisition occurs within the expiration phase by defining an optimal delay time (Fig. 2.5 b). Respiratory triggering technique can be utilized for free breathing dynamic scans.

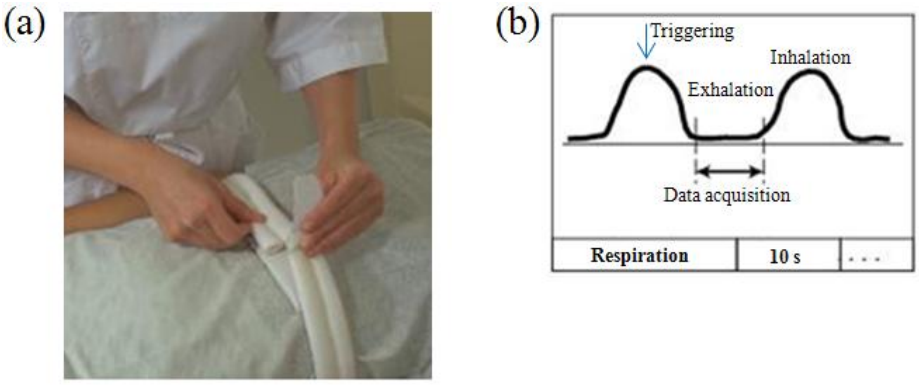

Figure 2.5 Respiratory compensation techniques – respiratory triggering: (a) the respiratory sensor positioning. (b) technical setting aspects of respiratory triggering.

Navigator respiratory compensation uses the so called navigator to sample the respiratory motion. A navigator is a cylindrical MR excitation. It can be used to sample respiratory motion when it is applied along the direction of moving tissue, e.g. the right hemi-diaphragm (Fig. 2.6 a). Therefore, no externally applied respiratory motion sensor is required. During the preparation phase of a navigator compensated scan, the system will automatically perform a free running navigator. These navigator echoes are excited continuously for a short period of time and are used to sample the patients natural respiration cycle (Fig 2.6 b). From this continuous sampling, the most stable and consistent diaphragm position (typically end-expiration) is determined. This stable diaphragm position will be used

to determine the gate window. Navigator echo is interleaved within main scan sequence and is usually used to compensate for respiratory motion during cardiac imaging.

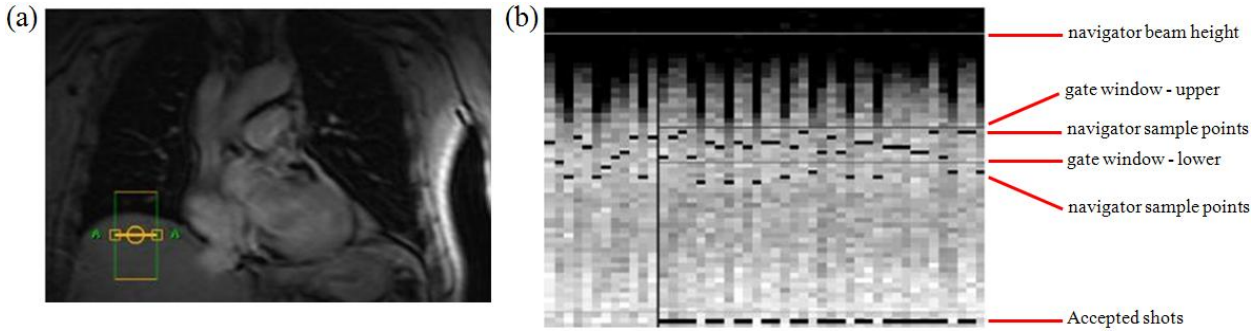

Figure 2.6 Respiratory compensation techniques – navigator: (a) navigator beam positioning. (b) technical setting aspects of navigator compensation.

CHAPTER THREE

CERVICAL CANCER MR STUDIES – tCho AND BOLD/TOLD

3.1 Introduction

Cervical cancer is the second most common type of cancer for women worldwide (Recio, Sahai Srivastava et al. 1998). In the United States, cervical cancer affects approximately 13,000 women each year, and more than 4,000 of women will die (National Cervial Cancer Coalition http://www.nccc-online.org/). ^{1}H MRS has recently been proposed as a means to diagnose cervical cancer and monitor therapy. Several studies have shown that tCho may be detected in malignant cervical tumors using the ^{1}H MRS technique (Allen, Prost et al. 2001; Booth, Pickles et al. 2009). However, some investigators reported that tCho signal was also observed in post-treatment lesion areas and in normal cervix tissues (deSouza, Soutter et al. 2004; Mahon, Cox et al. 2004; Mahon, deSouza et al. 2004). Thus, a quantitative measurement is required to quantify the accurate levels of tCho for differentiating between different pathologies. Additionally, measuring tCho level using ^{1}H MRS may offer the possibility of monitoring the oxygenation status of tumors non-invasively (Star-Lack, Adalsteinsson et al. 2000).

In previous cervical cancer ^{1}H MRS studies, quantitative measurements of tCho level with an internal water reference were performed using endovaginal coils at 1.5 T (deSouza, Soutter et al. 2004; Mahon, Cox et al. 2004; Mahon, deSouza et al. 2004; Booth, Pickles et al. 2009). However, a robust metabolite quantification method has not been implemented at 3T

using a high-quality surface coil, where increased signal compared with lower field strength systems (1.5T) is expected to provide improved spectral resolution and quantification of metabolites. In this study, I evaluate the feasibility of applying internal reference ^{1}H MRS in cervical cancer patients using a surface coil at 3T and assess the relationship between cervical tumor oxygenation (R_1 and R_2*) and tCho concentrations.

3.2 Methods

3.2.1 Overview

Single-voxel (SV) ^{1}H MRS method for the quantification of the absolute tCho concentration, previously described for breast lesions (Bolan, Meisamy et al. 2003; Baik, Su et al. 2006), was implemented in the cervical cancer study at 3T in three phases. First, four phantom solutions with known Cho concentrations were assessed by ^{1}H MRS. Relaxation times (T_1 and T_2) of water and Cho in the solutions were measured and applied for Cho concentration correction. A comparison was made between measured Cho concentration and the true Cho concentration. Second, tCho concentrations in cervix of 4 healthy volunteers were calculated. T_1 and T_2 relaxation times of tCho and water in normal cervix were measured in this experiment. The tCho concentration measurement on one of subjects was repeated to confirm the reproducibility of measurements. Third, a total of 13 patients with biopsy-confirmed cervical tumors were evaluated by ^{1}H MRS. 8 of 13 patients were re-scanned after therapy. T_2 values of water in tumors were measured for the tCho concentration corrections. The tCho concentrations within 15 voxels located in either tumor areas or

residual tumor areas of 9 patients were calculated. Statistical analysis was made to evaluate validation of the quantification method. This study was approved by the Institutional Review Board (IRB) and complies with the Health Insurance Portability and Accountability Act (HIPAA).

3.2.2 Quantification of tCho

The internal reference method for quantification of tCho concentration in *in vivo* studies has been previously used in breast cancer studies (Bolan, Meisamy et al. 2003; Baik, Su et al. 2006; Jansen, Backes et al. 2006). This method was implemented in cervical cancer studies at 3T with appropriate tCho relaxation time approximations. In the present study, all acquisitions were recorded at constant receiver gain. The absolute tCho concentration was calculated by the following equation [3-1]:

$$[\mathrm{tCho}] = \frac{n_{H_2O}}{n_{\mathrm{tCho}}\ MW_{H_2O}} \times \frac{S_{\mathrm{tCho}}}{S_{H_2O}} \times \frac{f_{T_{1H_2O}}}{f_{T_{1\mathrm{tCho}}}} \times \frac{f_{T_{2H_2O}}}{f_{T_{2\mathrm{tCho}}}} \qquad [3\text{-}1]$$

where [tCho] = the concentration of the tCho in units of mmol/kg; S_{tCho} = integral value of tCho peak at 3.2 ppm; S_{H2O} = integral value of the unsuppressed water signal at 4.7 ppm; n_{tCho} and n_{H2O} (the numbers of ^{1}H nuclei for each molecule) = 9 (3 CH_3)and 2, respectively; MW_{H2O} = 18 × 10^{-6} kg/mmol. The f_{T1} and f_{T2} relaxation time correction factors were calculated by using the equations below (Eq. [3-2] and [3-3]):

$$f_{T_1} = 1 - \exp\left(-\frac{TR}{T_1}\right), \quad [3\text{-}2]$$

$$f_{T_2} = \exp\left(-\frac{TE}{T_2}\right). \quad [3\text{-}3]$$

3.2.3 Acquisition

All studies, including phantom, volunteer and patient studies, were undertaken on a clinical 3.0 T MR system (Achieva 3.0 T, Philips Medical Systems, Best, Netherlands) in combination with a 6-element SENSE cardiac surface coil. The spectral signals were acquired from elements 2 and 5 of the coil (center of the coil) to optimize SNR (Philips MR system only exports the sum of spectral signals acquired from selected elements). MR imaging consisted of scout images followed by three orthogonal T_2-weighted images (turbo spin-echo, sagittal, axial and coronal images, TR/TE = 6,700/130 ms, FOV = 180 mm, matrix size = 340×309, slice thickness = 4 mm) for diagnostic and voxel positioning purposes.

^{1}H MRS was then performed using a package of point-resolved spectroscopy sequences (PRESS) (Bottomley 1987) including a tCho scan with water suppression (TR/TE = 2,000/135 ms, 196 averages, bandwidth = 4,000 Hz, and 4,096 data points) and a fully relaxed, unsuppressed water reference scan (TR/TE = 10,000/135 ms, 4 averages, bandwidth = 4,000 Hz, and 4,096 data points). No lipid suppression technique was applied on both sequences. Water suppression in tCho scan was achieved in the PRESS sequence using both three initial chemical shift selective saturation (CHESS) pulses (Haase, Frahm et al. 1985) and band selective inversion with gradient dephasing (BASING) pulses (Star-Lack, Nelson et

al. 1997). To ensure magnetization to reach equilibrium, four dummy scans were performed prior to data acquisition. T_1 and T_2 relaxation times of tCho and water were measured by varying the TR and TE, respectively. The values of T_1 and T_2 were then obtained by fitting the data to a mono-exponential model as a function of TRs and TEs (Eq. [3-2] and [3-3]), respectively. After the T_1 and T_2 corrections were made, the level of tCho metabolite in this work was calculated as a concentration in units of mmol/kg (Eq. [3-1]) and was independent of hardware factors, voxel size, and pulse sequence-related parameters.

3.2.4 Preprocessing and fitting

After acquisition, spectral data were processed by means of the MR spectroscopic analysis package, AdvancedView, provided by the manufacturer (Philips Healthcare Inc.). For the unsuppressed spectra used to measure the water peak, the free induction decays (FID) were truncated to 1024 points and then zero-filled to 2,048 points. After Fourier transformation, zero-order phase correction was applied manually on the water peak. Maximum peak of the water signal was assigned to 4.7 ppm. Frequency range (i.e., water = 4.0–5.4 ppm; 180 Hz) of the spectra was selected for preprocessing and fitting. In order to measure the tCho peak from the suppressed spectrum, a preprocessing stage including truncation of 1,024 points, zero-filling of 4,096 points, Gaussian apodization of 5 Hz, Fourier transformation, and phase correction was performed. The narrow frequency range for fitting tCho peak (i.e., 3.0 –3.4 ppm, 51 Hz) using a Gaussian lineshape model was selected to quantify its amplitude. The measurement error ($\sigma s \bullet$ [tCho]) was estimated using the jMRUI version 3.0 package (Naressi, Couturier et al. 2001).

3.2.5 Statistics

Statistical analysis was performed using online tools (Statistics analysis: T-TEST (http://www.graphpad.com/quickcalcs/ttest1.cfm)). The tCho levels before and after therapy were compared using a paired t-test. A Pearson's correlation coefficient was calculated to relate both oxygen-induced ΔR_2* and ΔR_1 to tCho concentration in tumors.

3.3 Phantom Study: Methods and Results

3.3.1 MRS experiments

Four home-built Cho phantoms with known concentrations of choline hydrochloride (1, 2, 4 and 8 mmol/kg) in aqueous solutions were prepared for metabolite (Cho) quantification (Fig. 3.1e). Each phantom consists of a 1 liter vegetable oil bottle with a 1" diameter choline solution sphere mounted on the bottom. After the localizer scan, coronal images were used for planning a voxel ($2\times2\times2$ cm^3) in the phantoms prior to MRS scans (Fig. 3-1 (e)). The automatic shimming technique was applied for optimization of the homogeneities in each volume of interest (VOI), and typically water peak linewidths of 2 Hz (full width at half-maximum; FWHM) were achieved. After the shimming procedure, a spectrum was acquired with water suppression by using CHESS and BASING techniques. An unsuppressed spectrum was also acquired to measure the amplitude of the water peak in VOI. This MRS package was repeated with different TRs or TEs for estimating water and Cho relaxation times. For example, for the estimation of T_1 values of Cho and water, TR was set at 5

different values (2, 4, 6, 8 and 10 s) with a constant TE at 60 ms; while for Cho and water T_2 measurements, five different TE values (60, 160, 260, 360, and 500 ms) were selected with a fixed TR at 6 s. T_1 and T_2 relaxation times of Cho and water were then determined as described above, and Cho concentrations were estimated and corrected using Eq. [3-1].

3.3.2 Results

The calculated Cho concentrations (mmol/kg) in phantoms were compared with the known concentrations of choline chloride (mmol/kg) in aqueous solutions, as shown in Figure 3.1(f). There was a high correlation between the absolute measurements and the known concentrations ($r^2 > 0.97$). Figure 3.1(a, b, c, d) also illustrates the intensity variation, with respect to TE and TR, of the water peak and Cho peak from the VOI in a phantom. The relaxation times (T_1 and T_2) of Cho and water are shown in Table 3.1. The phantom experiment indicates that it is possible to use an internal reference method to quantify metabolite levels.

Table 3.1
Cho concentration determined by MRS in phantom model

Phantom solution (mmol/kg)	T_1 (ms)		T_2 (ms)		Measured [Cho] + SD (mmol/kg)
	Choline	Water	Choline	Water	
1	1697	2444	597	1425	0.95±0.17
2	1769	2406	586	1487	2.13±0.26
4	1787	2321	581	1533	4.22±0.31
8	1806	2289	574	1569	7.85±0.28
Mean ± SD	1765±48	2365±72	584±10	1503±62	

(a)

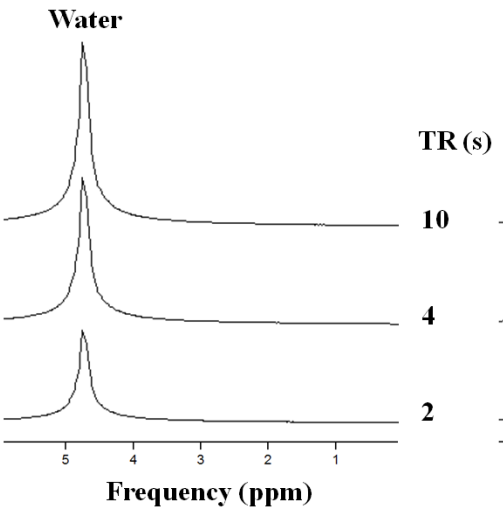
Water
TR (s)
10
4
2
5
4
3
2
1
Frequency (ppm)

(b)

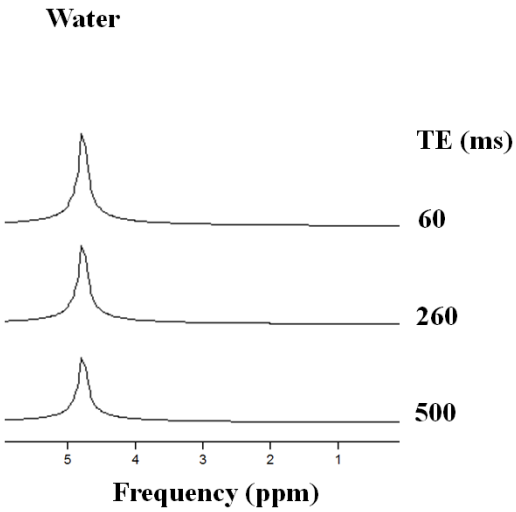
Water
TE (ms)
60
260
500
5
4
3
2
1
Frequency (ppm)

(c)

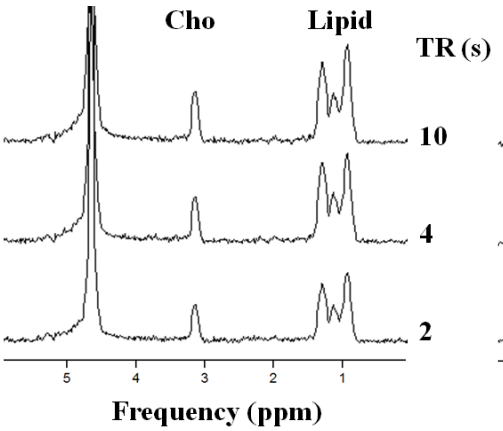
Cho
Lipid
TR (s)
10
4
2
5
4
3
2
1
Frequency (ppm)

(d)

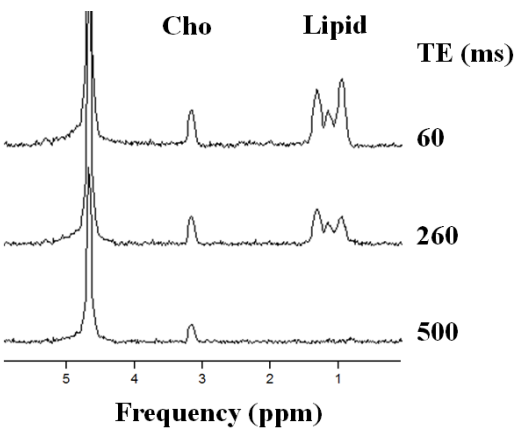
Cho
Lipid
TE (ms)
60
260
500
5
4
3
2
1
Frequency (ppm)

(e) (f)

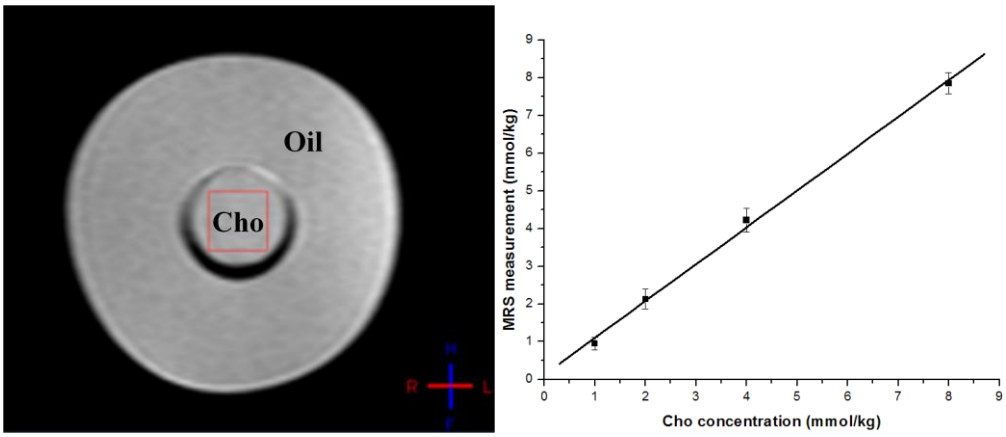

Figure 3.1 Phantom experiments for quantification method validation. T_1 and T_2 values of water and Cho in a known Cho concentration phantom (1 mmol/kg) were measured for correction of absolute Cho level estimation. (a) Water spectra obtained from values of TE of 60, 260, and 500 ms at the same value of TR (2,000 ms). (b) Water spectra obtained from values of TR of 2,000, 4,000, and 10,000 ms at the same value of TE (60 ms). (c) Cho spectra with suppressed water obtained from values of TE of 60, 260, and 500 ms at the same value of TR (2,000 ms). (d) Cho spectra obtained from values of TR of 2,000, 4,000, and 10,000 ms at the same value of TE (60 ms). (e) voxel placement in the center of the phantom (Cho: Choline solution; Oil: vegitable oil). (f) The linearity between the absolute tCho concentrations measured and the known tCho concentrations in phantoms (r^2 >0.97).

3.4 Volunteer Study: Methods and Results

3.4. 1 MRS experiments

The internal referencing strategy requires T_1 and T_2 corrections of tCho and water. In this study, T_1 and T_2 relaxation times of tCho and water were measured in the cervixes of four healthy subjects (age = 32 ± 4 years; range 28-35 years) (Table 3.2). To confirm the reproducibility of the measurements, relaxation times were re-measured in one subject three weeks later. The average relaxation times (T_1 and T_2) of tCho were calculated and would later be used for correction of tCho level in cervical tumors because measurements of the tCho relaxation times in patient studies are impractical (time-consuming) in routine clinical exams.

All subjects were scanned using the same protocol which consisted of a scout scan, a reference scan, three high-resolution T_2-weighted scans for localization and a series of ^{1}H MRS scans with variable TR or TE for relaxation time estimation. After the localizer, a voxel was placed in the cervix region by an experienced radiologist. For the estimation of T_1 values of tCho and water, TR was set at 3 different values (2, 4, and 6 s) with a constant TE at 85 ms; while for tCho and water T_2 measurements, three different TE values (85, 135, and 185 ms) were selected with a fixed TR at 2 s. T_1 and T_2 relaxation times of tCho and water were then determined by fitting Eq. [3-2] and Eq. [3-3], and tCho concentrations were estimated and corrected using Eq. [3-1].

3.4. 2 Results

In 4 subjects, the voxel sizes were between 4.2 and 8.0 ml depending on the size of the cervix and the tCho resonance peaks were detected at 3.2 ppm. The calculated relaxation times of tCho and water for each of the subjects are shown in Table 3.2. Figure 3-2 (a, b, c, d) illustrate the intensity variation with respect to TE and TR, of the water and tCho peaks from a normal cervix in subject #3. Figure 3-2 (a) and (c) present water and tCho spectra obtained at TRs of 2, 4, and 6 ms using a fixed TR of 2s. The average values of T_1s (mean ± SD) were water = 1,490 ± 45 ms and tCho = 1,369 ± 36 ms from the four subjects, respectively. Figure 3-2 (b) and (d) display water and tCho spectra obtained using values of TE of 85, 135, and 185 ms, respectively, at the fixed values of TR (2s). The averaged T_2 relaxation times for water and tCho were 53 ± 5 ms and 131 ± 12 ms, respectively. The measurements of relaxation times were reproducible in Subject 4 with acceptable intra-individual measurement variations, (T_1: variation of less than 4.5% for tCho and 7.5% for water; T_2: variation of less than 5.7% for tCho and 7.3% for water). After the T_1 and T_2 corrections were made, the absolute tCho levels were generated with a mean value of 0.92 ± 0.17 mmol/kg. These averaged T_1 and T_2 relaxation times for tCho were then applied for the estimation of tCho concentration in cervical cancer patient studies.

Table 3.2

Metabolite biologic parameters determined by MRS in healthy volunteers

Subject	T_1 (ms)		T_2 (ms)		[tCho] ± SD (mmol/kg)
	tCho	Water	tCho	Water	
1	1403	1458	131	58	0.73±0.56
2	1394	1466	137	53	1.15±0.72
3	1339	1510	147	46	0.92±0.64
4	1324	1554	123	55	0.87±0.69
Mean±SD	1369±36	1490±45	131±12	53±5	0.92±0.17
4(2)	1387	1437	116	51	0.96±0.71

4(2): The repeated scan was performed to confirm the reproducibility of measurements.

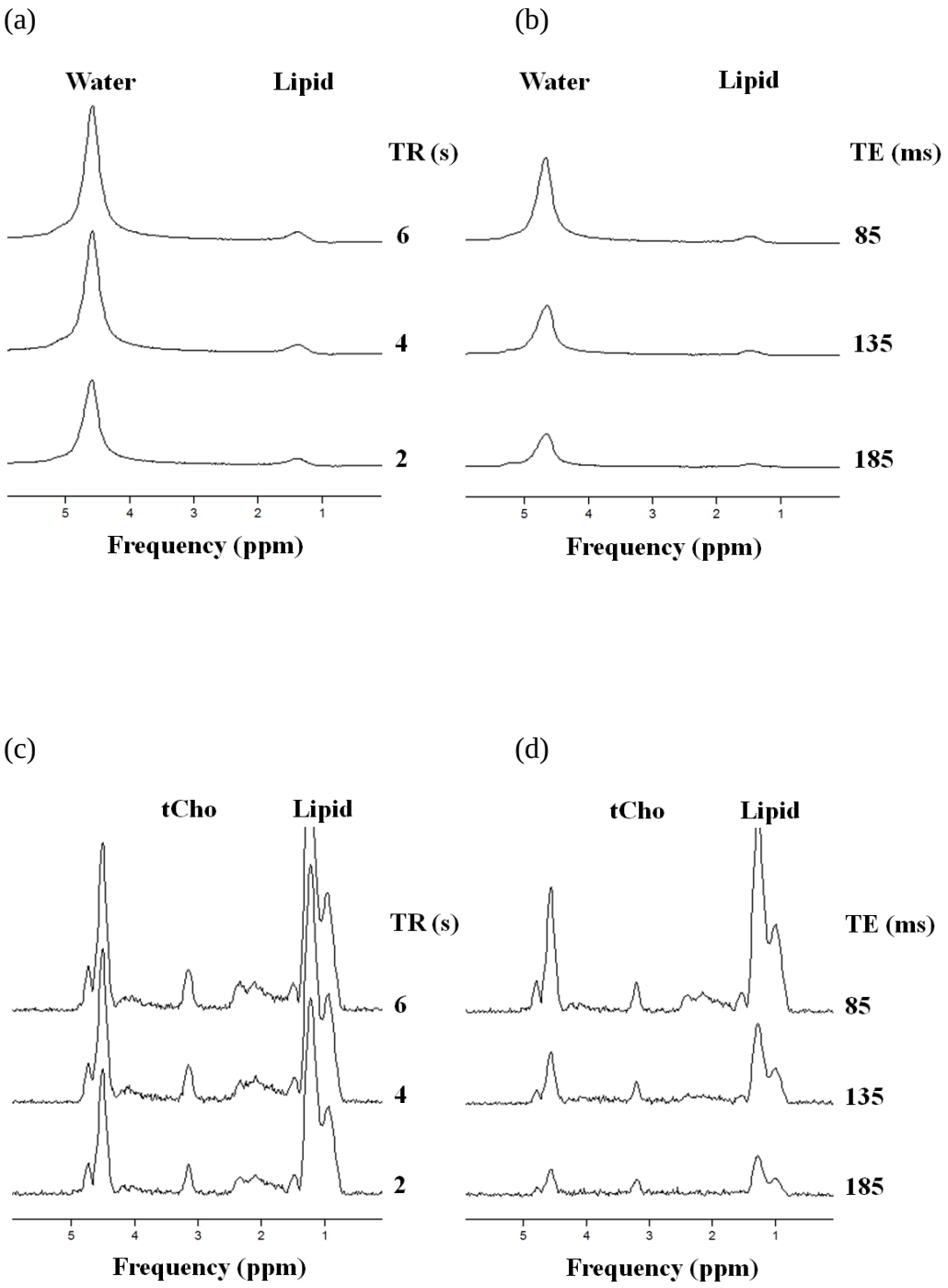
(a)
Water
Lipid
TR (s)
6
4
2
5
4
3
2
1
Frequency (ppm)
(b)
Water
Lipid
TE (ms)
85
135
185
5
4
3
2
1
Frequency (ppm)
(c)
tCho
Lipid
TR (s)
6
4
2
5
4
3
2
1
Frequency (ppm)
(d)
tCho
Lipid
TE (ms)
85
135
185
5
4
3
2
1
Frequency (ppm)

(e)

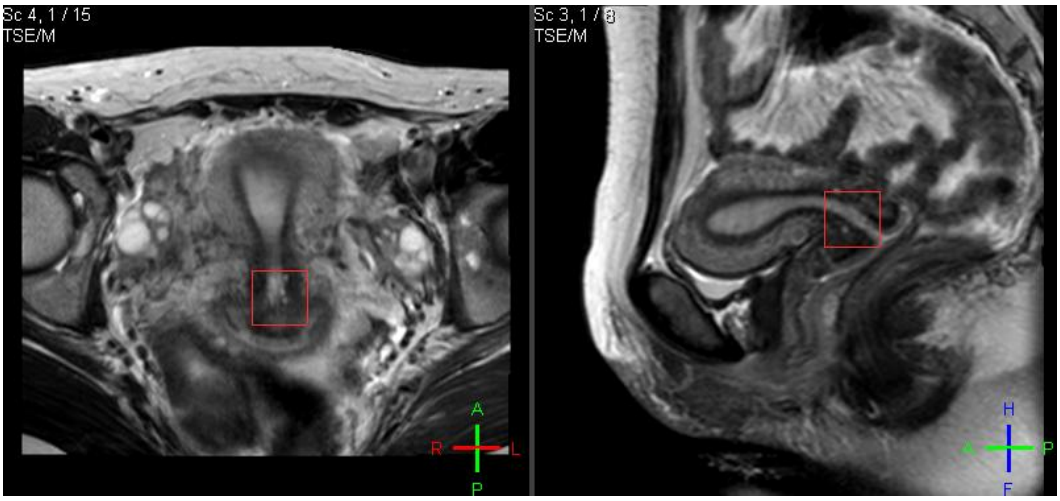

Figure 3.2 Volunteer experiments for estimation of correction factors. T_1 and T_2 values of water and Cho in normal cervix were measured for correction of absolute Cho level estimation. (a) Water spectra obtained from values of TE of 60, 260, and 500 ms at the same value of TR (2 s). (b) Water spectra obtained from values of TR of 2, 4, and 10 s at the same value of TE (60 ms). (c) Cho spectra obtained from values of TE of 85, 135, and 185 ms at the same value of TR (2,000 ms). (d) Cho spectra obtained from values of TR of 2, 4, and 6 s at the same value of TE (85 ms). (e) Example placement of the normal cervix voxel ($20\times20\times20$ mm^3, red box) in T_2-weighted images of the axial plane (left) and the sagittal plane (right).

3.5 Cervical Cancer Patient Study: Methods and Results

3.5.1 MRS experiments

Thirteen patients (range 30–56 years old, mean 43.69 ± 7.48 years) with biopsy-confirmed cervical cancer (FIGO stage IIA to IVA; 11 with invasive cervical squamous cell carcinoma (SCC) and 2 with invasive adenocarcinoma (patient 8 and 9)) were recruited to participate in this study between June 2008 and May 2011. Two of the thirteen patients were found to have metal clips. All patients were examined with the same MRI/MRS protocol after biopsy, which consisted of a scout scan, a reference scan, three high-resolution T_2-weighted scans for tumor localization and diagnoses, a BOLD/TOLD dynamic scan with 100% oxygen challenges for tumor oxygenation studies, a SV ^{1}H MRS package including an unsuppressed water reference scan and a suppressed tCho scan for tumor metabolism quantification and a dynamic contrast-enhanced magnetic resonance imaging (DCE-MRI) scan for tumor vascularity studies. The typical scan time for this study was approximately 1.5 hours. A baseline scan was done on 13 patients prior to the start of radiotherapy. A post-treatment scan was performed for 8 of 13 patients within 2 to 4 months later.

T_2-weighted images (sagittal, transverse and coronal images) were used for voxel placements. The spectroscopic voxel was carefully positioned centrally within the cervical mass or in the center of the cervix if no mass was visible by experienced radiologists to maximize the coverage of the lesions and minimize the inclusion of pericervical fat and necrosis fluid. In the longitudinal exam, the voxel was placed on the same region of the tumor/cervix in pre- and post-radiotherapy measurements on the same patient, but the voxel

size (3-15 ml, mean = 7.8 ml) was variable depending on the dimension of the tumor/cervix under examinations. Voxel shimming (iterative shimming) was performed automatically on the water resonance for optimizing the magnetic field homogeneities in the localized volumes, and FWHM of water peak was usually 11–17 Hz. The voxel was repositioned or spectroscopy was abandoned if the FWHM of water was greater than 20 Hz or a huge lipid peak (> water peak) appeared. Resonance peaks were all phased to tCho peak. To remove a potential source of physiological variation, measurements of water T_2 (TR = 6,000 ms; TE = 85, 110, 135, 160 and 185 ms; 4 averages) for each voxel was performed in the unsuppressed water reference scan to minimize water T_1 and T_2 effects in tCho quantification. The total time of tCho scan and water reference scan was approximately 10 minutes. This MRS package was performed before (on first 4 patients) or after (on rest 9 patients) tumor oxygenation scans (BOLD/TOLD).

3.5.2 Results

In 13 patients, tumors were identified on the conventional high resolution T_2-weighted images (Fig 3.4 a, c) and tumor volumes were estimated by summing up tumor ROIs in all slices with help of radiologists. The mean volume of 13 cervical tumors prior to therapy was 187±195 ml and post-treatment residual tumor size (6 patients) was 31±38 ml (Table 3.3). The spectroscopic voxel size ranged from 3 to 15 ml depending on the size of the tumor or post-treatment residual area. The tCho resonance was detected at 3.2 ppm in 15 (71%) of the 21 spectra. The tCho peak was fitted with a Gaussian with a linewidth of 5–9 Hz, and

unsuppressed water peak was fiof 5 with a Lorentzian with the line width of 13–24 Hz, respectively.

(a)

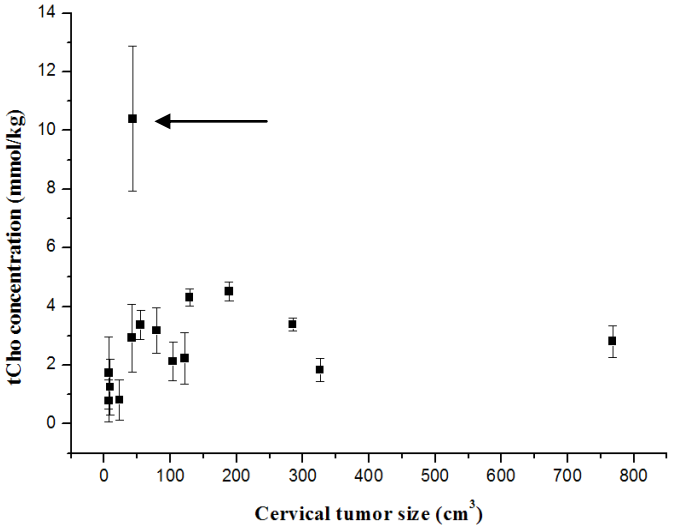

(b)

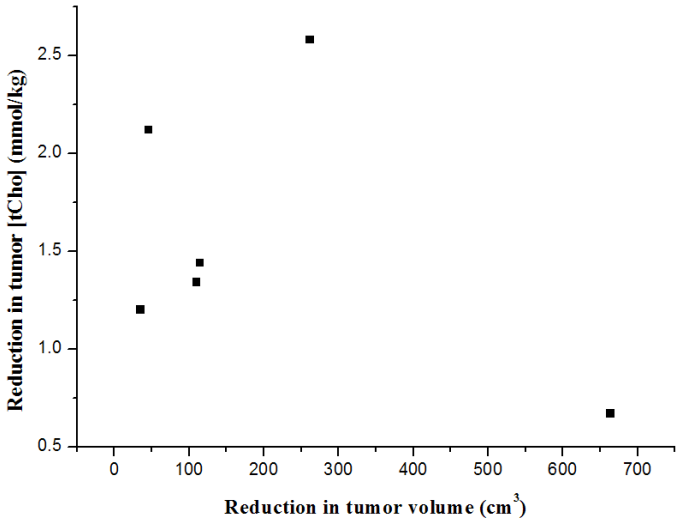

Figure 3.3 The relationship between absolute tCho concentrations and lesion volume. (a) The absolute tCho levels obtained from a total of 9 in vivo cervical spectra is independent of lesion volume of cervical cancer. (b) Of the 6 patients who completed the pre- and post-treament MR exams, the reduction in tCho concentration did not appear to be related to reduction in tumor sizes. An outlier is indicated by the arrow.

TABLE 3.3

Quantification of tCho by proton MRS at 3T in 13 cervical cancer patients

Patient	Age (year)	Tumor Size (ml)		[tCho] ± SD (mmol/kg)		Comments
		Pre-treatment	Post-treatment	Pre-treatment	Post-treatment	
1	47	141	9	NA	NA	Bladder filling
2*	53	285	23	3.39±0.23	0.81±0.69	
3*	41	122	7	2.23±0.88	0.79±0.71	
4†	38	768	104	2.81±0.54	2.14±0.66	PT was dead
5†	56	189	79	4.52±0.32	3.18±0.78	
6	56	163	8	NA	NA	Clip
7*	48	55	9	3.37±0.49	1.25±0.94	
8*	50	42	7	2.93±1.15	1.73±1.23	
9	43	56		NA		Clip
10	39	326		1.84±0.39		
11	42	43		10.40±2.47‡		
12	36	129		4.31±0.29		
13	31	110		NA		Motion
Means	44±8	187±195	31±38	3.18±0.93	1.65±0.92	

*: a responder cases – a successful treatment with a significantly anatomic reduction.

†: a non-responder case – an unsuccessful treatment with a large residual remaining.

‡: an outlier which was discarded.

The calculated average T_1 and T_2 relaxation times for tCho in normal cervixes were utilized to correct tCho concentrations within cervical tumors of 13 patients. Additional T_2 measurement for water was performed at each visit. The effects of water T_1 were negligible due to the use of a long TR setting. The corrected absolute tCho levels are shown in Table 3.3. Figure 3.3 (a) shows a plot of tCho concentration versus cervical lesion volume. The tCho levels were not correlated to lesion volumes of cervical cancer. An outlier appeared to deviate markedly from other values in Fig. 3.3 (indicated by an arrow). However, the causes

were unknown, because many reasons such as system behavior, human error, instrument error or simply through natural deviations in populations may be involved in, thus this outlier was discarded for statistical analysis. Of the 6 patients who completed the protocol, the reduction in tCho concentration between pre-therapy and post-therapy did not appear to be related to the reduction in tumor volumes (Figure 3.3 (b)). Figure 3.4 shows a 45-year-old patient (#2) with an invasive cervical squamous cell carcinoma. Figure 3.4A and 3.4C demonstrate cervical tumor location and voxel placement before and after therapy, respectively. Figure 3.4B and 3.4D are spectra obtained from lesion or residual area before and after therapy, respectively. The corresponding tCho concentrations are 3.39±0.23 mmol/kg before therapy and 0.81±0.69 mmol/kg after therapy. Significant reductions in both tumor sizes and tCho levels can be observed. Although the changes in tCho concentration after the complete course of therapy were not significantly different between responders and non-responders ($p = 0.18$) (Fig. 3.5), the relative reduction ($([tCho]_{pre}-[tCho]_{post})/[tCho]_{pre}*100\%$) in tCho concentration between baseline and post-therapy showed significant difference ($P = 0.04$) between responders (4 of 6) and non-responders (2 of 6). No error bar was added on each data point because error bars were not informative due to the large standard deviations (Haddadin, McIntosh et al. 2009).

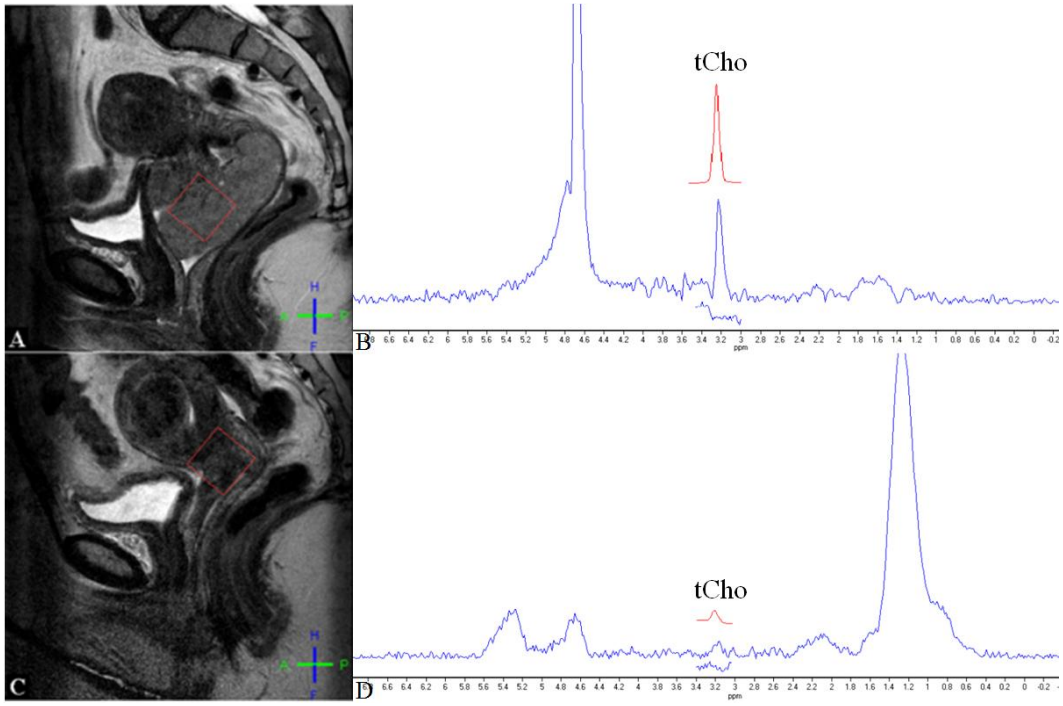

Figure 3.4 An example of a responder, showing decreased tCho concentration after therapy, and a clear anatomical response by the end of treatment. MRI and MRS measurement of a 54-year-old patient with biopsy-proven invasive squamous cell carcinoma of uterine cervix. (A), Sagittal non-fat-suppressed T2-weighted image shows an invasive squamous cell carcinoma located at uterine cervix. This image also demonstrates the voxel placement. (B), Magnified spectrum illustrates a low lipid (Lip) peak, but a high tCho resonance peak is visible at 3.2 ppm, and the fitting produces a measurement of [tCho] = 3.39 ± 0.23 mmol/kg. (C), Sagittal non-fat-suppressed T_2-weighted image obtained 3 months later, after completion of treatment with therapy. (D), There is resolution of the peak centered around choline ([tCho] = 0.81± 0.69 mmol/kg), which is indicative of local control. The large lipid peak is due to partial volume of the pericervical fat in this region. The estimated model fit was shown above the full spectrum and the residue was shown underneath (B and D).

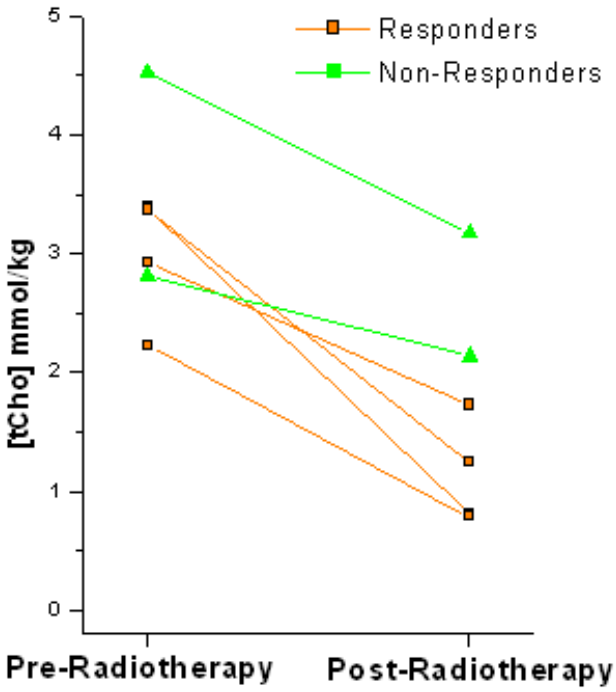

Figure 3.5 Cervix ^{1}H MRS can be used to evaluate response to therapy. These data include 6 patients measured with 3 T cervix MRI/MRS before the start of therapy and after the complete course of treatment (2-3 months later). The tCho concentration measurements are shown for the pre- and post-therapy measurements in both responders and non-responders showed a decrease in tCho concentration after treatments, but non-responders exhibited a higher post-treatment [tCho]. The reductions of tCho concentration after the complete course of therapy were not significantly different between respondors and non-responders ($p = 0.18$).

3.6 Cervical Cancer Patient Study: BOLD and TOLD

3.6.1 BOLD and TOLD experiments

As described in Chapter Two, tumor oxygenation can be assessed by the use of BOLD/TOLD contrast MRI. In the cervical tumor oxygenation experiments, all patients were examined during room air breathing followed by 100% oxygen (15 L/min.), which was administered via a face mask (adult oxygen mask, CareFusion, France) that was worn throughout the experiment. SaO_2 and heart rate were monitored throughout the experiment using a pulse oximeter (In vivo 4500 MRI, In vivo Research Inc., Orlando, FL).

For the first four patients, BOLD and TOLD contrast data were acquired during air and oxygen inhalation. For the later 9 patients, quantitative R_2* and R_1 measurements were performed in the sagittal plane using a mGRE sequence (TR = 65 ms, min TE = 2 ms; ΔTE = 2.5 ms, 16 echoes, FA = 30°, FOV = 300 mm, matrix size = 240x240, thickness = 5 mm, 1 slice) and a series of IR-HASTE sequences (TI = 0.3s, 0.4s, 0.6s, 1.2s, 1.4s, and 1.6s, TR = 10s, TE = 5.4s, FA = 90°, FOV = 300 mm, matrix size = 240x240, TSE factor = 47, SENSE factor = 2, , thickness = 5 mm, 1 slice), respectively.

Of the 9 patients with complete quantitative relaxation time scans, three (#6, #9, and #13) showed poor image quality and severe image distortion due to existing metal clips or bulk motion (Table 3.3). Additionally, incorrect control parameter settings for R_1 measurements (patient #10 – #12) occurred during data acquisition (Table 3.4). Therefore, all those data were discarded in tumor oxygenation studies.

BOLD MRI data analysis was performed using the AdvancedView software (Philips Healthcare Inc., Holland). ROIs overlapped the MRS voxels which were drawn by experienced radiologists. Data acquired using a MGRE sequence allowed R_2* maps to be generated by fitting the multi-echo T_2*-weighted image signal intensities to TEs using Eq. [2-6]. The relative change of R_2* due to oxygen challenge was then calculated as:

$$\%\Delta R_2^* = \frac{R_{2t}^* - R_{2b}^*}{R_{2b}^*} \cdot 100\% \qquad [3\text{-}4]$$

where R_{2b}* represents mean baseline rate during air breathing, and R_{2t}* is the mean rate with oxygen inhalation. The values of ΔR_2* were compared with tCho concentration in the corresponding voxel.

Similarly, accurate T_1 maps can be generated by fitting IR HASTE image data to 6 different TIs with Eq. 2-2. The relative change of R_1 under an oxygen challenge was defined as:

$$\%\Delta R_1 = \frac{R_{1t} - R_{1b}}{R_{1b}} \cdot 100\% \qquad [3\text{-}5]$$

where R_{1b} represents baseline rate during air breathing, and R_{1t} is the rate with oxygen breathing. The values of ΔR_1 were compared with tCho concentration in the corresponding voxel.

3.6.2 Results

In 6 cervical cancer patients (Table 3.4), R_2* values were estimated in the tumor areas overlapping the selected VOIs for MRS measurements (Fig. 3.6). The mean R_2* of cervical tumors prior to therapy was 19.2±2.6 s^{-1} in air breathing and 19.1±2.2 s^{-1} in oxygen

breathing, respectively. After therapy, the mean R_2* of residual tumor areas was significant increased to 34.8±6.4 s^{-1} in air breathing and 35.4±7.4 s^{-1} in oxygen breathing, respectively (Table 3.6).

Meanwhile, R_1 values were calculated in the same areas in 3 patients (Table 3.5). The mean baseline (prior to therapy) R_1 values were 0.66±0.03 s^{-1} in air inhalation and 0.67±0.03 s^{-1} in 100% oxygen inhalation. After therapy, the mean R_1 values in residual tumor areas were increased to 0.77±0.10 s^{-1} during air breathing and 0.80±0.10 s^{-1} during 100% oxygen breathing (Table 3.6).

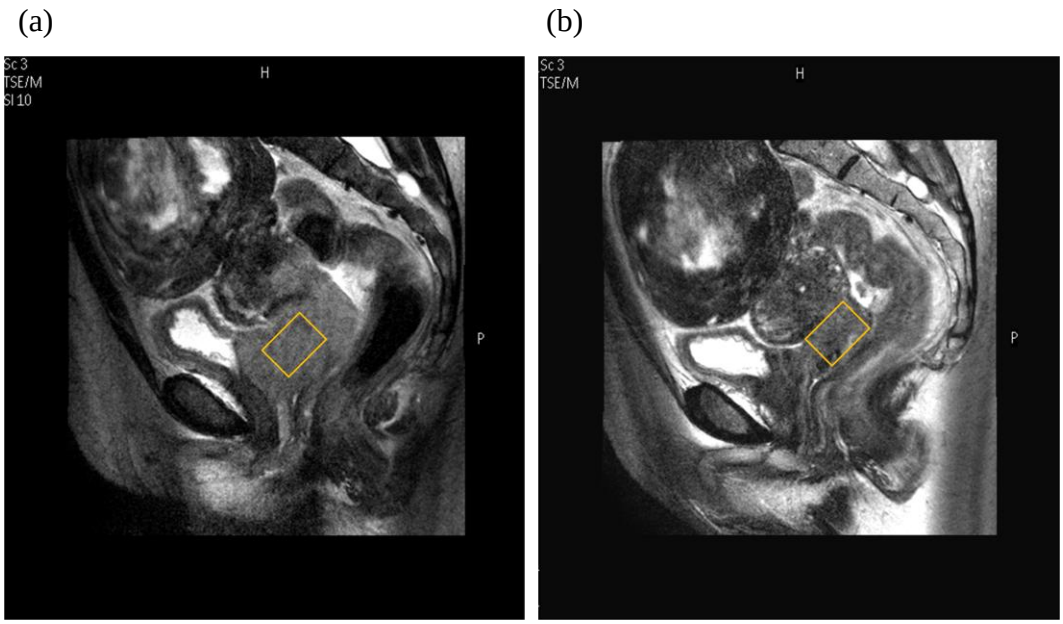

Figure 3.6 Example volume of interest placement in a cervical tumor for estimation of tumor R_1, R_2* and [tCho]. (a) a pre-treatment cervical tumor in T_2-weighted image of the sagittal plane. (b) the corresponding post-treatment cervical tumor (residual) in T_2-weighted image of the sagittal plane.

TABLE 3.4

Tumor oxygenation measurements by BOLD at 3T in 13 cervical cancer patients

Patient	Age (year)	R_2* ± SD (s^{-1}) (air/oxygen)		%ΔR_2* ± SD		Comments
		Pre-treatment	Post-treatment	Pre-treatment	Post-treatment	
1	47	N/A	N/A	N/A	N/A	No R_2* scan
2	53	N/A	N/A	N/A	N/A	No R_2* scan
3	41	N/A	N/A	N/A	N/A	No R_2* scan
4	38	N/A	N/A	N/A	N/A	No R_2* scan
5	56	22.1±0.7/ 21.6±0.8	29.0±1.0/ 28.8±1.1	-2.3±6.9	-0.7±7.3	
6	56	N/A	N/A	N/A	N/A	Clip
7	48	17.7±0.6/ 16.6±0.6	33.8±0.9/ 33.9±0.8	-6.5±7.0	0.3±5.0	
8	50	17.4±0.5/ 18.9±0.7	41.6±1.2/ 43.4±1.1	8.4±7.1	4.4±5.7	
9	43	N/A	N/A	N/A	N/A	Clip
10	39	15.7±0.5/ 16.5±0.7	N/A	5.2±7.8	N/A	
11	42	21.1±0.8/ 20.3±0.8	N/A	-3.8±7.7	N/A	
12	36	21.1±0.7/ 20.8±0.6	N/A	-1.4±6.2	N/A	
13	31	N/A	N/A	N/A	N/A	Motion
Means		19.2±2.6/ 19.1±2.2	34.8±6.4/ 35.4±7.4	-0.1±5.7	1.3±2.7	

Patient #1- #4 were not offered R_2* quantification scans.

Patient #6 and #9 had a metal clip preventing R_2* measurements.

Patient #13 experienced severe body motion preventing R_2* measurements.

TABLE 3.5

Comparisons of untreated and treated cervical tumor characteristics (tumor size, tCho concentration, and oxygenation parameters (R_1 and R_2*))

	Num	Pre-treatment	Post-treatment	P-value	Comments
Ave Tumor Size (ml)	8	221±234	31±38	~0.04	Significant
[tCho] (mmol/kg)	6	3.2±0.8	1.7±0.9	~0.01	Significant
Ave. R_2* (s^{-1})	3	19.1±2.6	34.8±6.4	~0.02	Significant
$\%\Delta R_2$*(O_2 breathing)	3	-0.1±5.7	1.3±2.7	~0.77	Not significant
Ave. R_1 (s^{-1})	3	0.7±0.1	0.8±0.1	~0.14	Not significant
$\%\Delta R_1$ (O_2 breathing)	3	1.2±1.0	4.0±2.7	~0.17	Not significant

TABLE 3.6

Tumor oxygenation measurements by TOLD at 3T in 13 cervical cancer patients

Patient	Age (year)	R_1 ± SD (s^{-1}) (air/oxygen)		$\%\Delta R_1$ ± SD		Comments
		Pre-treatment	Post-treatment	Pre-treatment	Post-treatment	
1	47	N/A	N/A	N/A	N/A	No R_1 scan
2	53	N/A	N/A	N/A	N/A	No R_1 scan
3	41	N/A	N/A	N/A	N/A	No R_1 scan
4	38	N/A	N/A	N/A	N/A	No R_1 scan
5	56	0.675±0.033/ 0.684±0.029	0.807±0.041/ 0.854±0.037	1.3±9.3	5.8±10.0	
6	56	N/A	N/A	N/A	N/A	Clip
7	48	0.674±0.028/ 0.689±0.031	0.656±0.027/ 0.691±0.029	2.2±8.8	5.3±8.7	
8	50	0.628±0.028/ 0.629±0.027	0.856±0.036/ 0.864±0.039	0.2±8.6	0.9±8.9	
9	43	N/A	N/A	N/A	N/A	Clip
10	39	N/A	N/A	N/A	N/A	Incorrect setting
11	42	N/A	N/A	N/A	N/A	Incorrect setting
12	36	N/A	N/A	N/A	N/A	Incorrect setting
13	31	N/A	N/A	N/A	N/A	Motion
Means		0.66±0.03/ 0.67±0.03	0.77±0.10/ 0.80±0.10	1.2±1.0	4.0±2.7	

Patient #1 – #4 were not offered R_1 quantification scans.

Patient #6 and #9 had a metal clip preventing R_1 measurements.

Patient #10 – #12 had incorrect settings (receiver gains or scales) during data acquisition.

Patient #13 experienced severe body motion.

3.7 Discussion

In vivo ^{1}H MRS is a non-invasive technique that provides information on tumor metabolism, showing a substantial elevation of choline-containing compounds (Bolan, Meisamy et al. 2003; Baik, Su et al. 2006). Several studies have demonstrated that tCho can be detected in human cervical tumors using ^{1}H MRS with an endovaginal coil at 1.5 T (Allen, Prost et al. 2001; deSouza, Soutter et al. 2004; Mahon, Cox et al. 2004; Booth, Pickles et al. 2009). However, all of those studies have measured tCho content qualitatively or used a semi-quantitative method for differentiating malignant and normal tissues. It is obvious that a quantitative method is necessary for improving the accuracy of lesion diagnosis because the sensitivity of the MRS measurement is variable due to variations in voxel size, tissue heterogeneity, and receiver coil efficiency. My preliminary study has shown the feasibility of using an internal water reference ^{1}H MRS for quantifying absolute tCho levels with a surface coil at 3 T in the cervical tumor system. Furthermore, these calculated quantitative relaxation rates and tCho concentrations in cervical tumors provide a quantitative basis for future investigations of relationships between metabolite concentration and tumor oxygenation in normal and cancerous cervical tissues.

The internal referencing strategy requires corrections using relaxation times of the tCho and water. Water relaxation time correction factors can be estimated in a short reference scan. In this work, water T_2 estimation was achieved by acquiring multiple echoes in a water reference scan, meanwhile, water T_1 effect was negligible by choosing a long TR ($TR > 5 \cdot T_1$) setting. However, accurate determination of T_1 and T_2 values of tCho in tumors is usually

time-consuming to be performed for every patient. Some investigators calculated average values of relaxation times from a small patient group, and then applied mean relaxation time values on large group estimation (Bolan, Meisamy et al. 2003; Baik, Su et al. 2006). This method offered a good compromise for quantification of metabolites in tumor studies. In this work, measuring the average relaxation times on cervical patients was impractical. Here, I utilized average T_1 and T_2 of tCho from healthy volunteers to correct tCho concentration estimation. Compared to corrections based on mean values in patient groups, corrections from a healthy volunteer group only produce a fixed deviation in the quantitative measurements of tCho concentrations. This is considered acceptable in cervical cancer studies. Moreover, measurements of water T_2 values for each patient may minimize influence of water T_2 variation in different pathologic conditions. For example, after therapy, the T_2 values of the cervical tumors were reduced moderately (Fig. 3.4 A and C).

The present study used the AdvancedView and jMRUI software packages for analysis of cervical tumor tCho levels before and after of therapy. Accurate fitting of MR cervical tumor spectra can be achieved by optimizing parameter settings. Here, a narrow frequency range was defined around the tCho peaks (i.e., 3.02-3.42 ppm) avoiding bias from neighboring water or lipid contamination. Linewidths for tCho peaks were allowed if less than 10 Hz. Moreover, patient's motion and respiration may cause tCho peak broadening with Gaussian lineshapes in the average spectra, so a Gaussian lineshape model was applied to fit the tCho peaks (Fig. 3.4 B and D). This model performed reasonably well with small standard deviations in fitting errors. The measured tCho levels were within a range of 0.79-10.4 mmol/kg which was comparable to the findings of previous studies in breast tumors

(Bolan, Meisamy et al. 2003; Baik, Su et al. 2006). More patient MRS exams may help to confirm whether the absolute tCho values reported here are reasonable and reproducible in repeated MRS measurements.

Some investigators reported cervical cancer biomarker drawbacks of ^{1}H MRS. Mahon et al. group quantified spectra by the ratio of tCho to unsuppressed water. *In vivo* results showed no significant differences between the levels of tCho detected in cancerous and normal tissues. This finding was inconsistent with their ex-vivo MRS studies. Partial volume effects within the VOI may be responsible, for example, the inclusion of necrosis fluid or normal tissues in tumor voxels would underestimate tCho levels in tumors. In my work, patients with large cervical tumors ranging from 42 ml to 768 ml were selected. Small voxels (< 30ml) were placed in the center of tumors carefully, but away from tumor necrosis areas and pericervical fat tissues by experienced radiologists. This VOI selection strategy would also be helpful to reduce spectral distortions/artifacts caused by water and fat contaminations. Evident differences in tCho levels between cervical tumors and residual areas or normal cervixes were observed in this study. Increased patient numbers are needed to estimate the threshold for malignant diagnosis and statistical significance.

Several groups also described in-phase -CH_2 lipid peaks at 1.3 ppm as a biomarker of cervical cancer (de Bazelaire, Duhamel et al. 2004; Mahon, Cox et al. 2004). However, estimation of -CH_2 lipid levels in cervical tumors was unreliable in this study. The resonances of lipid at 1.3 ppm were seen in all 15 spectra. But the majority of spectra (12 of 15) showed broadened and distorted -CH_2 lipid peaks due to pericervical fat contamination. Imperfect slice selection profiles and unexpected patient motion may be responsible for these

lipid resonance distortions. Our previous studies showed that contamination levels of the PRESS localization technique might reach 7% to 12%. The use of a better slice selective RF pulse or improved spoiling and presaturation band techniques might minimize these contaminations. Furthermore, ^{1}H MRS was performed at the end of the long exam (1.5 hours) which induced more patient motion issues. Further studies with better patient compliance (less movement) would improve experiments.

The majority of previous cervical cancer ^{1}H MRS scans were performed using endovaginal coils at 1.5T scanner. Although the endovaginal coil provided a higher signal-to-noise ratio, it is invasive and difficult to position, especially in large tumor cases where it is often displaced from the cervix. In this work, high-quality spectra were achieved using a SENSE cardiac surface coil at 3T. This MRS protocol can be directly added in the routine clinical cervical cancer exam.

Care was needed when performing the ^{1}H MRS scan with long intervals between the scout scan and the ^{1}H MRS scan. Unexpected movements may occur during the gap. In this work, the 1st patient who was given IV fluid during the MRI exam experienced quick bladder filling which caused imperfect voxel placements. This influence was overcome in later experiments by adding a short scout scan prior to the MRS scan to verify and correct the VOI placement. The overall failure rate of cervical tumor ^{1}H MRS was approximately 1/3.

A limitation to cervical cancer single voxel (SV) MRS is the lack of the spatial distribution information of metabolites. Although SV MRS can be used to measure absolute metabolite concentrations in a specific VOI, it does not allow the study of heterogeneity within the lesion of interest. A 3D chemical shift imaging technique (3D CSI) has been tested

and applied in our recent prostate tumor exams obtaining high quality localized spectra from array of continuous voxels throughout the lesion (Geethanath, Baek et al. 2012). Future use of this 3D technique on cervical cancer studies may provide spatial heterogeneity of lesions and allow better definition of proliferating areas of tumor for radiotherapy.

Another issue that may need to be addressed is the threshold of tCho concentrations for separating the residual/normal tissues or malignant lesions. The optimal cutoff value cannot be determined from this study due to the small sample size. However, the purpose for this pilot study was primarily to evaluate the feasibility of a quantitative ^{1}H MRS method in cervical cancer studies using the SENSE cardiac surface coil at 3T, and not to explore tCho concentration variability.

3.8 Summary

This work lays a foundation for future investigations of relationships between metabolite concentration and tumor oxygenation in normal and cancerous cervical tissues. The present study has shown the feasibility of using an internal water reference in ^{1}H MRS for quantifying absolute tCho levels with a surface coil at 3 T in the cervical tumor system. However, more patient studies are needed to determine if ^{1}H MRS is an effective and robust method to investigate tumor metabolisms.

CHAPTER FOUR

BOLD AND TOLD – SEQUENCE DESIGN

4.1 Background

In Chapter 3, I discussed cervical tumor oxygenation MRI experiments. In order to assess oxygenation in human tissues with MRI, both T_1 and T_2* weighting/mapping techniques have been considered as potential methods for monitoring oxygenation status in health and disease. However, the technique to acquire both BOLD and TOLD contrast/mapping images simultaneously is not available on current clinical MR systems.

In my previous cervical tumor oxygenation experiments, some schemes were performed to verify the feasibility of acquiring BOLD and TOLD contrast signals in a dynamic fashion. For example, two individual sequences with T_1 and T_2* contrast weighting/mapping, respectively, were performed in an interleaved mode (Fig. 4.1(a)). This method is simple and straightforward. However, it has scaling issues for image post-processing and experiences MR scanner crashes occasionally due to the overloaded system (too many sequences planned). Therefore, in our cervical cancer studies, only the BOLD sensitive scan was performed dynamically under an oxygen challenge while the TOLD contrast/mapping scan was performed before (breathing in air) and after (breathing in 100% O_2) the BOLD scan (Figure 4-1(b)). This compromised strategy allowed me to generate both T_1 and T_2* maps in air and O_2 inhalation. But only BOLD dynamic changes can be monitored under an oxygen challenge.

I therefore designed and implemented a respiratory-triggered, free-breathing, interleaved TOLD and BOLD acquisition technique, by which both T_1-, T_2*-weighted signal changes and T_1-, T_2*-mapping series can be generated simultaneously during a single dynamic MRI scan during an oxygen challenge (Figure 4.1(c)). This technique improves the efficacy of tissue oxygenation MRI scans and requires no registration of the images or maps. The accuracy and reproducibility of this technique were tested on phantoms and 7 healthy volunteers. While abdominal organs were examined here, as an example, this method is likely applicable to quantitate tumor oxygenation.

4.2 Materials and Methods

4.2.1 Basic sequence scheme and quantification

A modified multi-shot multiple gradient-echo EPI sequence to acquire interleaved T_1 and T_2^* maps (ms-mGEPI-$T_{1,2*}$) is shown in Figure 4.2. It comprises odd and even segments. Each individual odd segment consists of three parts: (i) a 180° adiabatic inversion recovery (IR) prepulse, followed by a recovery delay time TI; (ii) a fat saturation prepulse (SPIR - Spectral Presaturation with Inversion Recovery), which is applied at the end of TI, (iii) a 90° RF pulse followed by a train of EPI acquisition at minimum echo time. In each even segment, the IR prepulse is skipped and the acquisition of three more EPI echo trains is added following the first echo with even echo spacing. The number of EPI echo trains is limited by tissue T_2* values and the EPI echo train length. The nominal repetition time (TR) is set at 6 seconds. The breathing motion is compensated by respiratory triggering and all

image data are acquired at the same phase of expiration cycles. Therefore, the actual TR in volunteer experiments is determined by the combination of nominal TR and actual respiratory cycle. To ensure a reasonable temporal resolution, a limited number of TIs are chosen so that T_1 can be estimated within an acceptable time. In this study an IR segment and a non-IR segment pair were used to calculate T_1 and T_2* of tissues.

Assuming that the longitudinal magnetization is completely inverted by the IR prepulse at the beginning of odd segments and the respiratory cycle duration is constant, then the signal intensity images for the single echo of the IR sequence (odd segment) and multiple echoes of non-IR sequence (even segment) are:

$$\text{IR Sequence:} \quad S_{IR}(TE_1) = S_0\left(1 - 2\cdot e^{-\frac{TI}{T_1}} + e^{-\frac{TR}{T_1}}\right)\cdot e^{-\frac{TE_1}{T_2^*}} \qquad [4\text{-}1]$$

and

$$\text{Non} - \text{IR sequence:} \quad S_{non-IR}(TE_i) = S_0\left(1 - e^{-\frac{TR}{T_1}}\right)\cdot e^{-\frac{TE_i}{T_2^*}} \quad (i = 1, 2 \ldots) \qquad [4\text{-}2]$$

where S_0 is the fully relaxed signal, when TR >> T_1; TI is the inversion recovery delay time; TE_1 and TE_i are the first and later echo times, respectively.

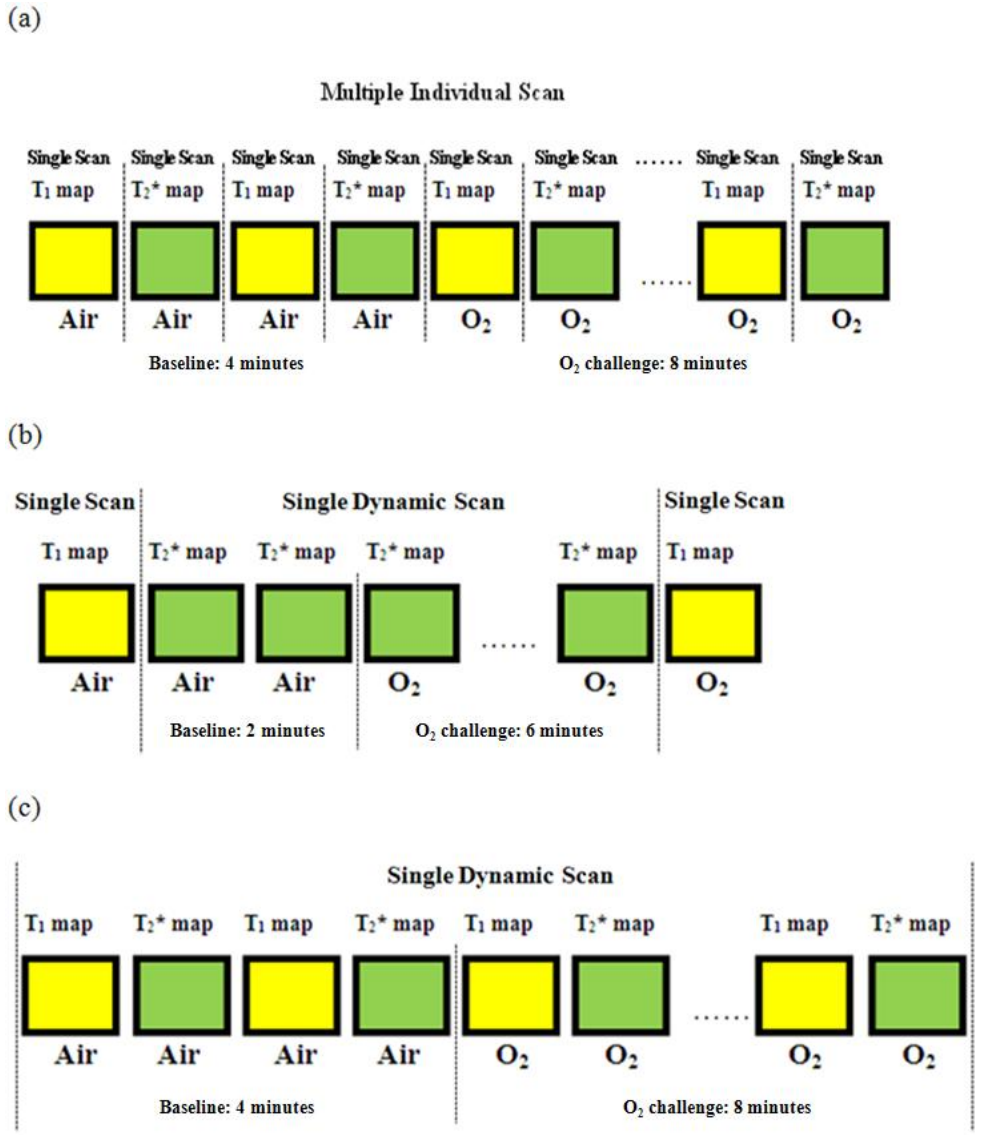

Figure 4.1 Typical T_1-T_2* acquisition strategies. (a) Multiple individual T_1 and T_2* scans repeated in an interleaved mode. (b) Traditional strategy for tissue/tumor oxygenation studies. Only T_1/T_2* dynamic scan was performed. (c) New developed strategy for T_1-T_2* acquisition in a single dynamic scan.

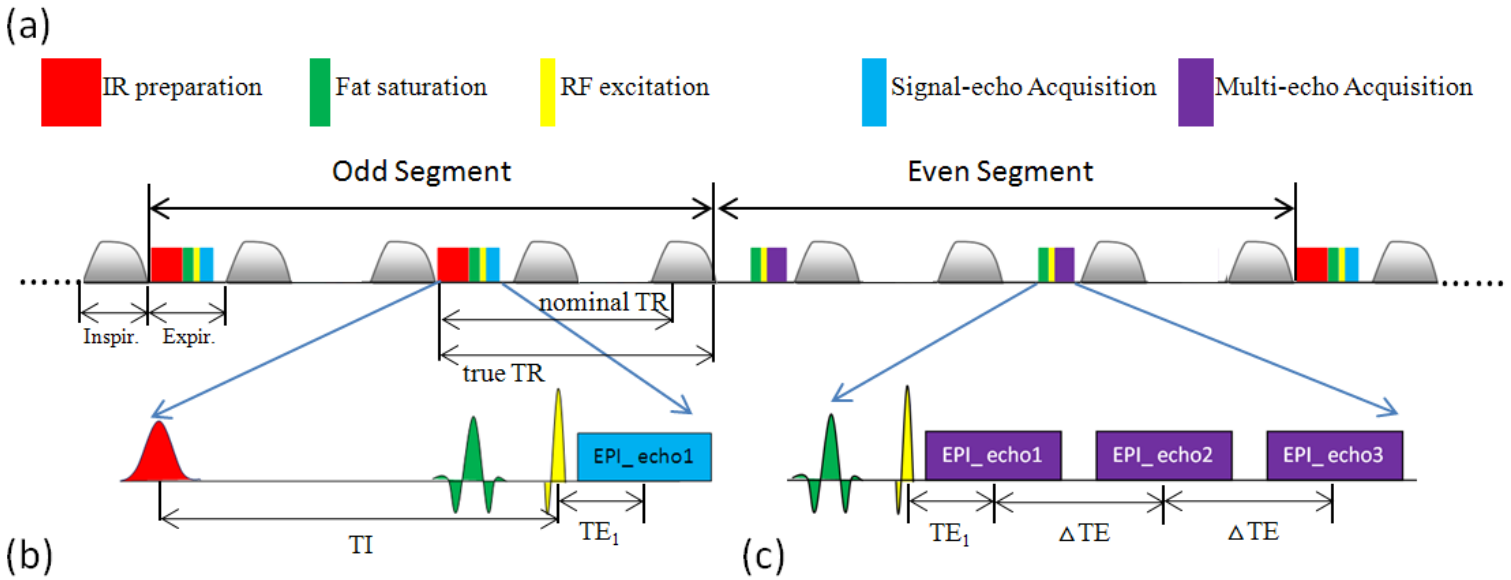
(a)
IR preparation
Fat saturation
RF excitation
Signal-echo Acquisition
Multi-echo Acquisition
Odd Segment
Even Segment
Inspir.
Expir.
nominal TR
true TR
EPI_ echo1
TI
TE1
(b)
EPI_ echo1
EPI_ echo2
EPI_ echo3
TE1
ΔTE
ΔTE
(c)

Figure 4.2 Schematic diagram of the ms-mGEPI-$T_{1,2*}$ sequence. (a) Respiratory-triggered, modified multi-shot multiple gradient-echo EPI sequence (ms-mGEPI-$T_{1,2*}$). (b) Pulse sequence order in odd segment, where IR preparation pulse with optimal TI is followed by fat saturation pre-pulse and a single gradient echo EPI acquisition is performed after 90° RF excitation. (c) Pulse sequence order in even segment, where fat saturation pre-pulse is followed by 90° RF excitation and multiple gradient echo acquisition.

Each pair of first echo images from two successive segments is used to generate T_1 maps using the iterative method (Zaharchuk, Martin et al. 2005; Zaharchuk, Busse et al. 2006). Here, the relationship between the ratio of signal intensity and T_1 at a fixed TE_1 can be expressed as

$$\text{Ratio} = \frac{S_{IR}(TE_1)}{S_{non-IR}(TE_1)} = \frac{1-2\cdot e^{-\frac{TI}{T_1}}+e^{-\frac{TR}{T_1}}}{1-e^{-\frac{TR}{T_1}}} \qquad [4\text{-}3]$$

where the TI and TR are known, allowing estimation of the only unknown, T_1, on a voxel-by-voxel basis for each time point. Variations in other MR parameters, such as proton density or T_2^*, do not affect the ratio of S_{IR} to $S_{non\text{-}IR}$ or the T_1 value. Moreover, in order to maximize the signal change produced by the T_1 change induced by breathing 100% oxygen, as compared to breathing room air, the optimal recovery delay time TI for the specific tissue can be chosen (Chen, Jakob et al. 1998). In this study, the optimal TI value was set equal to the mean of T_1 of renal cortex.

T_2* measurements can be derived from multiple echo images acquired in the even segments. Using a Levenberg-Marquardt algorithm on a voxel-by-voxel basis, the measured signal intensities in each voxel can be fitted to a two-parameter equation:

$$S_{non-IR}(TE_i) = S_0' \cdot e^{-\frac{TE_i}{T_2^*}},\ S_0' = S_0\left(1 - e^{-\frac{TR}{T_1}}\right) \quad [4\text{-}4]$$

where S_0' is the baseline signal intensity that would be obtained during the steady state with a given relaxation time TR. The oxygen-sensitive T_2*-weighted sequence can be optimized by choosing an echo time at the mean T_2* of the region of interest (ROI) (Posse, Wiese et al. 1999).

4.2.2 MRI investigations

All scans were performed on a Philips Achieva 3.0 T MR system (Philips Medical Systems, Best, Netherlands) using a six-element cardiac phased array coil. A 2D implementation of the ms-mGEPI-$T_{1,2^*}$ sequence was used to maintain reasonable scan time ($\alpha = 90°$, actual TR ≈ 6 ~ 8 s, TE_1 = 6.4 ms, ΔTE = 11.2 ms, TI = 1200 ms, Echo Train Length (ETL) = 15, spatial resolution = 3 × 3 × 5 mm^3, SENSE factor = 2, FOV = 220 × 220 mm^2 and bandwidth ≈ 2500 Hz), with temporal resolution of 24 s for the phantom studies, and around 24~32 s for volunteer studies depending on the respiratory rate. For validation tests, an inversion recovery half-Fourier acquisition single-shot turbo spin-echo (IR-HASTE) sequence with the same geometric parameters (2D half-Fourier spin echo, TR/TE = 10000/5.6 ms, recovery delay = 300, 600, 900, 1200, 1500, 1800 ms) was used for T_1 quantification and a conventional multiple gradient-echo (mGRE) sequence (TR/TE = 60/3.2 ms, echo spacing = 5.6 ms, 8 echoes) was applied for T_2* quantification.

Simulations

Numerical simulation of the variation of the T_1 measurements due to fluctuations in respiration rate was performed by using the iterative method (Zaharchuk, Martin et al. 2005). As seen in Eqs. [4-1] and [4-2], the actual TR must be known to obtain the correct T_1 values. The influence of TR variability between 4 s and 9 s was simulated for various T_1 values. Specifically, a nominal TR value was set at 7.5 s, and 4 different T_1 relaxation times were selected 900 ms, 1200 ms, 1300 ms, and 1500 ms representing typical T_1 of paraspinal muscle, spleen, renal cortex, and renal medulla, respectively.

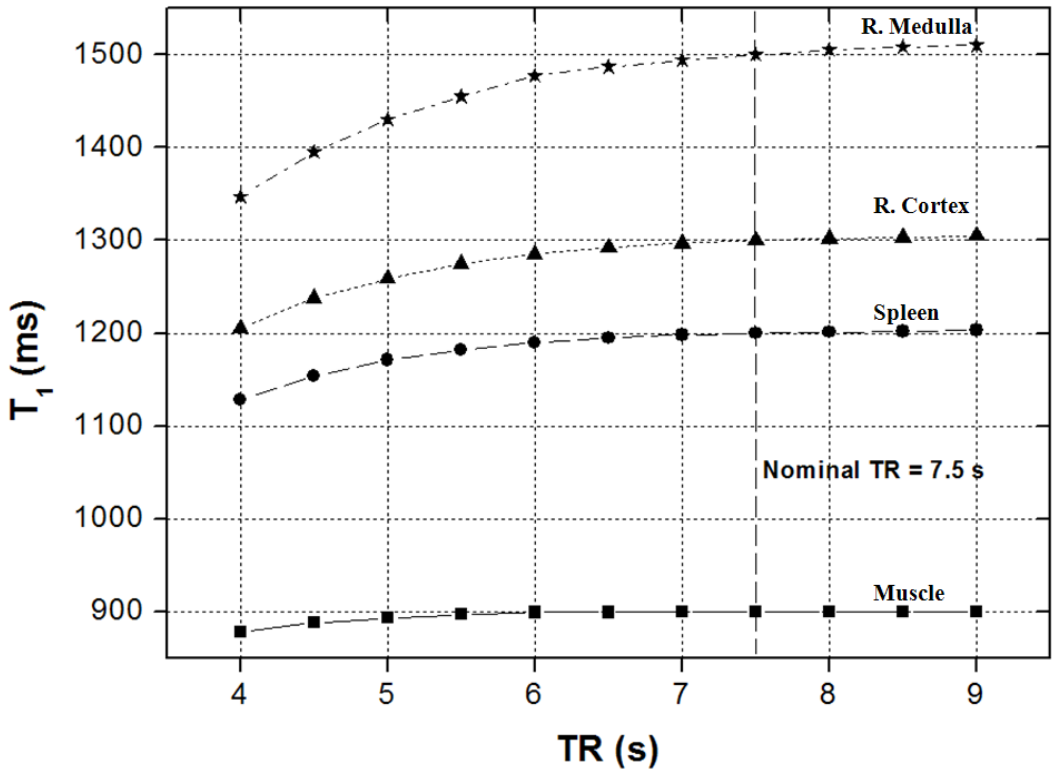

Figure 4.3 Simulation of the variation of T_1 measurements. Measuring T_1 with a nominal TR = 7.5 s would result in T_1 variation as a function of actual TR.

Phantoms

Both the ms-mGEPI-$T_{1,2*}$ sequence and the conventional sequences were tested on 10 phantoms that were constructed of identical glass bottles with different gadolinium concentrations of 0.04, 0.08 (two), 0.13 (two), 0.17, 0.25 (two), and 0.5 (two) mM providing T_1 values from 300 to 1700 ms and T_2* values of 50 to 140 ms. A simulated respiration with a cycle of 6 s was used to provide a trigger. MR imaging was separately performed on each bottle positioned at the center of the coil. To evaluate the performance and accuracy of the new method, an IR-HASTE scan and an mGRE scan were performed prior to the ms-mGEPI-$T_{1,2*}$ scan.

Volunteers

This study was approved by the Institutional Review Board and written informed consent was obtained from all volunteer subjects prior to the MR examination. Seven healthy volunteers (5 male, 2 female) with an age range of 26-55 years (mean age, 35.4 years) were imaged. Volunteers were examined during room air breathing followed by 100% oxygen (15 L/min), which was administered via a Hudson mask (Hudson RCI, model 1040; Temecula, CA, USA) from which the metallic nose piece had been removed. Arterial pressure of oxygen (SaO_2) and heart rate were monitored throughout the experiment using a pulse oximeter (In vivo 4500 MRI, In vivo Research Inc., Orlando, FL). The procedure was explained to the volunteer**.** The subjects were advised to breathe gently and freely throughout the entire dynamic series and measurements were acquired during expiration phases with respiratory triggering. No adverse events were reported.

After a survey and a SENSE reference scan, conventional quantification scans (IR-HASTE for T_1 and mGRE for T_2* each with breath-hold) were acquired in the appropriate coronal plane including spleen, kidney, and paraspinal muscle with little bowel present. The ms-mGEPI-$T_{1,2*}$ scan with oxygen challenge was then performed in the same location. Ten baseline measurements were collected, while breathing room air (21% O_2), followed by 20 with O_2 delivered at a rate of 15 L/min. Total scanning time for the oxygen study was about 14 minutes. In addition, five volunteers were scanned twice, on successive occasions, to investigate the reproducibility of measurements. Anatomic landmarks were used to reproduce the same imaging planes. For assessment of reproducibility, the agreement of measurements performed at different times was determined using Bland-Altman analysis (Bland and Altman 1986).

Image and Statistical Analysis

The relaxation times in this study were measured using in-house software developed by me using IDL (Interactive Data Language; Research Systems, Boulder, CO) and ImageJ (U.S. National Institutes of Health, Bethesda, Maryland). To validate the new technique, in phantom studies, a homogeneous ROI was chosen on the T_1 and T_2* maps for each phantom. The ROIs were obtained in the same location for each relaxation map. A Bland-Altman plot was used to compare the T_1 and T_2* variability between the conventional quantification methods (IR-HASTE for T_1 and mGRE for T_2*) and the ms-mGEPI-$T_{1,2*}$ sequence. This method is more suitable for assessment of reproducibility of clinical measurements (Hanneman 2008) and comparison of a new measurement technique with an established one

(Bland and Altman 1986) than by using correlation coefficients. The coefficient of variation was defined as the standard deviation (SD) of the differences between the two different measurements divided by their mean, and expressed as a percentage.

On images of volunteers, four different ROIs were drawn in the renal cortex, renal medulla, spleen, and paraspinal muscle for each volunteer (Fig. 4a). T_1 and T_2* values were measured in ROIs of the calculated relaxation time maps and compared with reference values calculated using conventional methods. A Bland-Altman plot was used to assess the reproducibility of scans with the new technique and a linear analysis was applied for comparing the T_1 and T_2* variability between the two methods.

The tissue oxygenation MRI data were analyzed in two ways: 1) on a voxel-by-voxel basis to generate maps of relaxation rate (R_1, R_2*) values before and during oxygen inhalation, and 2) in specific ROIs to reflect oxygen-induced signal intensity change at each time point. Masks were applied on relaxation rate maps to improve the visualization of areas of abdominal organs. For the T_1-T_2*-weighted signal intensity change analysis, ROIs drawn in the baseline image were copied in all T_1-T_2* weighted images. The relative signal change can be defined: $\Delta S = (S(t) - S_0) / S_0$, where S(t) is the signal intensity in the ROI at time t, and S_0 is the average baseline signal intensity (measured from the average of 10 baseline images) in the same ROI. The dynamic oxygen-induced signal changes for both T_1 and T_2* weighted images in abdominal organs were thus generated.

4.3 Results

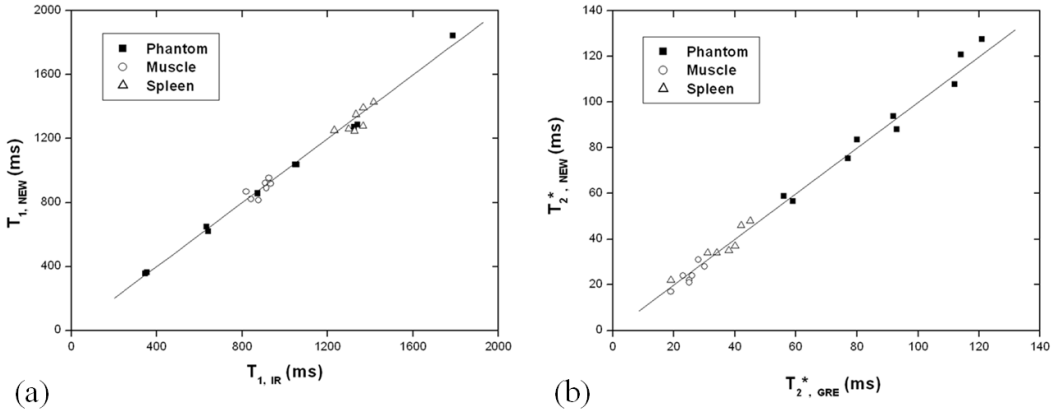

Figure 4.4 Comparison of relaxation times measured using new combined or traditional sequences. (a) T_1 (IR-HASTE ($T_{1, IR}$) vs. new sequence ($T_{1, NEW}$)): r= 0.98, P<0.0001; N = 24 and (b) T_2* (mGRE (T_2*$_{, GRE}$) vs. new sequence (T_2*$_{, NEW}$)): r = 0.97; P<0.0001; N = 24. The solid lines indicate the line of identity. Human data were obtained during baseline air breathing.

TABLE 4.1

Comparison of tissue T_1, T_2* results obtained from T_{NEW}, Conv, and Lit at 3 T.

Tissue	T_1 (ms)			T_2^* (ms)		
	Lit	Conv	T_{NEW}	Lit	Conv	T_{NEW}
P. muscle	898 ± 33	888 ± 44	884 ± 52	N.A.	24 ± 4	24 ± 5
Spleen	1328 ± 31	1334 ± 59	1316 ± 74	N.A.	36 ± 9	37 ± 9
R. cortex	1142 ± 154	1174 ± 157	1205 ± 171	~55(Pruijm, Hofmann et al. 2010)	52 ± 8	54 ± 11
R. medulla	1545 ± 142	1531 ± 166	1512 ± 189	~47(Boss, Martirosian et al. 2009)	39 ± 10	38 ± 13

P. muscle = paraspinal muscle;
R. cortex = renal cortex;
R. medulla = renal medulla;
Lit = literature (de Bazelaire, Duhamel et al. 2004);
Conv = conventional
T_{NEW} = ms-mGEPI-$T_{1,2^*}$
N.A. = not available;
± represents standard deviation for abdominal tissues over all subjects.

TABLE 4.2

T_1 and T_2* measured in human volunteers during baseline air breathing and with oxygen challenge.

	P. Muscle	Spleen	R. Cortex	R. Medulla
$T_{1, air}$ (V1)	917 ± 16	1252 ± 24	1086 ± 32	1414 ± 38
$T_{1, oxy}$ (V1)	924 ± 17	1174 ± 25	1026 ± 35	1445 ± 41
$T_{1, air}$ (V2)	953 ± 18	1247 ± 27	1345 ± 40	1623 ± 45
$T_{1, oxy}$ (V2)	951 ± 20	1157 ± 24	1267 ± 37	1689 ± 49
$T_{1, air}$ (V3)	891 ± 17	1278 ± 26	1172 ± 37	1735 ± 44
$T_{1, oxy}$ (V3)	887 ± 15	1199 ± 28	1115 ± 33	1698 ± 46
$T_{1, air}$ (V4)	815 ± 14	1393 ± 30	1302 ± 34	1476 ± 39
$T_{1, oxy}$ (V4)	823 ± 13	1304 ± 30	1232 ± 40	1462 ± 42
$T_{1, air}$ (V5)	868 ± 16	1260 ± 23	1235 ± 34	1522 ± 42
$T_{1, oxy}$ (V5)	866 ± 18	1172 ± 25	1163 ± 38	1551 ± 44
$T_{1, air}$ (V6)	922 ± 20	1429 ± 29	1103 ± 36	1498 ± 42
$T_{1, oxy}$ (V6)	908 ± 19	1301 ± 29	1039 ± 34	1477 ± 45
$T_{1, air}$ (V7)	822 ± 17	1351 ± 30	1437 ± 41	1699 ± 47
$T_{1, oxy}$ (V7)	835 ± 16	1243 ± 28	1353 ± 42	1726 ± 49
Mean $T_{1, air}$	884 ± 52	1316 ± 74	1240 ± 130	1567 ± 121
Mean $T_{1, oxy}$	885 ± 47	1221 ± 62	1171 ± 121	1578 ± 123
P(T_1, mean)	0.97	0.02†	0.32	0.86

	P. Muscle	Spleen	R. Cortex	R. Medulla
$T_2^{*}{}_{, air}$ (V1)	22.6 ± 0.8	36.6 ± 1.2	53.6 ± 3.9	37.2 ± 3.2
$T_2^{*}{}_{, oxy}$ (V1)	23.5 ± 1.0	37.2 ± 0.9	56.1 ± 3.6	39.8 ± 3.1
$T_2^{*}{}_{, air}$ (V2)	23.9 ± 1.2	37.1 ± 1.4	51.9 ± 3.5	39.0 ± 3.0
$T_2^{*}{}_{, oxy}$ (V2)	23.1 ± 0.9	35.9 ± 1.1	48.4 ± 3.8	41.4 ± 3.1
$T_2^{*}{}_{, air}$ (V3)	21.1 ± 0.8	40.5 ± 1.4	51.8 ± 3.7	31.5 ± 3.3
$T_2^{*}{}_{, oxy}$ (V3)	20.4 ± 0.8	38.8 ± 1.3	53.7 ± 3.6	34.3 ± 2.9
$T_2^{*}{}_{, air}$ (V4)	20.0 ± 0.7	26.5 ± 1.0	66.5 ± 4.0	28.7 ± 2.7
$T_2^{*}{}_{, oxy}$ (V4)	21.2 ± 1.1	27.4 ± 0.8	68.7 ± 3.9	27.9 ± 2.8
$T_2^{*}{}_{, air}$ (V5)	26.8 ± 0.9	31.4 ± 1.1	45.7 ± 3.3	34.8 ± 2.9
$T_2^{*}{}_{, oxy}$ (V5)	27.6 ± 1.2	29.7 ± 1.2	47.8 ± 3.5	36.7 ± 3.1
$T_2^{*}{}_{, air}$ (V6)	20.5 ± 1.0	26.4 ± 1.1	41.4 ± 3.4	40.3 ± 2.8
$T_2^{*}{}_{, oxy}$ (V6)	21.3 ± 0.9	27.0 ± 1.1	39.9 ± 3.7	43.6 ± 3.0
$T_2^{*}{}_{, air}$ (V7)	27.7 ± 1.1	43.7 ± 1.3	61.3 ± 4.2	52.1 ± 3.5
$T_2^{*}{}_{, oxy}$ (V7)	26.8 ± 1.0	41.9 ± 1.4	63.5 ± 4.0	50.9 ± 3.4
Mean; $T_2^{*}{}_{, air}$	23.2 ± 3.1	34.6 ± 6.7	53.2 ± 8.6	37.7 ± 7.6
Mean; $T_2^{*}{}_{, oxy}$	23.4 ± 2.8	34.0 ± 5.9	54.0 ± 9.8	39.2 ± 7.3
P(T_2*, mean)	0.90	0.86	0.87	0.71

Air vs. Oxy	P. Muscle	Spleen	R. Cortex	R. Medulla
$P(T_1(V1))$	0.48	<0.001†	0.02†	0.21
$P(T_1(V2))$	0.86	<0.001†	0.01†	0.14
$P(T_1(V3))$	0.67	<0.001†	0.03†	0.19
$P(T_1(V4))$	0.33	<0.001†	0.02†	0.56
$P(T_1(V5))$	0.84	<0.001†	0.01†	0.27
$P(T_1(V6))$	0.24	<0.001†	0.04†	0.42
$P(T_1(V7))$	0.20	<0.001†	0.02†	0.35
$P(T_2^*(V1))$	0.12	0.35	0.28	0.18
$P(T_2^*(V2))$	0.22	0.13	0.13	0.20
$P(T_2^*(V3))$	0.16	0.18	0.39	0.15
$P(T_2^*(V4))$	0.09	0.22	0.36	0.63
$P(T_2^*(V5))$	0.22	0.08	0.31	0.30
$P(T_2^*(V6))$	0.20	0.37	0.48	0.12
$P(T_2^*(V7))$	0.17	0.15	0.37	0.59

†: < 0.05 (significantly different)
V(1)……V(7): Volunteer number

A simulation of apparent T_1 calculated with a nominal TR = 7.5 s versus actual TR for 4 different T_1 values (Fig. 4.3) indicates little error when TR > 6 s (< 1.5%). For short TR (< 5 s) significant variation (> 5%) occurs and thus the minimum TR was set to 6 s, to ensure the accuracy of T_1 measurements for human abdominal experiments.

The new sequence was successfully implemented in both phantoms and human volunteers. The T_1 values measured for phantoms and human abdominal tissues (spleen and paraspinal muscle) by both traditional and new techniques were strongly correlated (r = 0.98; P<0.0001; n = 24**;** Fig. 4.4a). Likewise for the mean T_2* values (r = 0.97; P < 0.0001; n = 24; Fig. 4.4b). Moreover, Bland-Altman analysis indicated that there was no significant systematic deviation (Figure 4.5). The mean difference in the T_1 value obtained using the conventional IR-HASTE and the new sequence was –0.6% with 95% confidence interval 5.9% (Fig. 4.5a). The mean difference in T_2* using the mGRE sequence and new sequence was 0.4% with 95% confidence interval 8.6% (Fig. 4.5b).

The relaxation times of human tissues (paraspinal muscle, spleen, renal cortex and renal medulla) in the volunteers are in good agreement with both literature reports and those obtained using the conventional methods (Table 4.1). The results of the interstudy variability of the ms-mGEPI-$T_{1,2*}$ sequence are summarized in Figure 4.5c and 4.5d. The coefficient of variation of the spleen and muscle T_1 and T_2* values of 5 healthy volunteers was 5.0% for T_1 and 8.4% for T_2*.

No significant complications occurred during the human studies, although three of 7 volunteers complained of dry throat caused by strong flow rate of oxygen. The oxygen induced tissue relaxation time changes on a subject-by-subject basis are shown in Table 4.2.

T_1 relaxation times of spleen and renal cortex significantly decreased in every volunteer in response to oxygen challenge, but only the overall change in spleen was statistically significant ($P < 0.05$), as shown for a typical volunteer (Fig. 4.6, 4.7 and 4.8). No significant T_1 change was observed in paraspinal muscle and renal medulla ($P > 0.8$). T_2* relaxation times of these tissues during air and oxygen breathing did not differ significantly ($P > 0.7$), however some regions of renal medulla in 5 of 7 volunteers showed an evident increase in T_2* with oxygen.

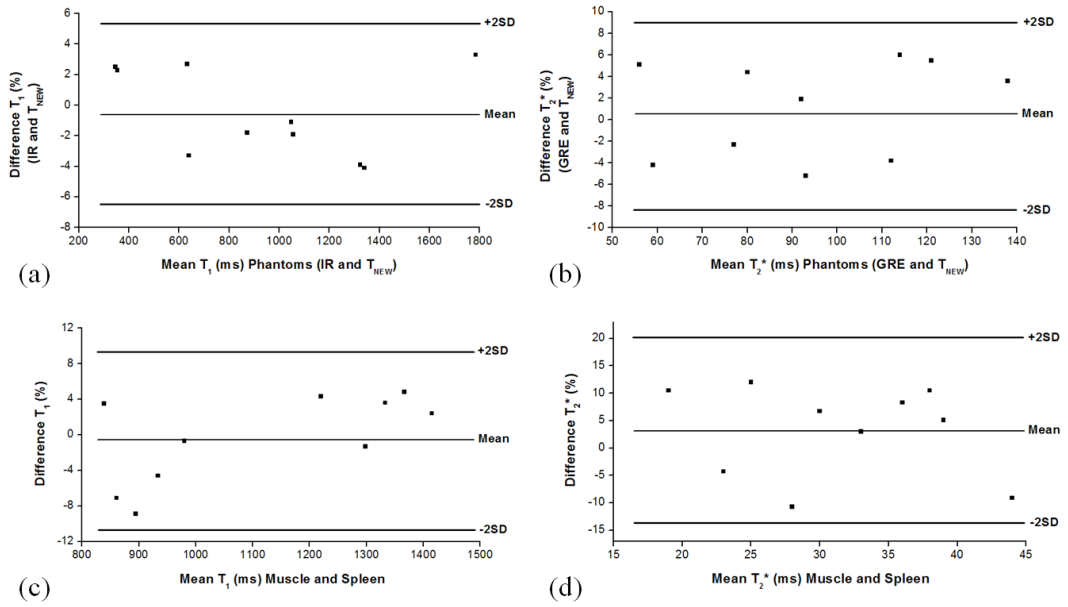

Figure 4.5 Comparison of T_1 and T_2* measurements using Bland-Altman analysis.
Phantom tests: Differences between phantom T_1 and T_2* measurements based on new and traditional measurements: (a) T_1 comparison with IR-HASTE ; (b) T_2* comparison with mGRE
Human volunteers: Reproducibility of new sequence: results of muscle and spleen on successive occasions; (c) T_1 and (d) T_2* relaxation time measurements using new sequence.

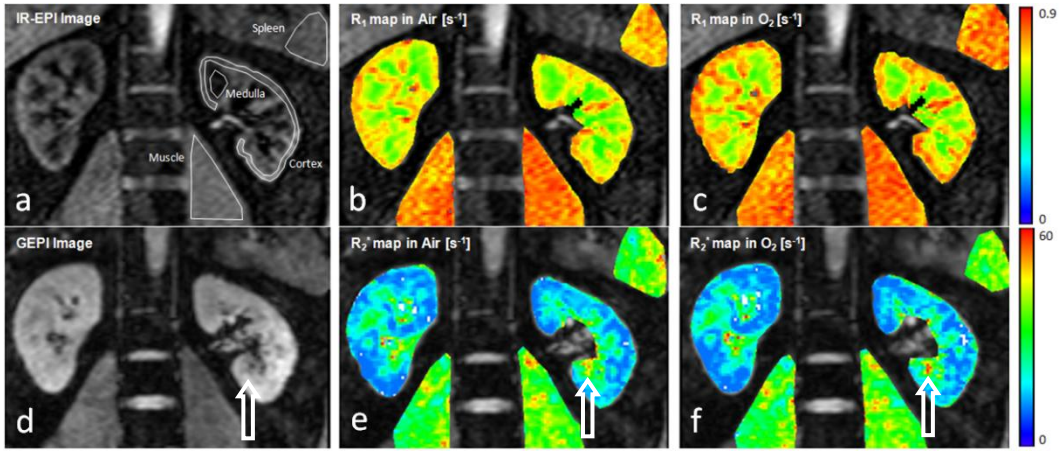

Figure 4.6 Oxygen-induced changes in R_1 and R_2^* in a healthy volunteer. The T_1-weighted image (a) and the T_2^*-weighted image (d) demonstrate the normal anatomy of the abdominal organs. Compared to the R_1 maps acquired while breathing air (b), a significant increase in R_1 was seen in spleen and renal cortex when O_2 was inhaled (c). $80R_2$* maps show minimal change between air breathing (e) and O_2 (f). R_1 maps clearly reveal differences between renal medulla and cortex, while the muscle and spleen are relatively homogeneous. Arrows in (d), (e), and (f) point at region of other renal tissues such as calyx or suppressed fat tissues.

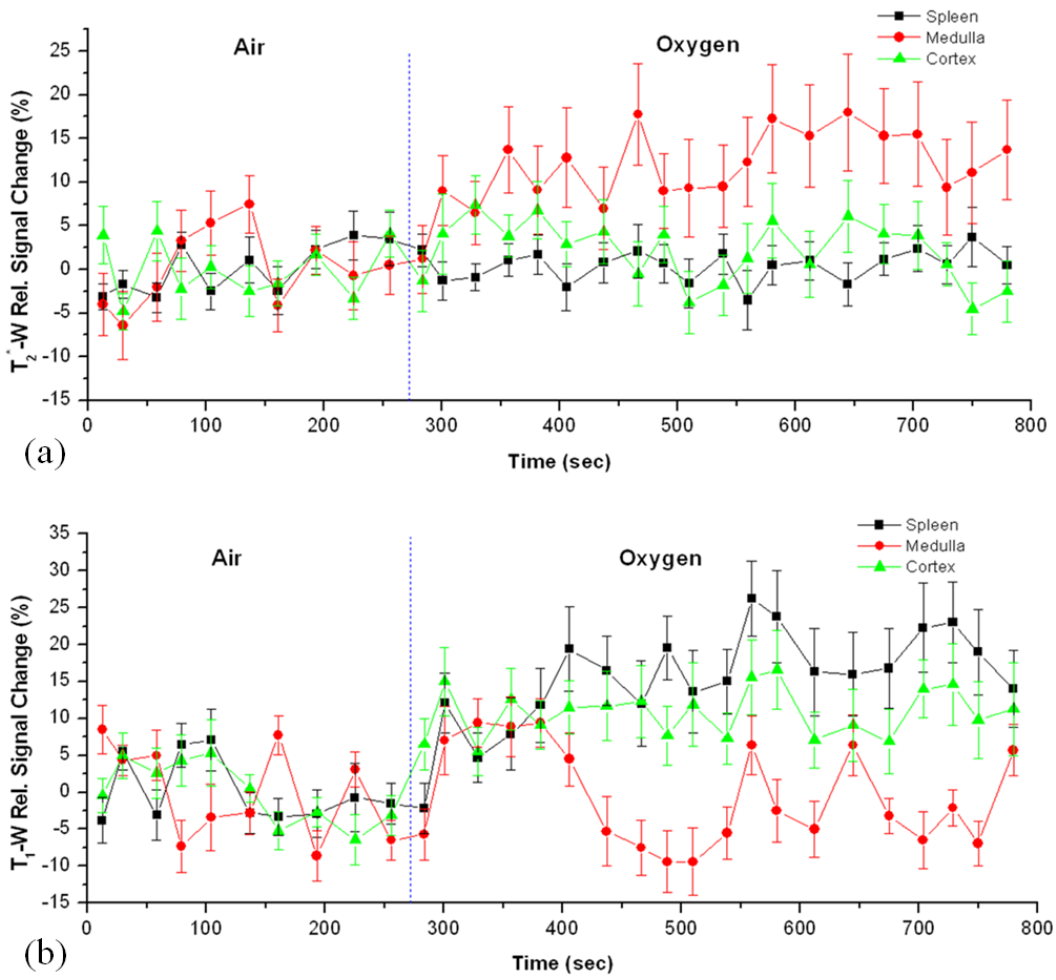

Figure 4.7 BOLD and TOLD response to oxygen challenges in a human volunteer. Time-intensity changes (%) show response to oxygen challenge for a healthy volunteer. The abdominal organs (spleen, renal cortex and renal medulla) show different BOLD (a) and TOLD (b) responses to oxygen breathing. The data represent the mean relative signal ± standard deviation in ROIs.

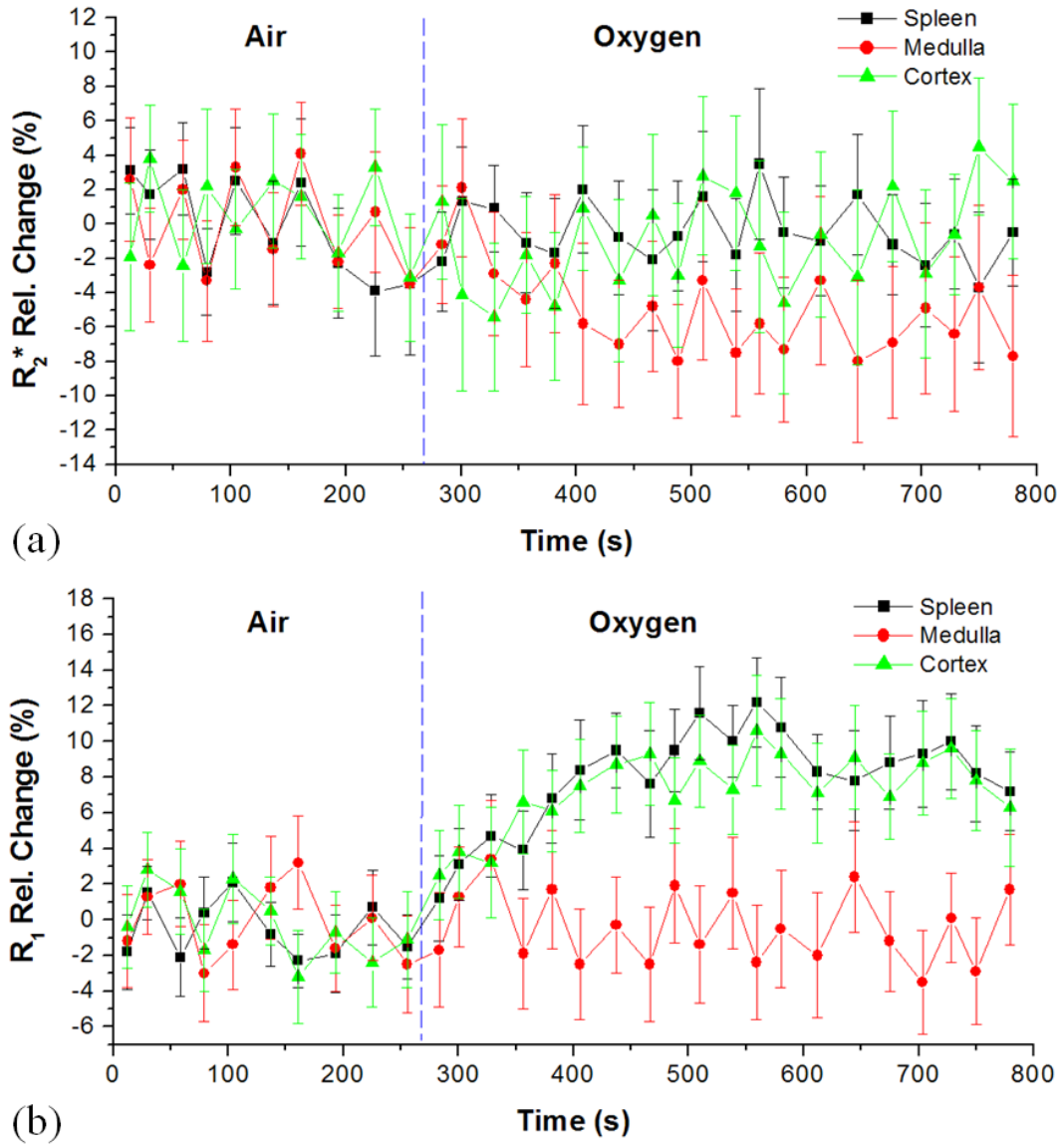

Figure 4.8 BOLD and TOLD response to oxygen challenges in a human volunteer. Differential (a) BOLD and (b) TOLD relaxation rate responses (%ΔR) to oxygen challenge in the abdominal organs (spleen, renal cortex and renal medulla). The data represent the mean relative relaxation rate ± standard deviation in ROIs of a single healthy volunteer.

Each tissue showed stable values during baseline air breathing with typical variation < 8%, *e.g.*, for the volunteer #5 shown in Figure 4.7, paraspinal muscle T_1 = 868 ± 16 ms, T_2*

= 26.8 ± 0.9 ms, spleen T_1 = 1260 ± 18 ms, T_2* = 31.4 ± 1.1 ms, renal cortex T_1 = 1235 ± 34 ms, T_2* = 45.7 ± 3.3 ms, renal medulla T_1 = 1522 ± 42 ms and T_2* = 34.8 ± 2.9 ms. There was little variation in data between individuals (Table 4.1). Spleen and renal cortex showed minimal T_2* response to oxygen challenge, while renal medulla responded rapidly with significant increase within 90 s and settling on an elevated plateau. T_1 response was somewhat different showing response within 2 minutes for all tissues. For spleen and renal cortex signal remained significantly elevated, whereas for renal medulla no evident change was observed after the transient phase (Figure 4.7). The corresponding relaxation rate changes are shown in Figure 4.8. For spleen and renal cortex ΔR_1 remained significantly elevated, but ΔR_2* of renal medulla settled on a reduced plateau.

4.4 Discussion

This chapter demonstrates the feasibility of interleaved TOLD and BOLD MRI in a single dynamic scan, allowing the simultaneous measurement of oxygen induced relaxation time changes in human abdominal tissues. The measured relaxation times were consistent with those obtained using traditional pulse sequences and with previous reports in the literature.

The accuracy of T_1 quantification depends on the steadiness of actual TR values under respiratory triggering. Choosing a sufficiently long TR to provide fully recovered signal ($\geq 5 \times T_1$) can avoid this problem and we set the minimum TR = 6 s ($\geq 5 \times T_1$ of renal cortex) combined with the respiratory triggering technique, which ensured an actual TR

between 6 and 9 s. Therefore, any variation in TR should have negligible effect, as simulated (Fig. 4.3) and the calculated T_1 depended on the signal intensity ratio of the successive images acquired with and without the IR prepulse. This proposed method is suitable for most current abdominal tissue oxygenation studies. However, in other tissues such as CSF studies (T_1 > 3 s) an oxygenation study would require longer TIs and longer relaxation recovery delays. We also note that the accuracy of T_1 estimation would be reduced if TI is close to a specific T_1 (~0.7·T1), due to low SNR in ms-IR-EPI images. Therefore, T_1 relaxation times in tissues of interest should be estimated a priori and the chosen TI should avoid "null-point" regions of target tissues. In this work, TI = 1.2 s to provide effective estimation of abdominal tissues.

The number of echoes influences the accuracy of T_2*. However, the maximum echo number is limited by the EPI echo train length and tissue T_2*. The multi-shot EPI technique provides a tradeoff between number of echoes and imaging time. Longer echo train length could reduce overall imaging time but would also cause more severe EPI-related distortion (Jezzard and Balaban 1995). Here, a simple monoexponential model with four time points provided accurate estimates of T_2* values in both phantom and human experiments. However, unlike the mGRE scan which could be performed during a single breath-hold, the ms-mGEPI-$T_{1,2*}$ scan may suffer from irregular abdominal motion during successive breaths potentially inducing signal dephasing artifacts such as spatial blurring and ghosting. Therefore, some late echo images were discarded for accurate T_2* estimation. I observed an R_2* decrease in some regions of the renal medulla with oxygen challenge, but the overall

changes in R_2* were not significant. This may represent tissue heterogeneity or partial volume effects between outer medulla and inner medulla.

Other respiratory compensation techniques such as gating and navigator might be a feasible strategy for this study. However, during the lengthy dynamic scan, I observed large respiratory rate variability, unexpected body motion, or exhalation location variability occasionally, especially when switching the gas supply. Data acquisition in such situations might be affected if gating or navigator technique is used. Therefore, respiratory triggering technique is more reliable in this study.

The observed relaxation times agreed with those reported previously for human volunteers at 3 T, by Bazelaire et al.(de Bazelaire, Duhamel et al. 2004) for T_1 in each of the tissues and by Boss et al. (Boss, Martirosian et al. 2009) and Pruijm et al. (Pruijm, Hofmann et al. 2010) for T_2*/R_2* in kidney (Table 1). Boss et al. also reported a significant increase in T_2* of renal medulla accompanying oxygen breathing challenge. It is reported that BOLD effects are greater at higher field (Garcia-Eulate, Garcia-Garcia et al. 2011). My observations in spleen and renal cortex were smaller BOLD responses at 3 T than previously reported at 1.5 T, though neither change was significant (O'Connor, Naish et al. 2009). Similarly, previous reports indicated a change in T_1 in spleen of 13% with respect to oxygen challenge in the spleen, whereas we found only 7.2% change (Table 2). In renal cortex our observations closely matched O'Connor et al. at 1.5 T (7%) with oxygen challenge.

To facilitate human abdominal application, the T_1, T_2* mapping sequence was combined with respiratory-triggering to acquire quantitative dynamic maps of abdominal organs under free breathing. The first echo acquisition in both segments was performed at the

same respiratory phase and all echoes were acquired in the expiration period. Since both maps are produced in the same scan, there is no need for additional co-registration of the T_1 and T_2* maps. Image quality, spatial and temporal resolution (3×3 mm^2 and ~ 30 s) of both relaxation maps were sufficient to detect relatively small anatomical structures and oxygen-induced tissue relaxation time changes.

4.5 Summary

In conclusion, this work demonstrates the feasibility of simultaneous interleaved BOLD and TOLD measurements in human abdominal oxygen-sensitive MRI studies with respect to an oxygen challenge, within a single dynamic acquisition. The increase in R_1 is consistent with an increase in tissue oxygenation, whereas the reduction in R_2* indicates increased vascular oxygenation. My measurements are consistent with previous reports. This new technique provides improved time efficiency (whenever both measurements are needed) and will almost certainly produce accurate results when assessing a specific organ for both T_1 and T_2* data during oxygen challenge. Such measurements could have important application to assessing hypoxia and response to interventions with respect to treatment planning in radiation oncology.

CHAPTER FIVE

TOLD/BOLD MRI: RAPID ACQUISITION STRATEGIES

5.1 Background

The novel ms-mGEPI-T_{12}* sequence, described in Chapter Four, has shown promise in detection of BOLD and TOLD effects in human abdominal oxygen-sensitive MRI studies with respect to an oxygen challenge, within a single dynamic acquisition. However, there are some limitations of ms-mGEPI-T_{12}* sequence in the application of abdominal tissue oxygenation studies. For example, the temporal resolution is about 24~32 seconds which is adequate for abdominal tissue oxygenation studies. However, in other potential applications such as dynamic contrast enhanced MRI (DCE-MRI) higher temporal resolution is required to provide important perfusion information. Moreover, to ensure adequate temporal resolution in dynamic studies, limited time points are sampled on the recovery or relaxation curve (two TIs for T_1 and 4 echoes for T_2*) and this tradeoff may affect the accuracy of the relaxation parameter estimation.

Therefore, I designed and implemented an upgraded "ms-mGEPI-T_{12}*" sequence to improve the temporal resolution and increase data samples using a saturation-recovery multi-shot multi-gradient-echo EPI sequence (SR-ms-mGEPI-T_{12}*). This sequence allows flexible adjustment of saturation recovery time in both segments. With an additional fully recovered acquisition, a 3-point fitting algorithm can be used for T_1 quantification. This method is able

to accurately measure T_1 and T_2* with higher temporal resolution, making it applicable to dynamic measurement of tissue oxygenation in abdominal MRI studies.

Moreover this 3-point strategy can also be extended to estimation of T_1 by replacing an SR pre-pulse with an IR pre-pulse. Here, I call this 3-point SR-ms-mGEPI-T_{12}* "SR-based sequence", and called the corresponding IR pre-pulse sequence "IR-based sequence". Compared with the ms-mGEPI-T_{12}* sequence which is a 2-point method, the 3-point IR-based sequence should improve the accuracy of T_1 quantification without sacrificing temporal resolution.

5.2 Material and Methods

5.2.1 Pulse sequence design

The schematic RF diagram of SR-ms-mGEPI-T_{12}* is shown in Figure 5.1. The sequence is modified from the ms-mGEPI-T_{12}* sequence with the following changes. 1) In the even segment, the 180°, adiabatic, IR prepulse (hs_500_400_100) is replaced by a 90° non-adiabatic, presaturation pulse (rest2) followed by a gradient dephasing lobe and the saturation recovery delay interval τ_1. Four more EPI echo trains are added following the first echo with the fixed echo space ΔTE. The sequence is repeated to generate five complete image series, S_1 … S_5, with different echo times TE_i (i = 1…5). 2) In the odd segment, an additional presaturation pulse is added in the beginning of the preparation phase followed by the saturation delay time τ_2. The same echo spacing as the even segment is used. 3) An additional fully recovery sequence with the same geometric parameters is performed

following the dynamic SR-based sequence to acquire an extra sampling point on the T_1 recovery curves.

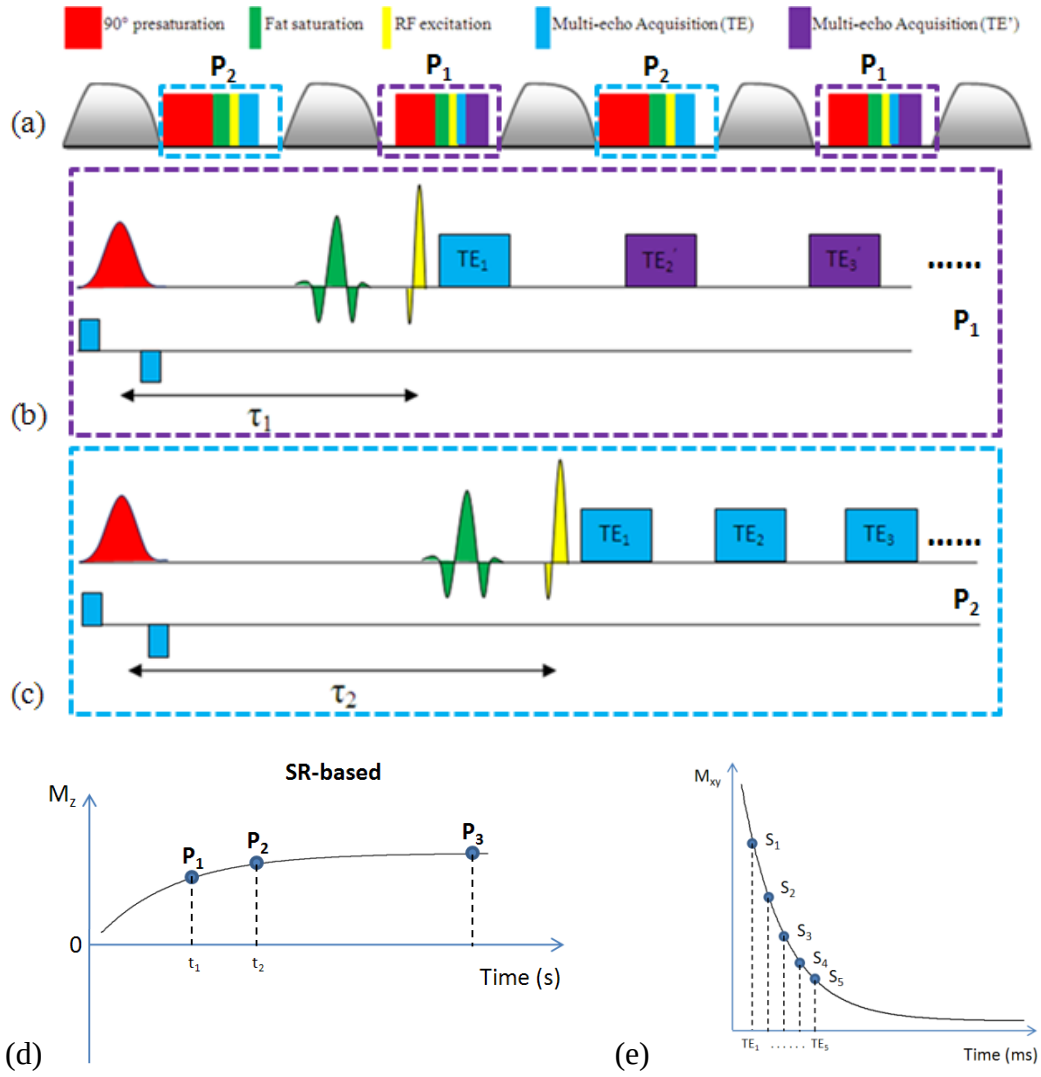

Figure 5.1 Schematic diagram of the SR-ms-mGEPI-T_{12}* sequence (SR-based sequence). (a) Respiratory-triggered, multi-shot multiple gradient-echo EPI sequence (SR-ms-mGEPI-$T_{1,2*}$). (b) Pulse sequence order for P_1 sampling with a delay time t_1. (c) Pulse sequence order for P_2 sampling with a delay time t_2. (d) Two points (P_1 and P_2) along saturation recovery curve are sampled by SR-based sequence for T_1 quantification. (e) Five points (S_1… S_5) along the relaxation curve are sampled by SR-based sequence for T_2* quantification.

Assuming that the longitudinal magnetization is completely destroyed by the saturation pulses at the beginning of the sequence and the respiration rate is approximately constant, then the signal intensity equation for a given saturation recovery time τ_i at the multiple echo times TE_j is:

$$S_i = S_0 \cdot (1 - \exp(-\tau_i/T_1)) \cdot \exp(-TE_j/T_2^*) \quad (i = 1, 2; \text{ and } j = 1, 2, 3, \ldots\ldots) \qquad [5\text{-}1]$$

And a fully recovered signal equation is:

$$S_3 = S_0 \cdot \exp(-TE_1/T_2^*) \qquad [5\text{-}2]$$

where S_0 is the fully relaxed signal, when $TR >> T_1$, representing the equilibrium longitudinal magnetization which does not vary with T_1 and only depends on proton density, imaging voxel dimension, magnetic field strength, and temperature (Slichter 1990).

As shown in Figure 5.1(d), the signal intensity of first echo images traces the saturation recovery curve at various delay times. For a dynamic SR-based scan, a limited number of saturation delay times are chosen, typically two, so that T_1 can be estimated with the required temporal resolution. Every two consecutive first echo images along with a fully recovery sample can be used to fit the Eq. [5-1] on the saturation recovery curve. Also, T_2^* measurements can be derived from multiple echo images acquired in the each segment by fitting the sampling points on T_2^* relaxation curve (Figure 5.1(e)).

This methodology can also be applied for the estimation of relaxation times using 3-point IR-based sequence. Three points, two samples obtained from every consecutive first echo image and one fully recovered sample, can be used to fit equation [4-1] on inversion recovery curve (Fig. 5.4(c)) and the same method used for SR-based sequence can be applied to estimation of T_2*.

5.2.2 MRI investigations

All scans were performed on a Philips Achieva 3.0 T MR system (Philips Medical Systems, Best, Netherlands) using a torso phased array coil. A 2D implementation of the SR-based sequence was used to maintain reasonable scan time ($\alpha = 90°$, actual TR ≈ 4 ~ 6 s, TE_1 = 6.4 ms, ΔTE = 11.2 ms, τ_1 = 600 ms, τ_2 = 1,300 ms, ETL (turbo-factor) = 9, spatial resolution = 3 × 3 × 5 mm^3, SENSE factor = 2, FOV = 280 × 280 mm^2 and bandwidth ≈ 2,500 Hz), with temporal resolution of 16 s for the phantom studies, and around 16~24 s for volunteer studies depending on the respiration rate. As a comparison, a 2D IR-based sequence was performed with the same geometric and contrast parameters, but different delay times and TRs (TI_1 = 1,300 ms, TI_2 = 1,800 ms, minimum TR = 6 s). For validation tests, an inversion recovery half-Fourier acquisition single-shot turbo spin-echo (IR-HASTE) sequence with the same geometric parameters (2D half-Fourier spin echo, TR/TE = 10,000/5.6 ms, recovery delay = 300, 600, 900, 1,200, 1,500, 1,800 ms) was used for T_1 quantification and a conventional mGRE sequence (TR/TE = 60/3.2 ms, echo spacing = 5.6 ms, 8 echoes) was applied for T_2* quantification.

Phantoms

The SR-based sequence, IR-based sequence and the conventional sequences were tested on 5 phantoms that were constructed of identical glass bottles with different gadolinium concentrations of 0.04 mM, 0.08 mM, 0.17 mM, 0.5 mM and 1 mM providing T_1 values in the range 300 ms to 1,700 ms and T_2* values of 50 ms to 140 ms. Simulated respiration rates with a cycle of 4 s for SR-based sequence and 8 s for IR-based sequence were used to provide triggers. MRI scans were separately performed on each bottle positioned in the center of the coil. To evaluate the performance and accuracy of the new methods, an IR-HASTE scan and an mGRE scan were performed prior to the SR- and IR-based scans.

Volunteers

This study was approved by the local IRB and written informed consent was obtained from 3 male subjects prior to the MR examinations. Volunteers were examined with room air breathing and the procedure was explained to the volunteer**.** Subjects were advised to breathe gently and freely throughout the entire dynamic series without oxygen challenge and measurements were acquired during expiration phases with respiratory triggering. After a survey and a SENSE reference scan, conventional quantification scans (IR-HASTE for T_1 and mGRE for T_2* in breath-hold) were acquired in the appropriate coronal plane including spleen, kidney, and paraspinal muscle with little bowel present. The SR- and IR-based scans were then performed separately. Scanning times for the SR-based scan and IR-based scan were about 7 minutes (dynamic number = 20) and 8 minutes (dynamic number = 10), respectively. In addition, to investigate the reproducibility of measurements, all 3 volunteers

were scanned twice with subject repositioning and a time interval of 10 minutes. Anatomic landmarks were used to reproduce the same imaging planes.

Image and Statistical Analysis

Relaxation times in this study were calculated using Origin 6 (OriginLab Corporation, Northampton, MA). To validate the new techniques, in phantom studies, ROIs were drawn on the T_1- and T_2*-weighted images for each phantom. A Bland-Altman plot was used to compare the T_1 and T_2* variability between the conventional quantification methods (IR-HASTE for T_1 and mGRE for T_2*) and the new sequences (IR- and SR-based sequences).

On images of volunteers, four different ROIs were drawn in the renal cortex, renal medulla, spleen, and paraspinal muscle for each volunteer (Figure. 5.2b). T_1 and T_2* values were measured in ROIs and compared with reference values calculated using conventional methods. A Bland-Altman plot was used to assess the reproducibility of scans with the new techniques and a linear analysis was applied for comparing the T_1 and T_2* variability between the two methods.

5.3 Results

Both new developed IR-based and SR-based sequences were successfully implemented in both phantoms (Fig. 5.6) and human volunteers (Fig. 5.4, 5.5 and 5.7). The T_1 values measured for phantoms and human abdominal tissues by traditional and new techniques were strongly correlated (phantom IR-based scan: r = 0.99, SD = 5.12, P < 0.0001; N = 5**,** Fig. 5.6a;

SR-based scan: r = 0.99, SD = 29.21, P < 0.0001; N = 5, n = 11**,** Fig. 5.6b; volunteer IR-based scan: r = 0.99, SD = 34.68, P < 0.0001, n = 11**,** Fig. 5.7a; SR-based scan: r = 0.97, SD = 60.76, P < 0.0001, n = 11**,** Fig. 5.7b), likewise for the mean T_2* values (phantom IR-based scan: r = 0.99, SD = 8.04, P < 0.0001; N = 5**,** Fig. 5.6c; SR-based scan: r = 0.99; SD = 12.06, P < 0.0001; N = 5**,** Fig. 5.6d; volunteer IR-based scan: r = 0.99, SD = 1.64, P < 0.0001, n = 11**,** Fig. 5.7c; SR-based scan: r = 0.97, SD = 2.15, P < 0.0001, n = 11**,** Figure 5.7d).

The results of the interstudy variability of the IR- and SR-based sequences are summarized in Figure 5.8. Bland-Altman analysis indicated that there was no significant deviation in the T_1 and T_2* values obtained between studies using the IR- and SR-based approaches. The mean difference in the T_1 value using the IR-based sequence was -0.2% with 95% confidence interval -5.2% to 4.8% (Fig. 5.8a). The mean difference in T_2* using IR-based sequence was 0.4% with 95% confidence interval -9.6% to 10.4% (Fig. 5.8c). Likewise for the SR-based sequence, the mean difference in the T_1 value was 0.1% with 95% confidence interval -8.2% to 8.3% (Fig. 5.8b) and the mean difference in the T_2* value was 0.1% with 95% confidence interval -9.7% to 9.9% (Fig. 5.8d).

Each tissue (muscle or renal cortex) showed stable relaxation values during dynamic acquisition with typical variations < 6% (Fig. 5.9). During IR-based scan, e.g., for the volunteer shown in Figure 5.9, the relaxation time values were muscle T_1 = 1056 ± 17 ms, T_2* = 24.1 ± 1.0 ms, renal cortex T_1 = 1381 ± 27 ms, T_2* = 58.6 ± 3.6 ms. Also for the SR-based scan, the values were muscle T_1 = 992 ± 37 ms, T_2* = 24.1 ± 1.0 ms, renal cortex T_1 = 1407 ± 58 ms, T_2* = 55.2 ± 3.4 ms. IR- and SR-based scans produced similar T_2* variations (muscle: ~ 4%; renal cortex: ~6%) during dynamic scans. For T_1 estimation, the IR-based

scan showed smaller variations (muscle: ~ 1.6%, renal cortex: ~ 2%) than that of SR-based scan (muscle: ~ 3.7%, renal cortex: ~ 4.2%).

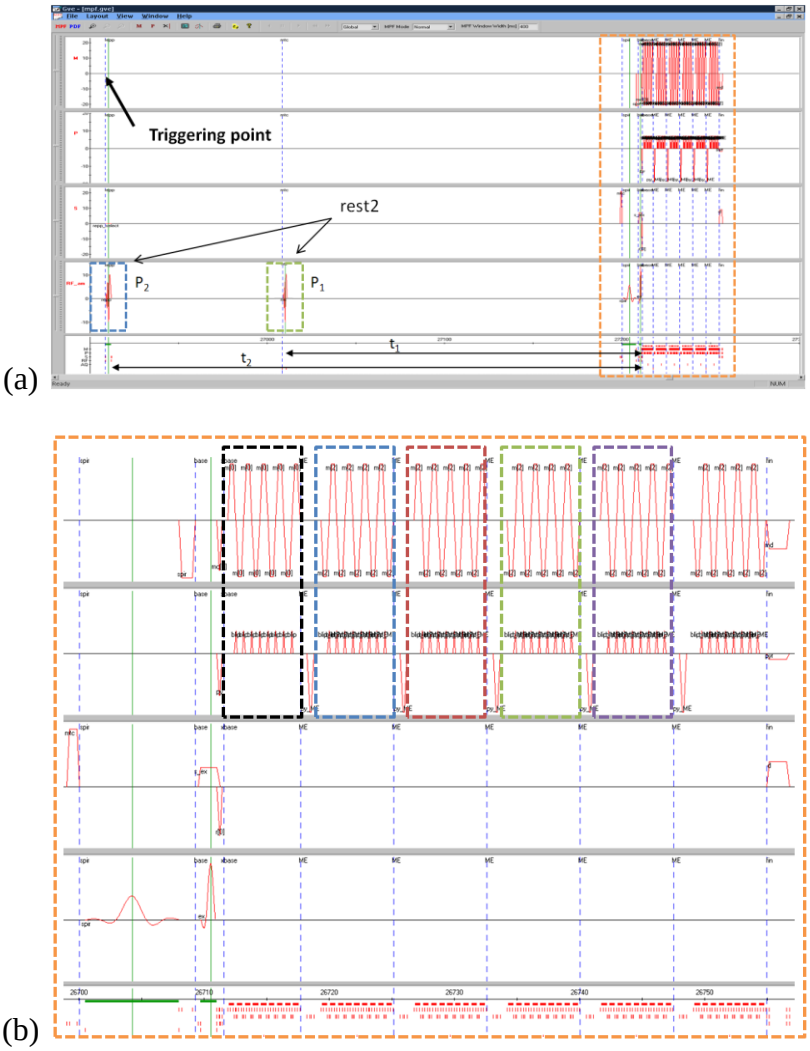

Figure 5.2 Pulse sequence diagram of the SR-based sequence. (a) Multiple saturation recovery time t1 and t_2 generate P_1 and P_2 points on the saturation recovery curve for estimation of T_1. (b) Multiple echo times generate 5 different samples on the T_2* relaxation curve for estimation of T_2*.

(a)

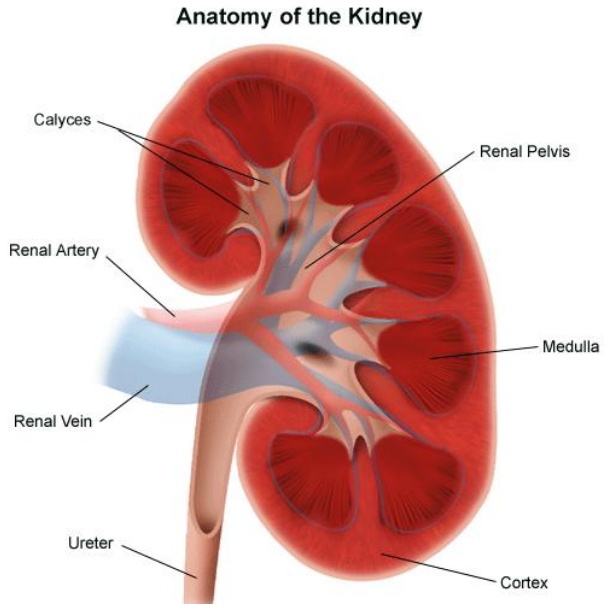

(b)

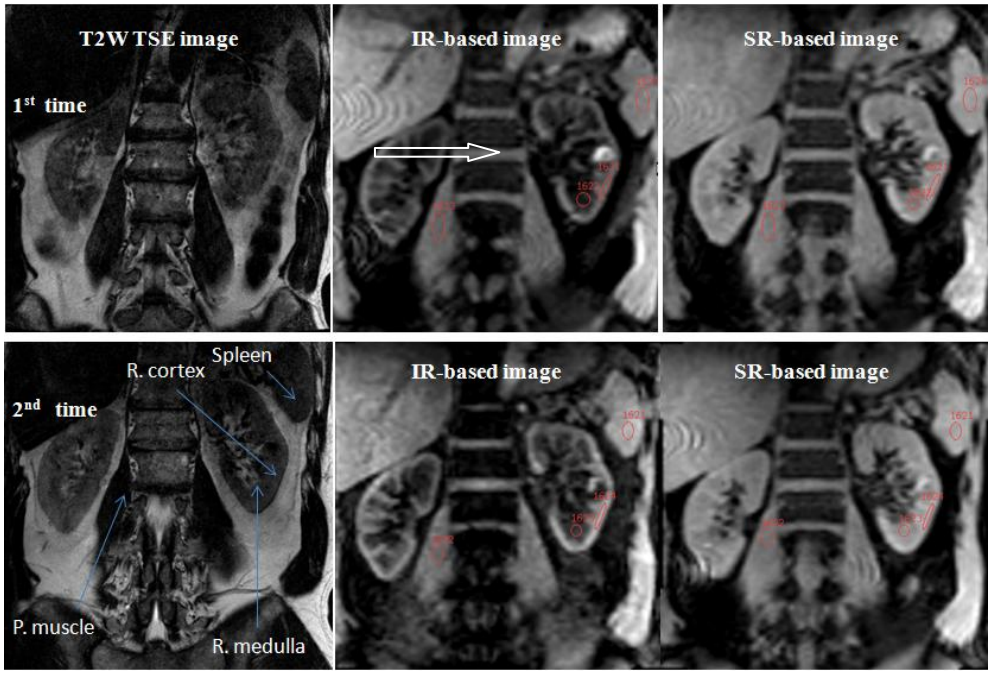

Figure 5.3 Example region of interest placement in human abdominal organs for T_1 and T_2* relaxation times quantification. (a) Anatomy of human kidney (http://www.childrenshospital.org/az/Site1318/mainpageS1318P0.html), (b) IR-based and SR-based images with ROIs in muscle, spleen, renal cortex, and renal medulla. Arrow points at region suspicious for renal cancer (reported to radiologists).

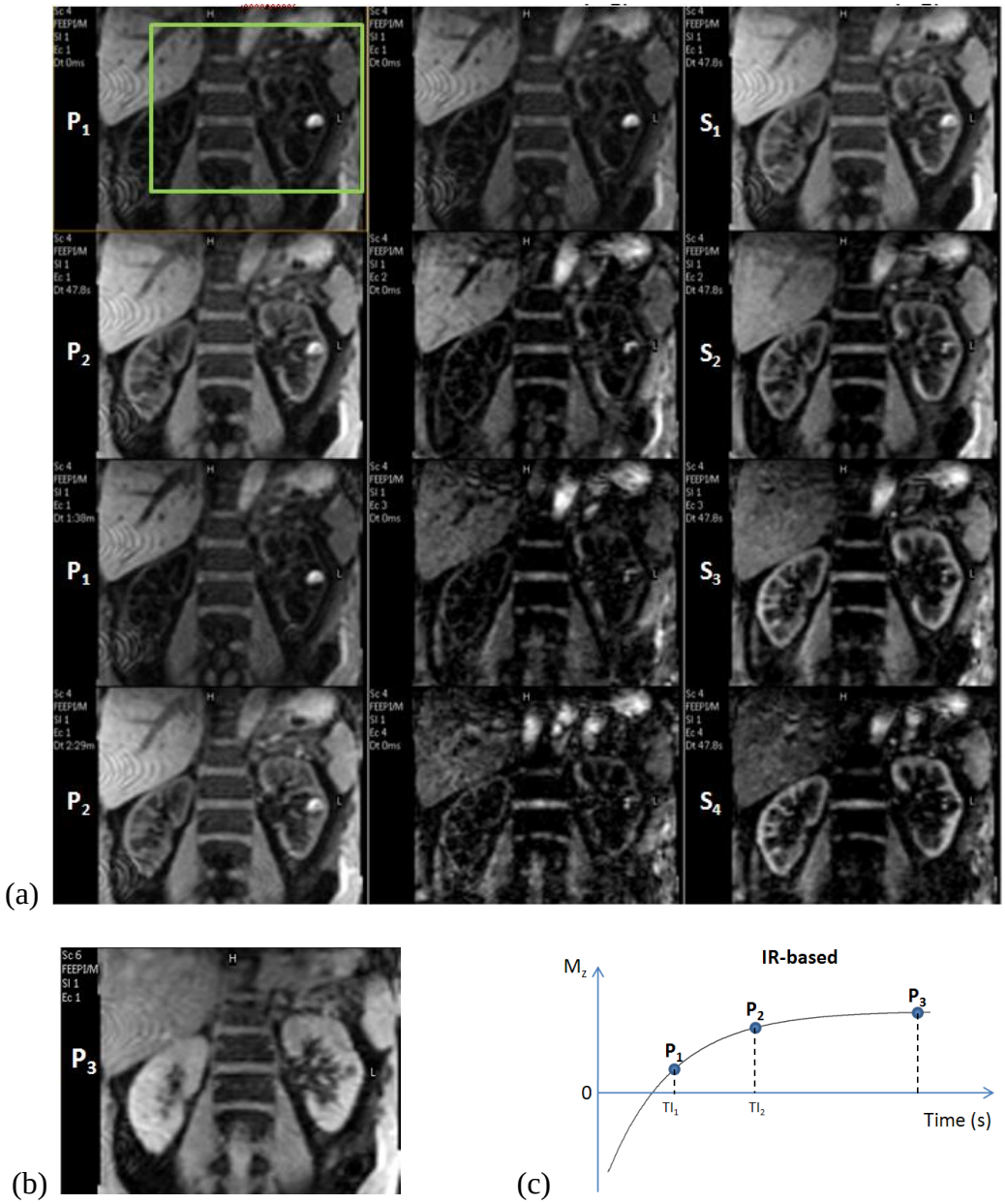

Figure 5.4 IR-based images and fully recovery image for relaxation time quantification. (a) T_1-weighted images with different TIs (left column) and T_2*-weighted images with different TEs (middle and right columns); (b) a fully recovery T_1-weighted image; (c) Three points (P_1, P_2, and P_3) on the inversion recovery curve for T_1 quantification.

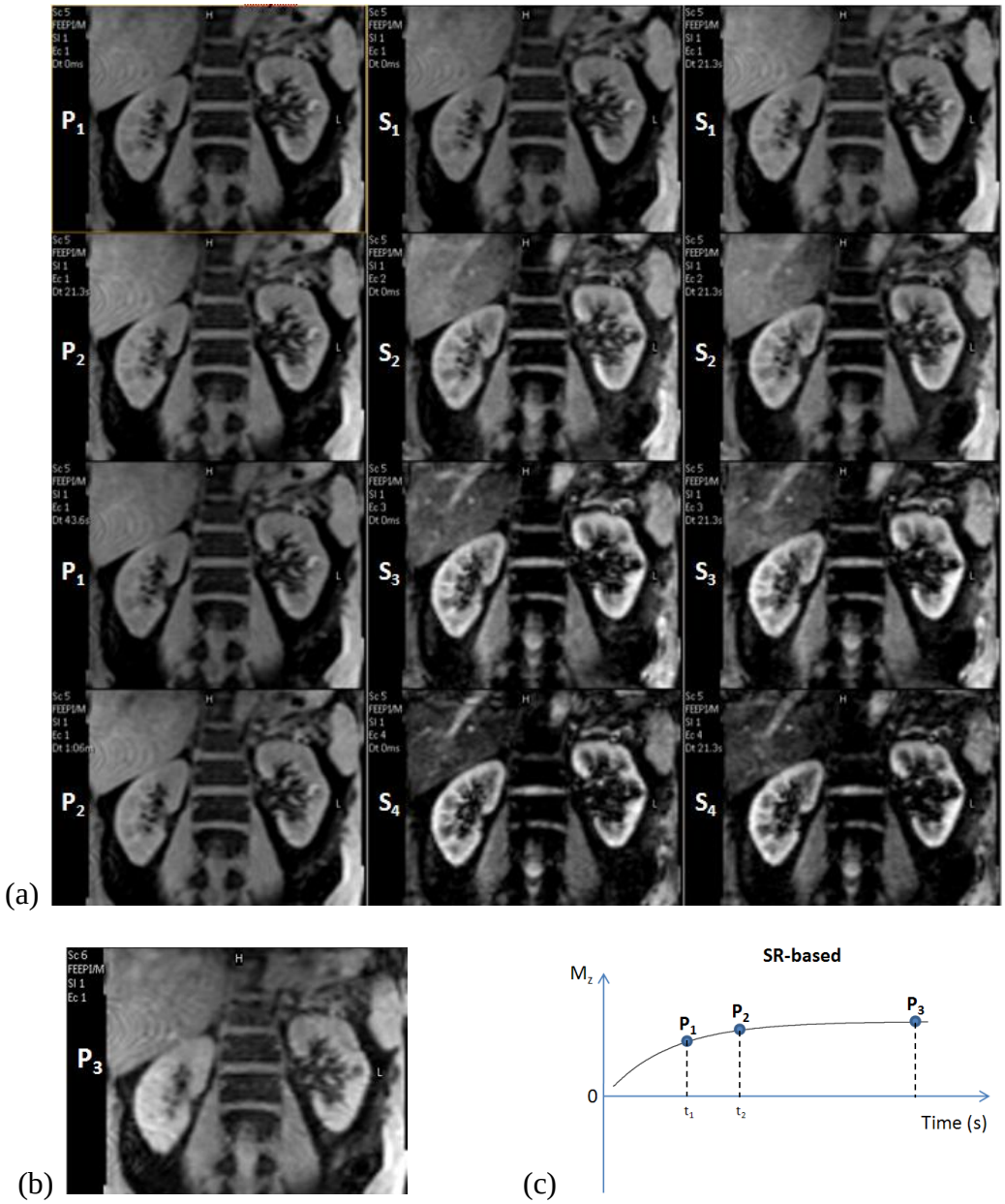

Figure 5.5 SR-based images and fully recovery image for relaxation time quantification. (a) T_1-weighted images with different delay times (left column) and T_2*-weighted images with different TEs (middle and right columns); (b) a fully recovery T_1-weighted image; (c) Three points (P_1, P_2, and P_3) on the saturation recovery curve for T_1 quantification.

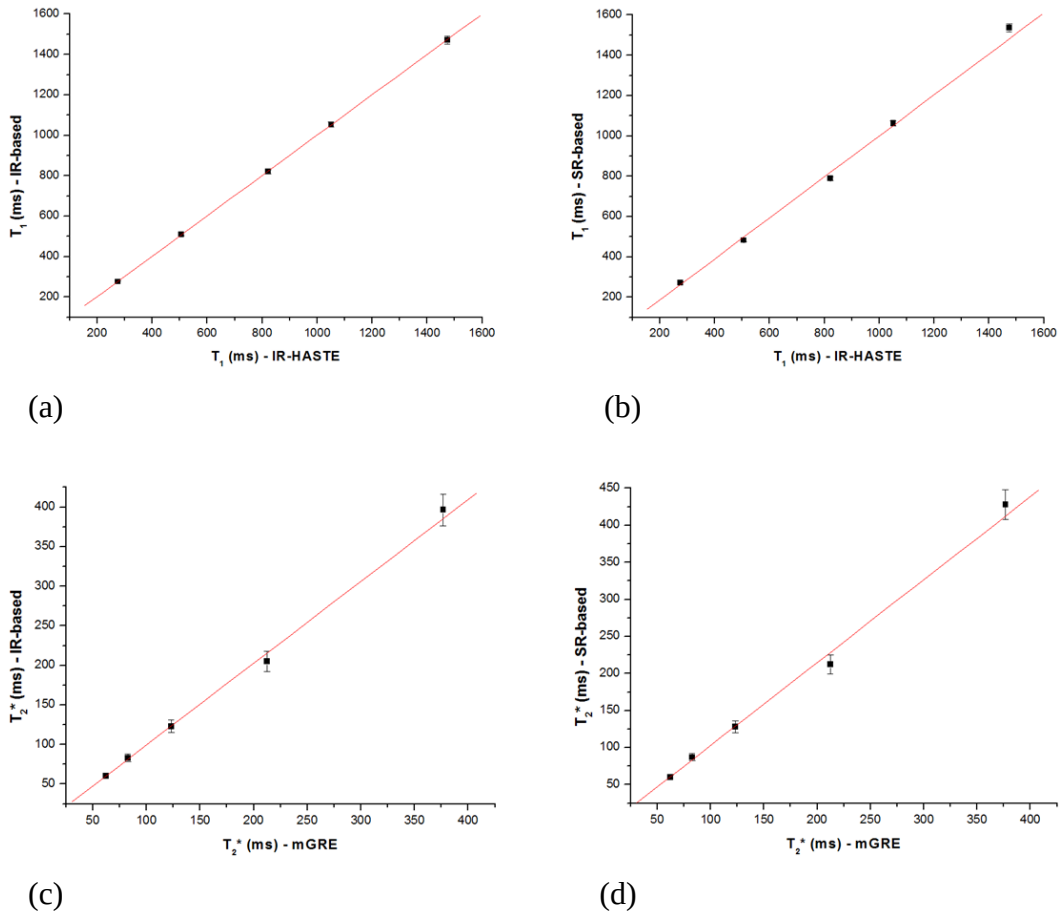

Figure 5.6 Comparison of relaxation times measured using new combined or traditional sequences on phantoms. (a) T_1 (IR-HASTE ($T_{1,\,IR}$) vs. IR-based ($T_{1,\,NEW}$)): r = 0.99, SD = 5.12, P < 0.0001; N = 5 and (b) T_1 (IR-HASTE ($T_{1,\,IR}$) vs. SR-based ($T_{1,\,NEW}$)): r = 0.99, SD = 29.21, P < 0.0001; N = 5 and (c) T_2* (IR-HASTE (T_2*$_{,\,GRE}$) vs. IR-based (T_2*$_{,\,NEW}$)): r = 0.99, SD = 8.04, P < 0.0001; N = 5 and (d) T_2* (mGRE (T_2*$_{,\,GRE}$) vs. SR-based (T_2*$_{,\,NEW}$)): r = 0.99; SD = 12.06, P < 0.0001; N = 5. The red lines indicate the line of identity. N is the number of ROIs from 5 phantoms.

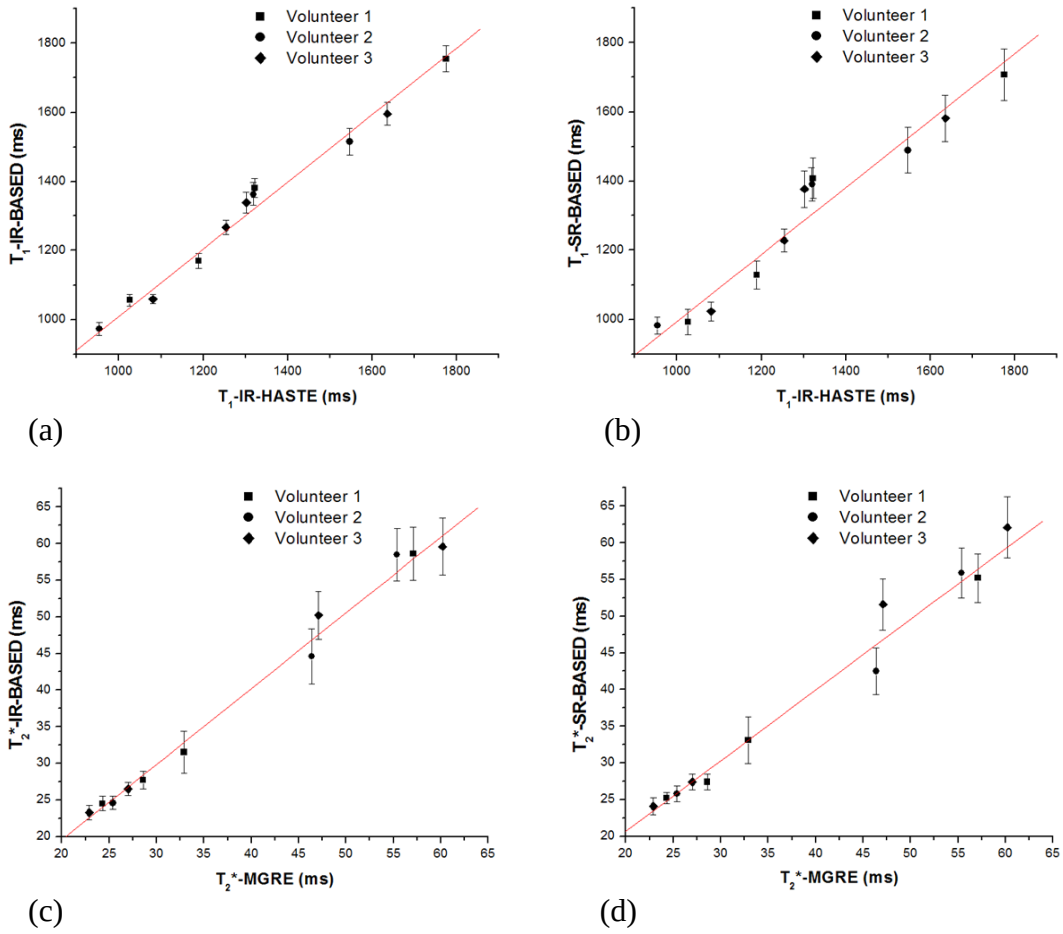

Figure 5.7 Comparison of relaxation times measured using new combined or traditional sequences on volunteers. (a) T_1 (IR-HASTE ($T_{1,\,IR}$) vs. IR-based ($T_{1,\,NEW}$)): r = 0.99, SD = 34.68, P < 0.0001; N = 11 and (b) T_1 (IR-HASTE ($T_{1,\,IR}$) vs. SR-based ($T_{1,\,NEW}$)): r = 0.97, SD = 60.76, P < 0.0001; N = 11 and (c) T_2* (IR-HASTE ($T_2^{*}{}_{,\,GRE}$) vs. IR-based ($T_2^{*}{}_{,\,NEW}$)): r = 0.99, SD = 1.64, P < 0.0001; N = 11 and (d) T_2* (mGRE ($T_2^{*}{}_{,\,GRE}$) vs. SR-based ($T_2^{*}{}_{,\,NEW}$)): r = 0.99; SD = 2.15, P < 0.0001; N = 11. The red lines indicate the line of identity. Human data were obtained during air breathing. N is the total number of measured organs obtained from three volunteers.

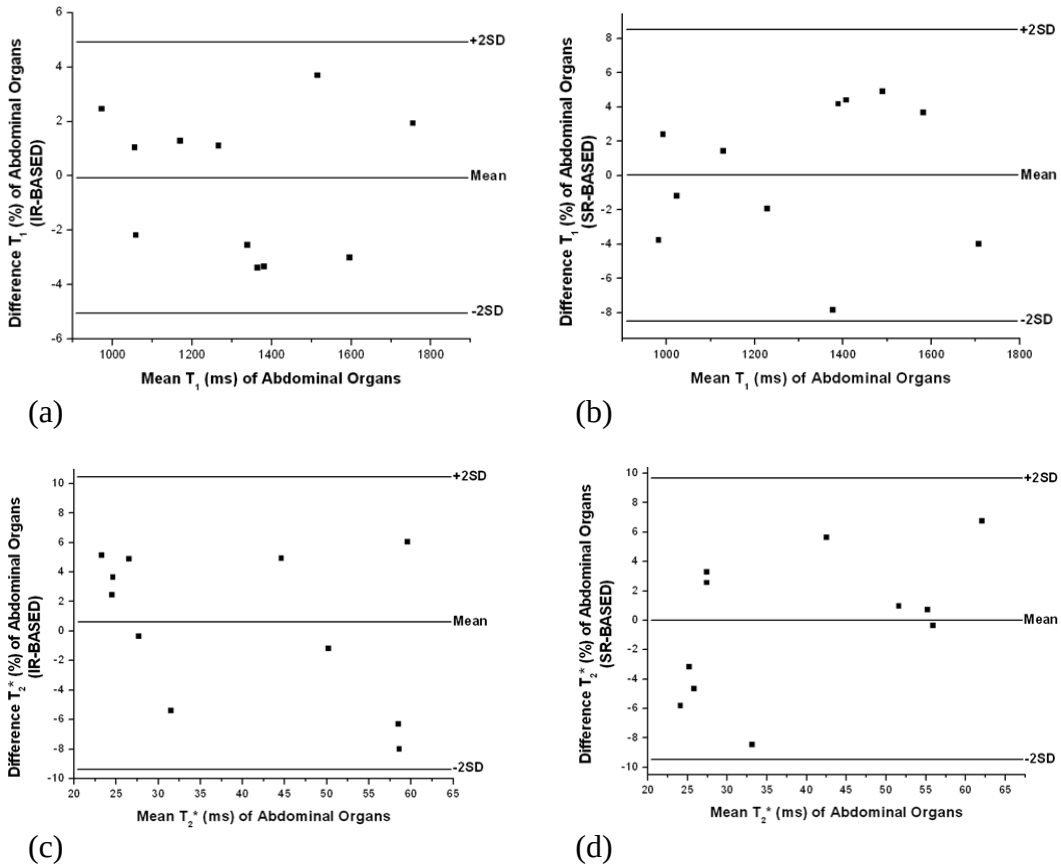

Figure 5.8 Comparison of T_1 and T_2* measurements using Bland-Altman analysis. Human volunteers: Bland-Altman plots of reproducibility of new sequences: results of muscle, spleen, renal cortex, and renal medulla on successive occasion; T_1 relaxation time measurements using (a) IR-based sequence and (b) SR-based sequence; and T_2* relaxation time measurements using (c) IR-based sequence and (d) SR-based sequence.

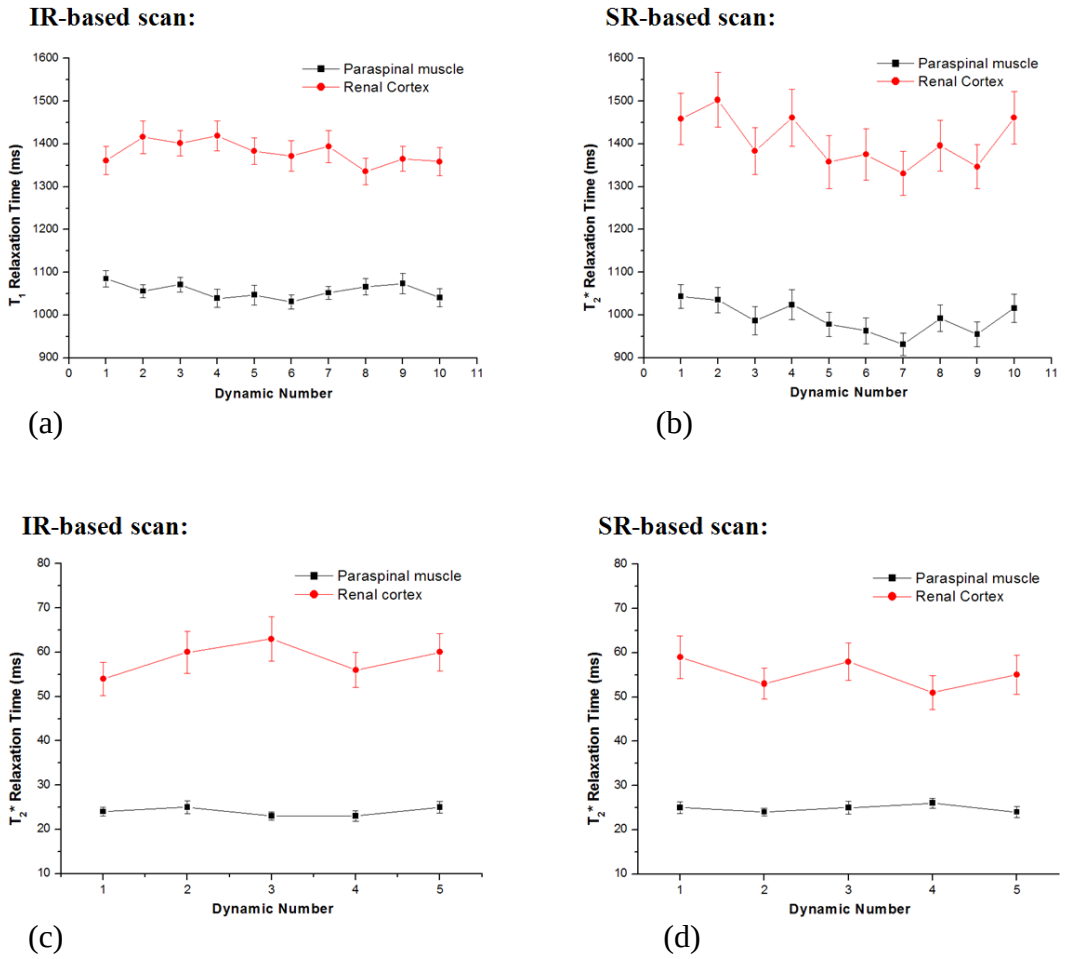

Figure 5.9 Plots of dynamic relaxation time variations in muscle and renal cortex (subject 1). (a) IR-based T_1 dynamic changes, (b) SR-based T_1 dynamic changes, and (c) IR-based T_2* dynamic changes, (d) SR-based T_2* dynamic changes.

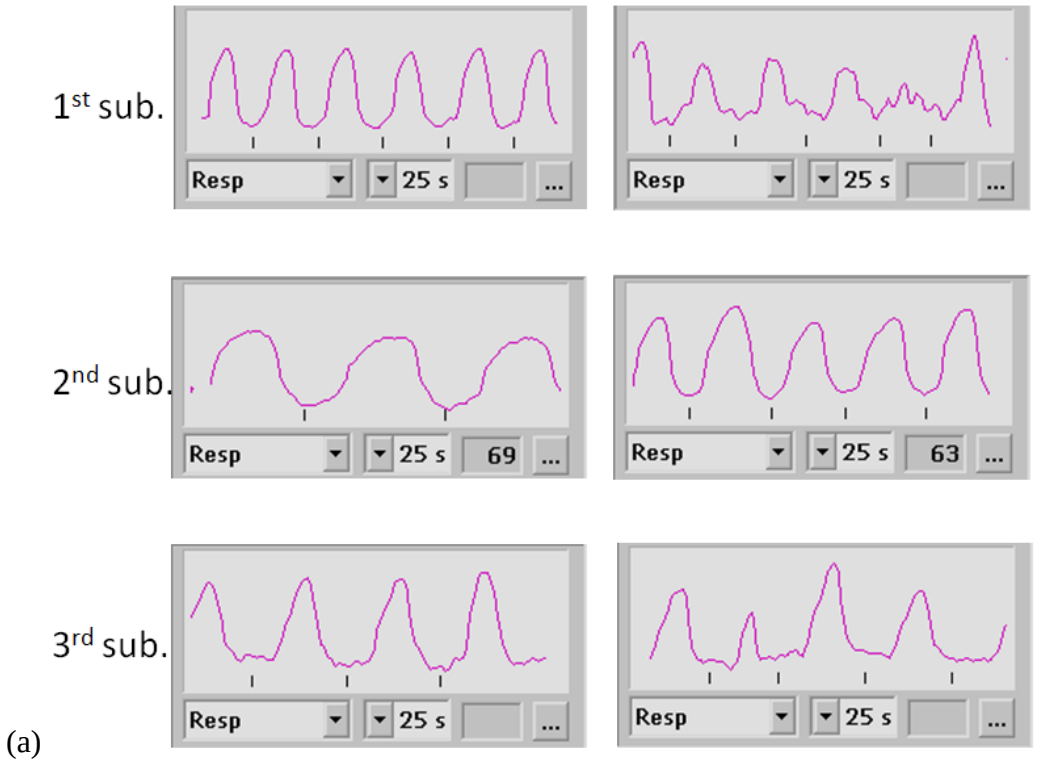

Figure 5.10 Variability of respiration during volunteer experiments. (a) regular respiration (left column) and irregular respiration (right column); (b) both exhalation level and respiratory cycle length may vary during respiratory triggering scans.

(a)

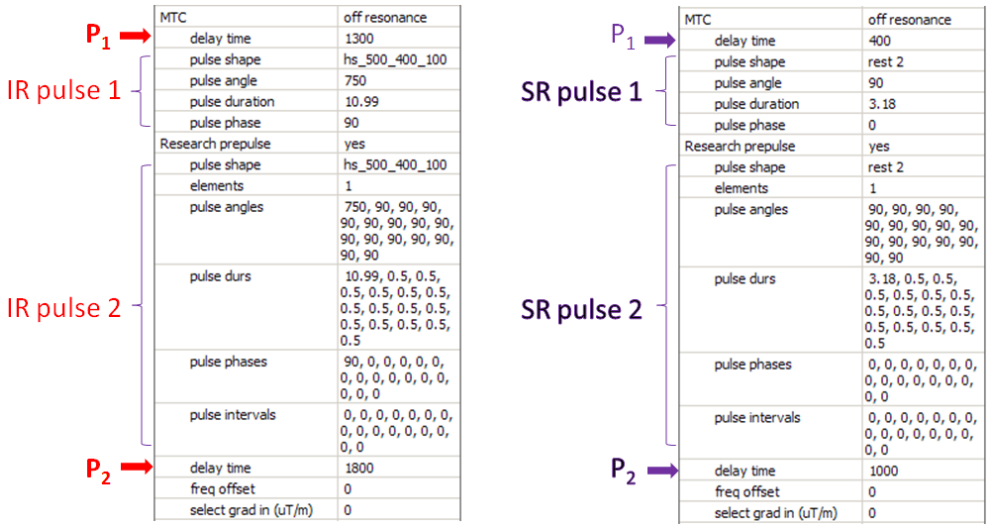

MTC	off resonance
delay time	1300
pulse shape	hs_500_400_100
pulse angle	750
pulse duration	10.99
pulse phase	90
Research prepulse	yes
pulse shape	hs_500_400_100
elements	1
pulse angles	750, 90, 90, 90, 90, 90, 90, 90, 90, 90, 90, 90, 90, 90, 90
pulse durs	10.99, 0.5, 0.5, 0.5, 0.5, 0.5, 0.5, 0.5, 0.5, 0.5, 0.5, 0.5, 0.5, 0.5, 0.5
pulse phases	90, 0, 0, 0, 0, 0, 0, 0, 0, 0, 0, 0, 0, 0, 0
pulse intervals	0, 0, 0, 0, 0, 0, 0, 0, 0, 0, 0, 0, 0, 0, 0
delay time	1800
freq offset	0
select grad in (uT/m)	0

MTC	off resonance
delay time	400
pulse shape	rest 2
pulse angle	90
pulse duration	3.18
pulse phase	0
Research prepulse	yes
pulse shape	rest 2
elements	1
pulse angles	90, 90, 90, 90, 90, 90, 90, 90, 90, 90, 90, 90, 90, 90, 90
pulse durs	3.18, 0.5, 0.5, 0.5, 0.5, 0.5, 0.5, 0.5, 0.5, 0.5, 0.5, 0.5, 0.5, 0.5, 0.5
pulse phases	0, 0, 0, 0, 0, 0, 0, 0, 0, 0, 0, 0, 0, 0, 0
pulse intervals	0, 0, 0, 0, 0, 0, 0, 0, 0, 0, 0, 0, 0, 0, 0
delay time	1000
freq offset	0
select grad in (uT/m)	0

(b)

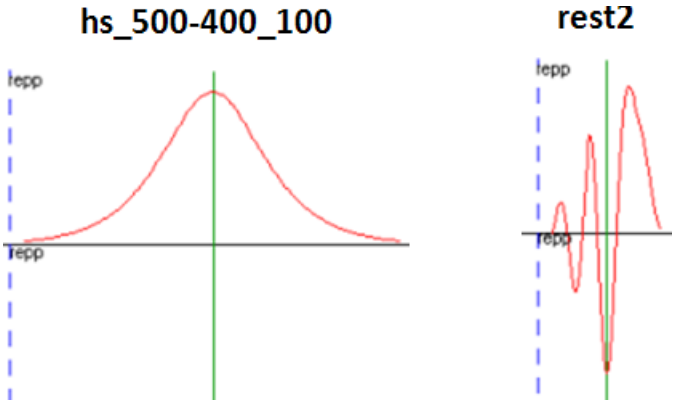

Figure 5.11 Parameter setting on Philips MR user interface. (a) IR-based sequence parameter setting (left column) and SR-based sequence parameter setting; (b) pre-pulse selected for IR-based sequence (left) and SR-based sequence (right).

5.4 Discussion

This chapter demonstrates the feasibility of two "upgraded" interleaved T_1 and T_2* mapping techniques, allowing the simultaneous measurements of the relaxation times of human abdominal tissues in a single dynamic scan. The SR-based sequence is suitable for higher temporal resolution measurements of relaxation times and IR-based scan can provide more stable values of T_1 and T_2* in a dynamic scan. The relaxation times measured by IR- and SR-based methods were consistent with those obtained using traditional pulse sequences.

The accuracy of T_1 quantification depends on the number of the sampling points (TI and τ_i) distributed over the relaxation curve. To ensure adequate temporal resolution, the 2-point sampling is applied for both IR- and SR-based scans. Furthermore, an additional scan without IR/SR prepulse was performed to determine fully recovered longitudinal magnetization and achieve 3-parameter fitting.

The multi-shot EPI technique allows flexible tradeoff between imaging time and susceptibility effects such as geometric distortion, ghosting. Longer echo train length leads to decreased imaging time and results in improvement in temporal resolution of T_1 measurements, but causes more severe artifacts from susceptibility. The increased echo trains may also result in underestimation of T_2*. Therefore, in volunteer experiments, a short ETL of 9 instead of 15 in the previous experiment (chapter 4) was selected to improve the image quality and accuracy of T_2* at the cost of temporal resolution in an acceptable range (SR-based ~ 20 s; IR-based ~ 40 s). With this setting, good image quality, accurate relaxation

time estimation and adequate temporal resolution can be achieved using IR- and SR-based sequences.

As shown in Figure 5.9, stable estimation of T_1 and T_2* can be seen in muscle and renal cortex during a dynamic IR-based scan. However, moderate variation occurred for T_1 estimation using a dynamic SR-based sequence. This might be due to the use of an imperfect saturation prepulse, called "rest2". Unlike inversion prepulse, an adiabatic pulse called "hs_500-400_100", the "rest2" saturation prepulse is a non-adiabatic pulse and may not meet the assumption of perfect flip angles for several reasons: (1) The flip angles could be calibrated incorrectly; (2) off-resonance effects may cause problems; (3) the RF (B1) field may be inhomogeneous, especially in a large FOV; (4) asymmetric pulse may yield some extra deviations between time intervals (Fig. 5.11b). Therefore a small residual magnetization would be left after SR pulse which may lead to errors of ~ 5% or more in estimation of T_1. In such cases the accuracy of T_1 measurements would be sensitive to pulse imperfections. Other options for better saturation, such as an adiabatic pulse, or/and composite pulses, should be validated in future work.

Moreover, Figure 5.11 showed smaller variations of muscle relaxation times compared with those of renal cortex. These measured variation differences may reflect inconsistent respiration during the dynamic scan. During irregular respiration scans, the influence of variability of respiration cycle length (TR) can be negligible with optimum setting. However, fluctuation in exhalation levels may cause slight mis-registration which may yield larger variation in renal cortex relaxation time estimation (Fig. 5.11). It is not easy to correct these

errors in image post-processing. Therefore, the volunteers were advised to breathe gently and freely throughout the entire dynamic series to try to mitigate this issue.

5.5 Summary

In conclusion, this work demonstrates the feasibility of two "upgraded" T_1 and T_2* mapping techniques, allowing the simultaneous quantification of relaxation times in human abdominal organs. The SR-based method provides improved temporal resolution for T_1 and T_2* measurements in short respiratory cycle cases (< 6 s) and the IR-based method provides more accurate and stable estimation of relaxation times with an adequate though lower temporal resolution. When in long respiratory cycle cases (> 6 s), the SR-based method and IR-based method will provide the same temporal resolution, therefore the IR-based method will be more preferable. My measurements using these new methods were consistent with those of conventional methods. Such measurements could have important application to assessing hypoxia and response to interventions with respect to treatment planning in radiation oncology.

CHAPTER SIX

SUMMARY AND FUTURE WORK

6.1 Summary

Tumor oxygenation is increasingly recognized as an important factor to enhance the efficacy of chemo- and radio-therapy**.** MRI is becoming a widely accepted diagnostic imaging modality for investigation of tumor oxygenation. Research to improve the effectiveness of MR techniques for detection of oxygenation biomarkers (T_1 and T_2*) in the tissue/tumor hypoxia studies mainly includes efforts to improve sensitivity, efficiency and accuracy of measurements (enhanced contrast change, reduced artifacts and distortion) and to minimize scan duration (high temporal resolution). The work in this dissertation mainly concentrates on novel combined multi-parametric techniques to obtain both BOLD and TOLD images.

Two major technical innovations described in this dissertation are: (a) an accurate IR-based T_1 and T_2* weighting/mapping method; (b) a rapid SR-based T_1 and T_2* mapping strategy. All these methods or concepts have been validated by phantom and human experiments. These contributions are summarized here:

- An absolute quantification ^{1}H MRS method for determination of tCho concentrations in cervical tumors is employed. The assessment of tumor oxygenation is also investigated in cervical cancer studies.

- A novel approach (ms-mGEPI-$T_{1,2*}$) is developed to simultaneously measure both T_1- and T_2*-weighted signal changes, as well as and T_1- and T_2*-maps serially during a single dynamic MRI scan. This method has also been validated in both phantom and human abdominal tissue experiments and both *in vitro* and *in vivo* results are in good agreement with those obtained using conventional methods and the literature. The ms-mGEPI-$T_{1,2*}$ has been found to provide sensitive BOLD and TOLD responses under an oxygen challenge.
- Two enhanced version of the ms-mGEPI-$T_{1,2*}$ technique with higher temporal resolution (SR-based sequence) or more accurate relaxation time estimation (IR-based sequence) are developed and validated in phantom and 3 volunteer studies. Relaxation times measured by these novel methods were in good agreement with those obtained using conventional pulse sequences. A pulse sequence which combines all three methods was developed for use on Philips MR user interface and has great potential in clinical MR examinations.

6.2 Future Directions

Although all the new methods have been validated in this dissertation, there is still room for further technical improvements, and for wider clinical and research applications. The possible future directions are summarized in the following sections.

6.2.1 ^{1}H MRS for Cervical Cancer Investigation

- Test the feasibility of using high sensitivity coils, such as endovaginal coil, for cervical tumor MRS studies. tCho concentrations can be measured accurately in a big voxel using the SENSE cardiac surface coil at 3 T. However, for small tumor cases, a higher sensitivity coil is essential to detect adequate signal from small voxels.
- Apply 3D chemical shift imaging technique for cervical tumor studies to minimize VOI placement errors and allow better definition of proliferating areas of tumors for radiotherapy. 3D MRS results can also be correlated with MR imaging results, such as DCE and BOLD/TOLD, spatially, voxel-by-voxel.
- Improve the current protocol to determine the presence or absence of $-CH_2$ biomarker and the response to therapy.
- Develop a lactate-edited MR spectroscopy technique for the quantification of lactate level. Determining the concentration of Lac in cervical tumors will be more challenging than other metabolites, such as tCho, due to spectral contamination from overlapped lipid.
- Collect more samples to validate the feasibility of determining the threshold (an optimal cutoff) for separating the residual/normal tissues or malignant lesions variability.

6.2.2 Simultaneous measurement of BOLD/TOLD

- Improve the accuracy of current SR-based quantification by replacing the imperfect SR prepulse by an adiabatic pulse or/and composite pulses without reducing imaging speed or sacrificing image quality. Specifically, B0 and B1

profiles (maps) will be measured in phantoms using different pre-pulse parameters, and then the measured B0 and B1 inhomogeneities guide the pulse design to produce optimal saturation effectiveness over the ROIs. Simulations and *in vivo* experiments will be used to evaluate the proposed saturation pulse and compare it with other current approaches.

- Validate the simulation of variations of T_1 calculations due to large respiratory rate variability on phantom experiments.
- Test the feasibility for oxygen-sensitive imaging in human abdomen under a hyperoxic gas (oxygen or carbogen) challenge. Changes in blood flow due to vasoconstriction or vasodilatation may produce different BOLD and TOLD effects in abdominal tissues.
- Develop a modified TE-shifted SR-based sequence to yield more short TE images to ensure the accuracy of short T2* (< 10 ms) tissues, e.g. lung tumors, quantification.
- Test the feasibility of using the proposed multi-parametric oxygen-sensitive sequences for tumor oxygenation studies.

APPENDIX A

ITERATIVE T_1 ESTIMATION

The relationship between the ratio of signal intensity and T_1 at a fixed TE_1 can be expressed as:

$$\text{Ratio} = \frac{S_{IR}(TE_1)}{S_{non\ -IR}(TE_1)} = \frac{1-2\cdot e^{-\frac{TI}{T_1}}+e^{-\frac{TR}{T_1}}}{1-e^{-\frac{TR}{T_1}}} \qquad [1]$$

where the TI and TR are known, allowing estimation of the only unknown, T_1, on a voxel-by-voxel basis for each time point. Figure 7.1 shows the ratio $S_{IR}/S_{non\text{-}IR}$ plotted for T_1 in the range of 1 s - 2 s for the parameters used in the current study. While each ratio will correspond to a single T_1 value, it is not possible to analytically solve for T_1 as a function of the signal intensity ratio. However, for a known ratio, the corresponding, unique T_1 can be obtained with the use of an iterative approach. In the current study, an initial estimate of T_1 can be estimated by ignoring the effects of non-equilibrium relaxation:

$$T_{1,est} = \frac{-TI}{\ln(0.5-(\frac{S_{IR}}{2S_{non\ -IR}}))} \qquad [2]$$

Next, the T_1 estimate is increased by a small factor (δ = 1 ms), and the ratio based on Eq. [1] is recalculated and compared with the observed ratio. Repeat this process until difference between the observed and calculated ratios is less than a given tolerance ($\varepsilon < 0.001$). The T_1 corresponding to this ratio is then assigned to the given voxel. This process can be repeated for each voxel to produce T_1 map. The propagation of noise in T_1 can be analyzed below.

Suppose two measured corresponding voxel signal intensities S_{IR} and $S_{non\text{-}IR}$ have noise, n_{IR} and $n_{non\text{-}IR}$ (usually $n_{IR} << S_{IR}$ and $n_{non\text{-}IR} << S_{non\text{-}IR}$). A new voxel SI, Ratio, is calculated from S_{IR} and $S_{non\text{-}IR}$. The uncertainty of Ratio, n_{ratio}, can be estimated by using standard deviations with the equation below:

$$n_{ratio} = |Ratio| \cdot \sqrt{\left(\frac{n_{IR}}{S_{IR}}\right)^2 + \left(\frac{n_{non\ -IR}}{S_{non\ -IR}}\right)^2} \qquad [3]$$

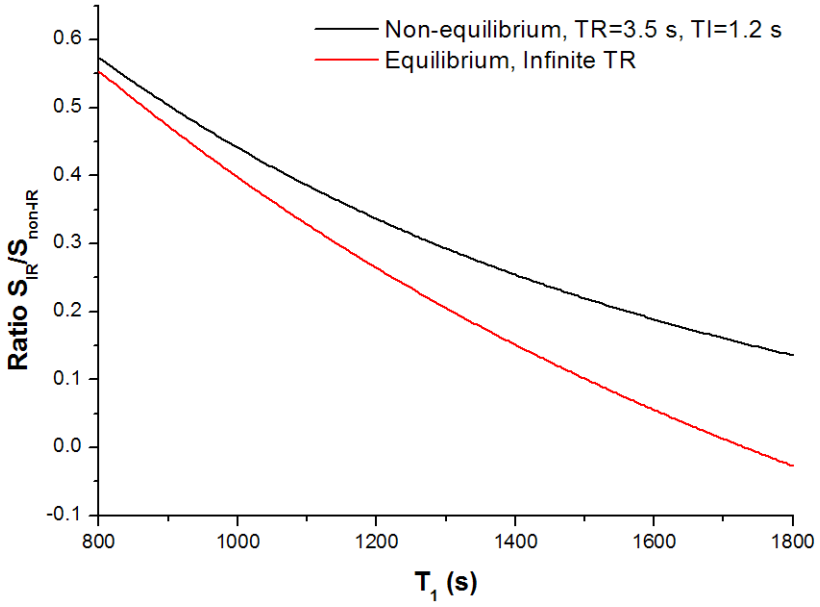

Figure 7.1 Comparison of the signal ratio ($S_{IR}/S_{non\text{-}IR}$ images) vs. T_1 under conditions of equilibrium magnetization (infinite TR, red line), and under the nonequilibrium conditions (e.g. TR=3.5 s, TI=1.2 s; black line). For any measured ratio, there is a unique T_1 value that may be obtained using an iterative method as described in the Appendix A.

APPENDIX B

MODIFICATION IN SOURCE CODE

(Yellow Highlighted lines indicate changes made by Yao)

```
/*==========================================================================
=====*/
/*                                                                        */
/*       INCLUDE_FILE:      MPUMTCRCD.H                                   */
/*       PACKAGE:    IMTC                                               */
/*       COMPONENT:         METHPDF                                       */
/*       SOFTWARE LAYER: 1320                                             */
/*                                                                        */
/*       Copyright 1995: Philips Electronics N.V..                        */
/*==========================================================================
=====*/

#ifndef MPUMTCRCD_H
#define MPUMTCRCD_H

/*==========================================================================
=====*/
/*       I N C L U D E S                                                  */
/*==========================================================================
=====*/
#include "mrmethods/igoalobj/mggrcd.h"                  /*< GOAL_MODULE >*/
#include "METHPDF/inc/mpurcd.h"                 /*< GOAL_MODULE >*/
#include "METHGLO/inc/mgobjrfvarrcd.h"          /*< GOAL_MODULE >*/    //Yao Ding
/*==========================================================================
=====*/
/*       S Y M B O L   D E F I N I T I O N S                              */
/*==========================================================================
=====*/
/*<      GOAL_ENUM NAME_TAG: "XEIMTC01"                                   >*/
typedef enum
{
MPUMTC_SHAPE_MIN = -1,
MPUMTC_SHAPE_COMP,
```

```
MPUMTC_SHAPE_OFF_RES,
MPUMTC_SHAPE_1,
MPUMTC_SHAPE_2,
MPUMTC_SHAPE_3,
MPUMTC_SHAPE_MAX
}
MPUMTC_SHAPE_ENUM;
/*==========================================================================*/
/*      IEX_MTC       I N T E R F A C E   D E F I N I T I O N            */
/*==========================================================================*/
/*[     GOAL_PAR_FORM_DEFGROUP  MPIMTC_EX                                  ]*/

/*<    PARAMETER MPU_MTC_MODE_ENUM EX_MTC_enable                          >*/
/*<    {                                                          >*/
/*<      DEFAULT_VALUE:      MPU_MTC_MODE_NO;                     >*/
/*<      NAME_TAG:           "XNIMTC001";                         >*/
/*<      HELP_TAG:           "XHIMTC001";                         >*/
/*<    }                                                          >*/

/*<    PARAMETER MGG_YESNO_ENUM EX_MTC_sos                                >*/
/*<    {                                                          >*/
/*<      DEFAULT_VALUE:      NO;                                  >*/
/*<      NAME_TAG:           "XNIMTC002";                         >*/
/*<      HELP_TAG:           "XHIMTC002";                         >*/
/*<    }                                                          >*/

/*<    PARAMETER MGG_YESNO_ENUM EX_MTC_IR_base_enable
       >*/
/*<    {                                                          >*/
/*<      DEFAULT_VALUE:      NO;                                  >*/
/*<      NAME_TAG:           "XNIMTC003";                         >*/
/*<      HELP_TAG:           "XHIMTC003";                         >*/
/*<    }                                                          >*/

/*<    PARAMETER int EX_MTC_off_res_mp_nr_reps                      >*/
/*<    {                                                          >*/
/*<      RANGE:              1 - 100;                             >*/
/*<      DEFAULT_VALUE:      8;                                   >*/
/*<      ADJUST_VALUE: 1;                                         >*/
/*<      NAME_TAG:           "XNIMTC004";                         >*/
/*<      HELP_TAG:           "XHIMTC004";                         >*/
```

```
/*<      }                                                                  >*/

/*<      PARAMETER int EX_MTC_off_res_mp_angle                                 >*/
/*<      {                                                                  >*/
/*<        RANGE:              1 - 1200;                                    >*/
/*<        DEFAULT_VALUE:      800;                                            >*/
/*<        ADJUST_VALUE: 50;                                                >*/
/*<        NAME_TAG:           "XNIMTC005";                                       >*/
/*<        HELP_TAG:           "XHIMTC005";                                       >*/
/*<      }                                                                  >*/

/*<      PARAMETER int EX_MTC_off_res_mp_dur                                   >*/
/*<      {                                                                  >*/
/*<        RANGE:              1 - 100;                                     >*/
/*<        DEFAULT_VALUE:      20;                                             >*/
/*<        ADJUST_VALUE: 1;                                                 >*/
/*<        NAME_TAG:           "XNIMTC006";                                       >*/
/*<        HELP_TAG:           "XHIMTC006";                                       >*/
/*<      }                                                                  >*/

/*<      PARAMETER int EX_MTC_off_res_mp_freq                                  >*/
/*<      {                                                                  >*/
/*<        RANGE:              1 - 1000;                                    >*/
/*<        DEFAULT_VALUE:      500;                                            >*/
/*<        ADJUST_VALUE: 1;                                                 >*/
/*<        NAME_TAG:           "XNIMTC007";                                       >*/
/*<        HELP_TAG:           "XHIMTC007";                                       >*/
/*<      }                                                                  >*/

/*<      PARAMETER float EX_MTC_delay_time                                     >*/
//yao ding start
/*<      {                                                                  >*/
/*<        RANGE:              0.0 - 10000.0;                               >*/
/*<        DEFAULT_VALUE:      100.;                                           >*/
/*<        ADJUST_VALUE: 10.0;                                              >*/
/*<        NAME_TAG:           "XNIMTC008";                                       >*/
/*<        HELP_TAG:           "XHIMTC008";                                       >*/
/*<      }                                                                  >*/

/*<      PARAMETER MAOBJ_RFSHAPE_ENUM EX_MTC_pulse_shape                       >*/
/*<      {                                                                  >*/
/*<        DEFAULT_VALUE:      RFSHAPE_BLOCK;                                  >*/
/*<        RANGE:              RFSHAPE_BLOCK,                                  >*/
```

```
/*<                          RFSHAPE_SG_300_100_0,                    >*/
/*<                          RFSHAPE_REST_2,                          >*/
/*<                          RFSHAPE_HYPSEC,                          >*/
/*<                          RFSHAPE_HS_500_400_100;                        >*/
/*<       NAME_TAG:                "XNIMTC009";                             >*/
/*<       HELP_TAG:                "XHIMTC009";                             >*/
/*<    }                                                          >*/

/*<    PARAMETER float EX_MTC_pulse_angle     >*/
/*<    {                                                          >*/
/*<       MULTIPAGE;                                                  >*/
/*<       RANGE:             0.0 - 1800.0;                        >*/
/*<       DEFAULT_VALUE:        90.;                              >*/
/*<       ADJUST_VALUE: 10.0;                                     >*/
/*<       NAME_TAG:                "XNIMTC010";                             >*/
/*<       HELP_TAG:                "XHIMTC010";                             >*/
/*<    }                                                          >*/

/*<    PARAMETER float EX_MTC_pulse_dur    >*/
/*<    {                                                          >*/
/*<       MULTIPAGE;                                                  >*/
/*<       RANGE:             0.01 - 50.0;                         >*/
/*<       DEFAULT_VALUE:        0.5;                              >*/
/*<       ADJUST_VALUE: 1.0;                                      >*/
/*<       NAME_TAG:                "XNIMTC011";                             >*/
/*<       HELP_TAG:                "XHIMTC011";                             >*/
/*<    }

/*<    PARAMETER float EX_MTC_pulse_phase   >*/
/*<    {                                                          >*/
/*<       MULTIPAGE;                                                  >*/
/*<       RANGE:             -180.0 - 180.0;                      >*/
/*<       DEFAULT_VALUE:        0.;                                  >*/
/*<       ADJUST_VALUE: 10.0;                                     >*/
/*<       NAME_TAG:                "XNIMTC012";                             >*/
/*<       HELP_TAG:                "XHIMTC012";                             >*/
/*<    }                                                          >*/ // yao ding end

/*[      GOAL_PAR_FORM_DEFGROUP_END                                  ]*/

/*-------------------------------------------------------------------*/
/* IEX_MTC PARAMETER GROUPS                                          */
/*-------------------------------------------------------------------*/
```

```
/*<      PARAMETER_GROUP IEX_MTC_all_pars                                  >*/
/*<      {                                                          >*/
/*-------------------------------------------------------------------*/
/* This group is used for database and display order.          */
/* This group contains all mtc parameters.                    */
/*-------------------------------------------------------------------*/
/*<        ID: 10107;                                               >*/
/*<        PARAMETER EX_MTC_enable;                                    >*/
/*<        PARAMETER EX_MTC_sos;                                       >*/
/*<        PARAMETER EX_MTC_IR_base_enable;                                >*/
/*<        PARAMETER EX_MTC_off_res_mp_nr_reps;                  >*/
/*<        PARAMETER EX_MTC_off_res_mp_angle;                          >*/
/*<        PARAMETER EX_MTC_off_res_mp_dur;                            >*/
/*<        PARAMETER EX_MTC_off_res_mp_freq;                           >*/    //yao
ding start
/*<        PARAMETER EX_MTC_delay_time;                                >*/
/*<        PARAMETER EX_MTC_pulse_shape;                               >*/
/*<        PARAMETER EX_MTC_pulse_angle;                               >*/
/*<        PARAMETER EX_MTC_pulse_dur;                                    >*/
/*<        PARAMETER EX_MTC_pulse_phase;                               >*/
/*<      }                                                          >*/  //yao ding end

/*=================================================================
=====*/
/*       UGN1_MTC   I N T E R F A C E     D E F I N I T I O N            */
/*=================================================================
=====*/
/*[      GOAL_PAR_FORM_DEFGROUP   MPIMTC_GN1                                ]*/

/*<      PARAMETER MPU_MTC_MODE_ENUM UGN1_MTC_enable                    >*/
/*<      {                                                          >*/
/*<        DEFAULT_VALUE:        MPU_MTC_MODE_NO;
       >*/
/*<      }                                                          >*/

/*<      PARAMETER MGG_YESNO_ENUM UGN1_MTC_ir_base_enable               >*/
/*<      {                                                          >*/
/*<        DEFAULT_VALUE:        NO;                                     >*/
/*<      }                                                          >*/

/*<      PARAMETER MGG_YESNO_ENUM UGN1_MTC_sos                          >*/
/*<      {                                                          >*/
/*<        DEFAULT_VALUE:        NO;                                     >*/
```

```
/*<     }                                                    >*/

/*<     PARAMETER int UGN1_MTC_off_res_mp_nr_reps                    >*/
/*<     {                                                    >*/
/*<       DEFAULT_VALUE:       8;                            >*/
/*<     }                                                    >*/

/*<     PARAMETER int UGN1_MTC_off_res_mp_angle                  >*/
/*<     {                                                    >*/
/*<       DEFAULT_VALUE:       800;                          >*/
/*<     }                                                    >*/

/*<     PARAMETER int UGN1_MTC_off_res_mp_dur                    >*/
/*<     {                                                    >*/
/*<       DEFAULT_VALUE:       20;                           >*/
/*<     }                                                    >*/

/*<     PARAMETER int UGN1_MTC_off_res_mp_freq                   >*/
/*<     {                                                    >*/
/*<       DEFAULT_VALUE:       500;                          >*/
/*<     }                                                    >*/
//yao ding start
/*<     PARAMETER float UGN1_MTC_delay_time                      >*/
/*<     {                                                    >*/
/*<       DEFAULT_VALUE:       100.;                         >*/
/*<     }                                                    >*/

/*<     PARAMETER float UGN1_MTC_pulse_shape                     >*/  /*<     {
                                                          >*/
/*<       DEFAULT_VALUE:       RFSHAPE_BLOCK;                                >*/
/*<     }                                                    >*/

/*<     PARAMETER float UGN1_MTC_pulse_angle                     >*/
/*<     {                                                    >*/
/*<       DEFAULT_VALUE:       90.;                          >*/
/*<     }                                                    >*/

/*<     PARAMETER float UGN1_MTC_pulse_dur                       >*/
/*<     {                                                    >*/
/*<       DEFAULT_VALUE:       0.5;                          >*/
/*<     }                                                    >*/

/*<     PARAMETER float UGN1_MTC_pulse_phase                     >*/
```

```
/*<      {                                                       >*/
/*<        DEFAULT_VALUE:        0.;                                 >*/
/*<      }                                                       >*/  //yao ding end
/*[      GOAL_PAR_FORM_DEFGROUP_END                                    ]*/

/*<      PARAMETER_GROUP UGN1_MTC_all_pars                             >*/
/*<      {                                                       >*/
/*----------------------------------------------------------------*/
/* This group contains all UGN1_MTC parameters.                  */
/*----------------------------------------------------------------*/
/*<        ID: 10012;                                            >*/
/*<        PARAMETER UGN1_MTC_enable;                                  >*/
/*<        PARAMETER UGN1_MTC_ir_base_enable;                          >*/
/*<        PARAMETER UGN1_MTC_sos;                                 >*/
/*<        PARAMETER UGN1_MTC_off_res_mp_nr_reps;                    >*/
/*<        PARAMETER UGN1_MTC_off_res_mp_angle;                    >*/
/*<        PARAMETER UGN1_MTC_off_res_mp_dur;                          >*/
/*<        PARAMETER UGN1_MTC_off_res_mp_freq;                         >*/    //yao
ding begin
/*<        PARAMETER UGN1_MTC_delay_time;                          >*/
/*<        PARAMETER UGN1_MTC_pulse_shape;                             >*/
/*<        PARAMETER UGN1_MTC_pulse_angle;                             >*/
/*<        PARAMETER UGN1_MTC_pulse_dur;                           >*/
/*<        PARAMETER UGN1_MTC_pulse_phase;                             >*/
/*<      }                                                       >*/  //yao ding end


#endif  /* MPUMTCRCD_H                                                */
/*=============================================================
=====*/
/*       H I S T O R Y                                          */
/*=============================================================
=====*/
/*IGRAB: MSWE::PALSTRA 95-03-30 10:40 for release ASWT5X2             */
```

```
/*=============================================================================*/
/*                                                                             */
/*       SOURCE_FILE:       MPUMTC__G.C                                        */
/*       PACKAGE:    IMTC                                                      */
/*       COMPONENT:         METHPDF                                            */
/*       SOFTWARE LAYER: 1320                                                  */
/*                                                                             */
/*       Copyright 1995: Philips Electronics N.V..                             */
/*=============================================================================*/
/*=============================================================================*/
/*       I N C L U D E S                                                       */
/*=============================================================================*/
/*MPF:::IMTC::MPUMTC__G.C:MPUMTC_val1=========================================*/
/*                                                                             */
/*  FUNCTION NAME:       MPUMTC_val1                                           */
/*  PACKAGE:             IMTC                                                  */
/*  SCOPE:               IMA                                                   */
/*  DESCRIPTION:                                                               */
/*       This function performs validation phase 1.                            */
/*  CALLING SEQUENCE:                                                          */
void            MPUMTC_val1( void)
/*EMP==========================================================================*/
{
OSTRC_info( &export_cpp, "MPUMTC_val1()");

/*-----------------------------------------------------------------*/
/* Init for display                                                */
/*-----------------------------------------------------------------*/
GRP`UGN1_MTC_all_pars:init();
GRP`IEX_MTC_all_pars:disable();

/*-----------------------------------------------------------------*/
/* Start with enable for display                                   */
/*-----------------------------------------------------------------*/
if (`UGN1_ACQ_scan_type == MGUACQ_SCT_IMAGING)
{
PAR`EX_MTC_enable:enable();
```

```
`UGN1_MTC_enable = `EX_MTC_enable;
}
// yao ding begin
if (`UGN1_MTC_enable != MPU_MTC_MODE_NO )
{
PAR`EX_MTC_delay_time:enable();
`UGN1_MTC_delay_time =`EX_MTC_delay_time;
PAR`EX_MTC_pulse_shape:enable();
`UGN1_MTC_pulse_shape =`EX_MTC_pulse_shape;

PAR`EX_MTC_pulse_angle:enable();
`UGN1_MTC_pulse_angle =`EX_MTC_pulse_angle;

PAR`EX_MTC_pulse_dur:enable();
`UGN1_MTC_pulse_dur =`EX_MTC_pulse_dur;

PAR`EX_MTC_pulse_phase:enable();
`UGN1_MTC_pulse_phase =`EX_MTC_pulse_phase;
}               //yao ding end

if ((`EX_ACQ_imaging_sequence == MGUACQ_SEQ_IR) || (`EX_ACQ_imaging_sequence
== MGUACQ_SEQ_MIXED))
{
if (`UGN1_MTC_enable != MPU_MTC_MODE_NO)
{
PAR`EX_MTC_IR_base_enable:enable();
`UGN1_MTC_ir_base_enable = `EX_MTC_IR_base_enable;
}
if (`HW_main_magnetic_field_mT == 1500)
{
PAR`EX_MTC_sos:enable();
`UGN1_MTC_sos = `EX_MTC_sos;
}
}

// Multi pulse MTC for coronary vein imaging
if (`UGN1_MTC_enable == MPU_MTC_MODE_OFF_RES_MULTI_PULSE)
{
PAR`EX_MTC_off_res_mp_nr_reps:enable();
`UGN1_MTC_off_res_mp_nr_reps = `EX_MTC_off_res_mp_nr_reps;
PAR`EX_MTC_off_res_mp_angle:enable();
`UGN1_MTC_off_res_mp_angle = `EX_MTC_off_res_mp_angle;
PAR`EX_MTC_off_res_mp_dur:enable();
```

```
`UGN1_MTC_off_res_mp_dur = `EX_MTC_off_res_mp_dur;
PAR`EX_MTC_off_res_mp_freq:enable();
`UGN1_MTC_off_res_mp_freq = `EX_MTC_off_res_mp_freq;
}
/*----------------------------------------------------------------*/
/* Enable and check only parameters for delayed recon and ima prod.       */
/*----------------------------------------------------------------*/
if ((`UGN_cur_basic_func == MPU_CBFU_DELREC) ||
(`UGN_cur_basic_func == MPU_CBFU_DELIMP))
{
GRP`IEX_MTC_all_pars:disable();
}
}


/*================================================================
=====*/
/*      umtc_set_rf_attrs_for_mtc                                 */
/*                                                                */
/*  DESCRIPTION:                                                  */
/*      Set a number of attributes of the RF`mtc object specifically */
/*      for the application of mtc. This in contrast to the       */
/*      application of sos (silicone only)                        */
/*      These attributes are:                                     */
/*      function, shape, comp_elements, angle, dur, phase, pause, freq      */
/*      Those attributes from this list that are not assigned are */
/*      supposed to get the default value.                        */
/*================================================================
=====*/
static void     umtc_set_rf_attrs_for_mtc(
BOOLEAN     spectro_head_coil,          /* IN: coil                    */
BOOLEAN     normal_head_coil,           /* IN: coil                    */
float    scale_factor)
{
static const float min_comp_dur = 0.25;             /* msec          */
static const float infinit_BW = 9999999.999;/* Hz          */

OSTRC_info( &local, "umtc_set_rf_attrs_for_mtc()");
RF`mtc:nucleus = `UGN1_ACQ_nucleus;
RF`mtc:gamma = `UGN1_ACQ_gamma;
RF`mtc:function = MGOBJRF_FUNCTION_EXCITATION;
switch (`UGN1_MTC_enable)
{
```

```
case MPU_MTC_MODE_ON_RES:
/*-------------------------------------------------------------*/
/*        fixed 121 composite on-resonance pulse               */
/*-------------------------------------------------------------*/
RF`mtc:shape = RFSHAPE_BLOCK;
RF`mtc:comp_elements = 1;  /* fake 1 element for set_min_dur*/
RF`mtc:[ 0 ]:angle = 90.;
RF`mtc:[ 0 ]:set_min_dur( infinit_BW, `UGN2_COIL_possible_B1 );
RF`mtc:[ 0 ]:dur = MAX( RF`mtc:[ 0 ]:dur, min_comp_dur );
RF`mtc:[ 0 ]:dur = RF`mtc:[ 0 ]:dur * scale_factor;
RF`mtc:comp_elements = 3;  /* now set 3 elements           */
RF`mtc:[ 1 ]:angle = 180.;
RF`mtc:[ 2 ]:angle = 90.;
RF`mtc:[ 1 ]:dur = 2 * RF`mtc:[ 0 ]:dur;
RF`mtc:[ 2 ]:dur = RF`mtc:[ 0 ]:dur;
RF`mtc:[ 0 ]:phase = 0.;
RF`mtc:[ 1 ]:phase = 180.;
RF`mtc:[ 2 ]:phase = 0.;
RF`mtc:[ 0 ]:pause = 0.;
RF`mtc:[ 1 ]:pause = 0.;
RF`mtc:[ 2 ]:pause = 0.;
RF`mtc:freq = 0.;
break;
case MPU_MTC_MODE_OFF_RES:
/*-------------------------------------------------------------*/
/*        sinc-gauss off-resonance pulse.                      */
/*        max BW 400 Hz, corresponding to minimum duration of  */
/*        15 ms.                                               */
/*-------------------------------------------------------------*/
RF`mtc:function = MGOBJRF_FUNCTION_INVERSION;
RF`mtc:comp_elements = 1;
RF`mtc:shape  =  `UGN1_MTC_pulse_shape;                                  //yao  ding
`UGN1_MTC_pulse_shape (RFSHAPE_HS_500_400_100) -> RFSHAPE_SG_300_100_0
/*-------------------------------------------------------------*/
/* angle choice depends on SAR limits                          */
/*-------------------------------------------------------------*/
switch (`HW_main_magnetic_field_mT)
{
case 500:
case 1000:
if (AWASW_main_system_type() == AWASW_MST_P10)
{
/*-----------------------------------------------------*/
```

```
/* Panorama 1.0 T: more stringent local SAR limitations */
/* Avoid very long TR's by using a lower flip angle     */
/*------------------------------------------------------*/
RF`mtc:[ 0 ]:angle = 520.;
} else
{
/*------------------------------------------------------*/
/* The original value for the Intera T10                */
/*------------------------------------------------------*/
RF`mtc:[ 0 ]:angle = 1040.;
}
break;
case 1500:
case 3000:
case 7000:
if (spectro_head_coil)
{
RF`mtc:[  0  ]:angle  =  `UGN1_MTC_pulse_angle;                          //yao  ding
`UGN1_MTC_pulse_angle(750) -> 700
} else if (normal_head_coil)
{
RF`mtc:[  0  ]:angle  =  `UGN1_MTC_pulse_angle;                          //yao  ding
`UGN1_MTC_pulse_angle(750) -> 620
} else   /* all other coils                                  */
{
RF`mtc:[  0  ]:angle  =  `UGN1_MTC_pulse_angle;                          //yao  ding
`UGN1_MTC_pulse_angle(750) -> 520
}
break;
default:
MAOBJ_ENUM_OUT_OF_RANGE_ERR();
break;
}//yao ding begin
//RF`mtc:[ 0 ]:set_min_dur( infinit_BW, `UGN_min_of_all_max_B1 );   // at the beginning
RF`mtc:[  0  ]:dur  =  `UGN1_MTC_pulse_dur;              `UGN1_MTC_pulse_dur(10.99)  ->
RF`mtc:[ 0 ]:dur * scale_factor
RF`mtc:[  0  ]:phase = `UGN1_MTC_pulse_phase;          `UGN1_MTC_pulse_phase adding
the line
RF`mtc:freq = 0.;            //yao ding end   0. -> 1100.
break;
case MPU_MTC_MODE_OFF_RES_MULTI_PULSE:
/*------------------------------------------------------------*/
/*        sinc-gauss off-resonance pulse.                     */
```

```
/*-------------------------------------------------------------*/
RF`mtc:function = MGOBJRF_FUNCTION_INVERSION;
RF`mtc:comp_elements = 1;
RF`mtc:shape = RFSHAPE_SG_300_100_0;
RF`mtc:repetitions = `UGN1_MTC_off_res_mp_nr_reps;
RF`mtc:freq = `UGN1_MTC_off_res_mp_freq;
RF`mtc:[ ALL ]:angle = `UGN1_MTC_off_res_mp_angle;
RF`mtc:[ ALL ]:dur = `UGN1_MTC_off_res_mp_dur * scale_factor;
break;
default:
MAOBJ_ENUM_OUT_OF_RANGE_ERR();
break;
}
}

/*=============================================================
=====*/
/*      umtc_set_rf_attrs_for_sos                              */
/*                                                             */
/*  DESCRIPTION:                                               */
/*      Set a number of attributes of the RF`mtc object for the        */
/*      application of sos (silicone only sequence).           */
/*      These attributes are:                                  */
/*      function, shape, comp_elements, angle, dur, phase, pause, freq     */
/*      Those attributes from this list that are not assigned are      */
/*      supposed to get the default value.                     */
/*=============================================================
=====*/
static void       umtc_set_rf_attrs_for_sos( void)
{
float    pulse_max_B1 = 0.;
float    unit_dur = 0.07;
int              i;

......

RF`mtc:[ 2 ]:pause = 1.61;
RF`mtc:freq = -286.;
}

/*=============================================================
=====*/
/*  umtc_compute_sq                                            */
```

```
/*==========================================================================*/
static void                umtc_compute_sq(
double Tpre_next_seq,                  /*In:  time dur. from the end of the    */
/*     MTC sequ. to the magn. center of        */
/*     the exc. pulse                  */
double scale_factor,           /*In:  scale factor for RF`mtc:dur      */
int       sor_prepulses_id)       /*In:  SOR in which to place SQ`mtc */
/*EMP=======================================================================*/
{
static const float wait_time = 0.1;                    /* msec                 */
static const float mtc_deph_cycles = 4.0;              /* cycles        */

......

SQ`mtc:dur = SQ`mtc:ref + trail;

SOR`( sor_prepulses_id ):add_in_front( SQ`mtc, 1);
}

/*MPF:::IMTC::MPUMTC__G.C:MPUMTC_update_IMP=============================*/
/*                                                                       */
/*  FUNCTION NAME:       MPUMTC_update_IMP                                */
/*  PACKAGE:             IMTC                                             */
/*  SCOPE:               IMA                                              */
/*  DESCRIPTION:                                                          */
/*       Update the IMP_MTC parameters                                    */
/*  CALLING SEQUENCE:                                                     */

void               MPUMTC_update_IMP( void)
/*EMP=======================================================================*/
{
if (`UGN1_MTC_enable != MPU_MTC_MODE_NO)
{
`MP_mtc = YES;
}
`MP_mtc_IR_base_enable = `UGN1_MTC_ir_base_enable;
}
```

```
/*=================================================================
=====*/
/*       H I S T O R Y                                             */
/*=================================================================
=====*/
/*Yao Ding (ddyy)::interleaved BOLD and TOLD sequence                */
```

```
/*=============================================================================*/
/*                                                                             */
/*       SOURCE_FILE:       MMIFFE.MXGC                                        */
/*       PACKAGE:   IFFE                                                       */
/*       COMPONENT:         METHMPF                                            */
/*                                                                             */
/*       Copyright 1995: Philips Electronics N.V..                             */
/*                                                                             */
/*=============================================================================*/
/*=============================================================================*/
/*       I N C L U D E S                                                       */
/*=============================================================================*/
#include <math.h>
#include "infra/iosinterface/oslanguage.h"
#include "infra/isuperglo/sgmath.h"
#include "infra/isyslib/stdio.h"

.....



/*-----------------------------------------------------------------*/
/*       Loop over dynamic scans                                   */
/*-----------------------------------------------------------------*/
iffe_continue = TRUE;
iffe_dummy_dynamic_scan = 0;    /* iffe_dynamic_scan initialized earlier */
iffe_ext_dev_state_ix = 0;
while ( iffe_continue &&
(`MPPR_scan_enable == YES) &&
((`MP_dyn_interactive == YES ) ||
(iffe_dynamic_scan < end_dyna_scan)))
{
if ((`MP_EX_dynamic_study == YES) &&
(iffe_dynamic_scan == end_dyna_scan - 1))
{
if ((`CSC_dyn_noise_scan == MGUCSC_NOISE_NO_RF) ||
(`CSC_dyn_noise_scan == MGUCSC_NOISE_NO_RFGR))
{
RF`:disable();
```

```
}
if ((`CSC_dyn_noise_scan == MGUCSC_NOISE_NO_GR) ||
(`CSC_dyn_noise_scan == MGUCSC_NOISE_NO_RFGR))
{
GR`:disable();
}
}

int       resp_hold = 0;
int       outer_package_loop_cntr = 0;          /* counter for outer package loop */
int       first_loc_ix;
BOOLEAN image_acq_complete =
((iffe_dynamic_scan+1) % `MP_DYN_recon_multiplier) == 0;
BOOLEAN prev_dyn_keyhole_reduced_scan = FALSE;
BOOLEAN dyn_keyhole_reduced_scan = FALSE;

if (image_acq_complete)
{
// Moved XTC loop to first in dynamic loop instead of last to avoid scanning one
// unnecessary dynamic to get info. Only downside is that we need to break to handle
// while loop correctly if iffe_continue is false
MMIIA_xtc_loop( iffe_dynamic_scan, &iffe_continue, iffe_steady_state_period ==
IFFE_SSP_SCAN);
if (iffe_continue == FALSE)
{
break;
}
}

if (`MP_dyn_keyh_enable == YES)
{
dyn_keyhole_reduced_scan = MMUGN_dyn_keyhole_reduced_scan( iffe_dynamic_scan);
if (iffe_dynamic_scan > 0)
{
prev_dyn_keyhole_reduced_scan          =          MMUGN_dyn_keyhole_reduced_scan(
iffe_dynamic_scan - 1);
}
}

for (int dyn = 0; dyn < MAOBJVAR_MAX_PROTO_DYN; dyn++)
{
VAR`proto_dyn[ dyn ]:assign( iffe_dynamic_scan);
}
```

```
if (iffe_dummy_dynamic_scan == `MP_nr_dummy_dynamic_scans)
{
iffe_performing_dummy_scan = FALSE;
} else
{
iffe_performing_dummy_scan = TRUE;
}

GR`s_prep:enable = ON;

/*-------------------------------------------------------------*/
/*      RF`mtc will be ON, unless this is the first dynamic    */
/*      scan of an "mtc dynamic" experiment.                   */
/*      (kernel does not switch RF`mtc, as may happen in irfe) */
/*-------------------------------------------------------------*/
RF`mtc:enable = ON;
if ((`MP_dyn_mtc_enable == YES) && (IS_ODD(iffe_dynamic_scan)))          //yao ding
iffe_dynamic_scan == 0 -> IS_ODD(iffe_dynamic_scan)
{
RF`mtc:enable = OFF;
}
/*-------------------------------------------------------------*/
/*      RF`repp will be ON, unless this is the first dynamic   */
/*      scan of an "repp dynamic" experiment.                  */
/*      (kernel does not switch RF`repp, as may happen in irfe)*/
/*-------------------------------------------------------------*/
RF`repp:enable = ON;
if ((`MP_dyn_repp_enable == YES) && (IS_EVEN(iffe_dynamic_scan)))          //yao ding
iffe_dynamic_scan == 0 -> IS_EVEN(iffe_dynamic_scan)
{
RF`repp:enable = OFF;
}

/*-------------------------------------------------------------*/
/*      RF shimming set to "calibrate" implies B1 mapping,     */
/*  in a dynamic scan where we cycle through channels.         */
/*-------------------------------------------------------------*/
if (`MP_DYN_rf_shim_calibrate == YES)
{
int bitmask_multix_one = ( 1 << iffe_dynamic_scan );

RF`ex:bitmask_multix = bitmask_multix_one;
// cycle through each channel individually
```

```
// alternatively, cycle through "all channels except one" by:
// int bitmask_multix_all = ( 1 << RF`ex:nr_channels ) - 1;
// RF`ex:bitmask_multix = ( ~bitmask_multix_one ) & bitmask_multix_all;
}

if (`MP_EX_dynamic_study == YES)
{
/*-----------------------------------------------------------*/
/*  Dynamic study.                                           */
/*  For dynamic scans 1 - 1023 :                             */
/*  manual start or pause (user defined time) may happen.    */
/*  Dynamic scan 0 is always "shortest" (but then we have    */
/*  just executed the initial manual start).                 */
/*  Send message "Performing dynamic scan x..."              */
/*-----------------------------------------------------------*/
int user_def_dyn_scan = MIN( iffe_dynamic_scan, (MGG_MAX_DYN_SCANS - 1));

if (`MP_dyn_scan_pauses[ user_def_dyn_scan ] == MGUDYN_INTV_MANUAL)
{
MMUGN_dyn_man_start( iffe_dynamic_scan, iffe_update_procedure_cb);
if (user_def_dyn_scan > 0)
{
/*-------------------------------------------------*/
/*  In case of dummy dynamics and manual start, the */
/*  manual start is before the dummy dynamics.      */
/*  Do not assign previous_loc_number to -1 for the */
/*  first user_def_dyn_scan.                        */
/*-------------------------------------------------*/
iffe_previous_loc_number = -1;
}
} else if (`MP_dyn_scan_pauses[ user_def_dyn_scan ] > 0)
{
MMUGN_dyn_pause( user_def_dyn_scan );
iffe_previous_loc_number = -1;
} else
{
/* skip */
}
MMUGN_pro_motion_update(iffe_update_procedure_cb);

int_array[ 0 ] = -1;
if (iffe_performing_dummy_scan)
{
```

```
sprintf( str_array[ 0 ], "%1d", iffe_dummy_dynamic_scan + 1 );
MCUI`:message( "XMIDYN03", 1, int_array, str_array );
} else
{
sprintf( str_array[ 0 ], "%1d", iffe_dynamic_scan + 1 );
MCUI`:message( "XMIDYN02", 1, int_array, str_array );
}
} else
{
/* skip */
}

.....

/*=============================================================================*/
/*        H I S T O R Y                                                        */
/*=============================================================================*/
/*GRAB: MSWE::DEGRAAF 92-05-26 11:37 for release ASWTNAP                       */
/*        Change global variables to static.                                   */

.....

// 2010-04-29 Ulrike Blume for r32
//      MR00095630: correction of the FLL-cycle loop within iffe_tfe_kernel

//2011-11-10 Yao ding added an interleaved function in the dynamic scan.
```

REFERENCES

Aboagye, E. O. and Z. M. Bhujwalla (1999). "Malignant transformation alters membrane choline phospholipid metabolism of human mammary epithelial cells." Cancer Res **59**(1): 80-84.

Allen, J. R., R. W. Prost, et al. (2001). "In vivo proton (H1) magnetic resonance spectroscopy for cervical carcinoma." Am J Clin Oncol **24**(5): 522-529.

Altenberg, B. and K. O. Greulich (2004). "Genes of glycolysis are ubiquitously overexpressed in 24 cancer classes." Genomics **84**(6): 1014-1020.

Baik, H. M., M. Y. Su, et al. (2006). "Quantification of choline-containing compounds in malignant breast tumors by 1H MR spectroscopy using water as an internal reference at 1.5 T." MAGMA **19**(2): 96-104.

Bansal, A., R. A. Harris, et al. (2012). "Choline phosphorylation and regulation of transcription of choline kinase alpha in hypoxia." J Lipid Res **53**(1): 149-157.

Bartrons, R. and J. Caro (2007). "Hypoxia, glucose metabolism and the Warburg's effect." J Bioenerg Biomembr **39**(3): 223-229.

Baudelet, C., G. O. Cron, et al. (2006). "Determination of the maturity and functionality of tumor vasculature by MRI: correlation between BOLD-MRI and DCE-MRI using P792 in experimental fibrosarcoma tumors." Magn Reson Med **56**(5): 1041-1049.

Baudelet, C. and B. Gallez (2002). "How does blood oxygen level-dependent (BOLD) contrast correlate with oxygen partial pressure (pO2) inside tumors?" Magn Reson Med **48**(6): 980-986.

Bindra, R. S., M. E. Crosby, et al. (2007). "Regulation of DNA repair in hypoxic cancer cells." Cancer Metastasis Rev **26**(2): 249-260.

Bland, J. M. and D. G. Altman (1986). "Statistical methods for assessing agreement between two methods of clinical measurement." Lancet **1**(8476): 307-310.

Bolan, P. J., S. Meisamy, et al. (2003). "In vivo quantification of choline compounds in the breast with 1H MR spectroscopy." Magn Reson Med **50**(6): 1134-1143.

Booth, S. J., M. D. Pickles, et al. (2009). "In vivo magnetic resonance spectroscopy of gynaecological tumours at 3.0 Tesla." BJOG **116**(2): 300-303.

Boss, A., P. Martirosian, et al. (2009). "Influence of oxygen and carbogen breathing on renal oxygenation measured by T2*-weighted imaging at 3.0 T." NMR Biomed **22**(6): 638-645.

Bottomley, P. A. (1987). "Spatial localization in NMR spectroscopy in vivo." Ann N Y Acad Sci **508**: 333-348.

Brizel, D. M., G. S. Sibley, et al. (1997). "Tumor hypoxia adversely affects the prognosis of carcinoma of the head and neck." Int J Radiat Oncol Biol Phys **38**(2): 285-289.

Brown, J. M. and W. R. Wilson (2004). "Exploiting tumour hypoxia in cancer treatment." Nat Rev Cancer **4**(6): 437-447.

Brune, B. and J. Zhou (2003). "The role of nitric oxide (NO) in stability regulation of hypoxia inducible factor-1alpha (HIF-1alpha)." Curr Med Chem **10**(10): 845-855.

Carmeliet, P., Y. Dor, et al. (1998). "Role of HIF-1alpha in hypoxia-mediated apoptosis, cell proliferation and tumour angiogenesis." Nature **394**(6692): 485-490.

Cavassila, S., S. Deval, et al. (2001). "Cramer-Rao bounds: an evaluation tool for quantitation." NMR Biomed **14**(4): 278-283.
Chen, C., N. Pore, et al. (2001). "Regulation of glut1 mRNA by hypoxia-inducible factor-1. Interaction between H-ras and hypoxia." J Biol Chem **276**(12): 9519-9525.
Chen, Q., P. M. Jakob, et al. (1998). "Oxygen enhanced MR ventilation imaging of the lung." MAGMA **7**(3): 153-161.
Cheng, H. L. and G. A. Wright (2006). "Rapid high-resolution T(1) mapping by variable flip angles: accurate and precise measurements in the presence of radiofrequency field inhomogeneity." Magn Reson Med **55**(3): 566-574.
Cho, S. G., D. H. Lee, et al. (2005). "Differentiation of chronic focal pancreatitis from pancreatic carcinoma by in vivo proton magnetic resonance spectroscopy." J Comput Assist Tomogr **29**(2): 163-169.
Cohen, M. S. and R. M. Weisskoff (1991). "Ultra-fast imaging." Magnetic Resonance Imaging **9**(1): 1-37.
Davda, S. and T. Bezabeh (2006). "Advances in methods for assessing tumor hypoxia in vivo: implications for treatment planning." Cancer Metastasis Rev **25**(3): 469-480.
de Bazelaire, C. M., G. D. Duhamel, et al. (2004). "MR imaging relaxation times of abdominal and pelvic tissues measured in vivo at 3.0 T: preliminary results." Radiology **230**(3): 652-659.
Del Sole, A., A. Falini, et al. (2001). "Anatomical and biochemical investigation of primary brain tumours." Eur J Nucl Med **28**(12): 1851-1872.
Deoni, S. C., B. K. Rutt, et al. (2003). "Rapid combined T1 and T2 mapping using gradient recalled acquisition in the steady state." Magn Reson Med **49**(3): 515-526.
deSouza, N. M., W. P. Soutter, et al. (2004). "Use of neoadjuvant chemotherapy prior to radical hysterectomy in cervical cancer: monitoring tumour shrinkage and molecular profile on magnetic resonance and assessment of 3-year outcome." Br J Cancer **90**(12): 2326-2331.
Doran, S. T., G. L. Falk, et al. (2003). "Pathology of Barrett's esophagus by proton magnetic resonance spectroscopy and a statistical classification strategy." Am J Surg **185**(3): 232-238.
Evans, S. M. and C. J. Koch (2003). "Prognostic significance of tumor oxygenation in humans." Cancer Lett **195**(1): 1-16.
Farzaneh, F., S. J. Riederer, et al. (1990). "Analysis of T2 limitations and off-resonance effects on spatial resolution and artifacts in echo-planar imaging." Magn Reson Med **14**(1): 123-139.
Fatouros, P. P., D. L. Heath, et al. (2000). "Comparison of NAA measures by MRS and HPLC." Brain Edema Xi **76**: 35-37.
Fayad, L. M., D. A. Bluemke, et al. (2006). "Musculoskeletal tumors: use of proton MR spectroscopic imaging for characterization." J Magn Reson Imaging **23**(1): 23-28.
Fayad, L. M., X. Wang, et al. (2010). "A feasibility study of quantitative molecular characterization of musculoskeletal lesions by proton MR spectroscopy at 3 T." AJR Am J Roentgenol **195**(1): W69-75.

Feinberg, D. A., R. Turner, et al. (1990). "Echo-planar imaging with asymmetric gradient modulation and inner-volume excitation." Magn Reson Med **13**(1): 162-169.
Feldser, D., F. Agani, et al. (1999). "Reciprocal positive regulation of hypoxia-inducible factor 1alpha and insulin-like growth factor 2." Cancer Res **59**(16): 3915-3918.
Fukumura, D. and R. K. Jain (2007). "Tumor microvasculature and microenvironment: targets for anti-angiogenesis and normalization." Microvasc Res **74**(2-3): 72-84.
Fyles, A., M. Milosevic, et al. (2002). "Tumor hypoxia has independent predictor impact only in patients with node-negative cervix cancer." J Clin Oncol **20**(3): 680-687.
Garcia-Eulate, R., D. Garcia-Garcia, et al. (2011). "Functional bold MRI: advantages of the 3 T vs. the 1.5 T." Clin Imaging **35**(3): 236-241.
Geethanath, S., H. M. Baek, et al. (2012). "Compressive Sensing Could Accelerate H-1 MR Metabolic Imaging in the Clinic." Radiology **262**(3): 985-994.
Glover, G. H. (2011). "Overview of functional magnetic resonance imaging." Neurosurg Clin N Am **22**(2): 133-139, vii.
Gluch, L. (2005). "Magnetic resonance in surgical oncology: II - literature review." ANZ J Surg **75**(6): 464-470.
Glunde, K., C. Jie, et al. (2004). "Molecular causes of the aberrant choline phospholipid metabolism in breast cancer." Cancer Res **64**(12): 4270-4276.
Gorski, D. H., M. A. Beckett, et al. (1999). "Blockage of the vascular endothelial growth factor stress response increases the antitumor effects of ionizing radiation." Cancer Res **59**(14): 3374-3378.
Gowland, P. and P. Mansfield (1993). "Accurate measurement of T1 in vivo in less than 3 seconds using echo-planar imaging." Magn Reson Med **30**(3): 351-354.
Gribbestad, I. S., H. E. Fjosne, et al. (1993). "In vitro proton NMR spectroscopy of extracts from human breast tumours and non-involved breast tissue." Anticancer Res **13**(6A): 1973-1980.
Gribbestad, I. S., B. Sitter, et al. (1999). "Metabolite composition in breast tumors examined by proton nuclear magnetic resonance spectroscopy." Anticancer Res **19**(3A): 1737-1746.
Griffiths, J. R., N. J. Taylor, et al. (1997). "The response of human tumors to carbogen breathing, monitored by Gradient-Recalled Echo Magnetic Resonance Imaging." Int J Radiat Oncol Biol Phys **39**(3): 697-701.
Guthridge, C. J., M. R. Stampfer, et al. (1994). "Phospholipases A2 in ras-transformed and immortalized human mammary epithelial cells." Cancer Lett **86**(1): 11-21.
Haase, A., J. Frahm, et al. (1985). "1H NMR chemical shift selective (CHESS) imaging." Phys Med Biol **30**(4): 341-344.
Haddadin, I. S., A. McIntosh, et al. (2009). "Metabolite quantification and high-field MRS in breast cancer." NMR Biomed **22**(1): 65-76.
Hall, E. J. (1994). Radiobiology for the Radiologist. Philadelphia: Lippincott**:** 133-152.
Hanneman, S. K. (2008). "Design, analysis, and interpretation of method-comparison studies." AACN Adv Crit Care **19**(2): 223-234.

Hara, T., A. Bansal, et al. (2006). "Effect of hypoxia on the uptake of [methyl-3H]choline, [1-14C] acetate and [18F]FDG in cultured prostate cancer cells." Nucl Med Biol **33**(8): 977-984.

Harada, H. and M. Hiraoka (2010). "Hypoxia-Inducible Factor 1 in Tumor Radioresistance." Current Signal Transduction Therapy **5**(3): 188-196.

Harada, H., S. Itasaka, et al. (2009). "Treatment regimen determines whether an HIF-1 inhibitor enhances or inhibits the effect of radiation therapy." Br J Cancer **100**(5): 747-757.

Harada, H., S. Kizaka-Kondoh, et al. (2005). "Optical imaging of tumor hypoxia and evaluation of efficacy of a hypoxia-targeting drug in living animals." Mol Imaging **4**(3): 182-193.

Harris, A. L. (2002). "Hypoxia--a key regulatory factor in tumour growth." Nat Rev Cancer **2**(1): 38-47.

Helms, G. (2000). "A precise and user-independent quantification technique for regional comparison of single volume proton MR spectroscopy of the human brain." NMR Biomed **13**(7): 398-406.

Hennig, J. and H. Friedburg (1988). "Clinical-Applications and Methodological Developments of the Rare Technique." Magnetic Resonance Imaging **6**(4): 391-395.

Hockel, M., K. Schlenger, et al. (1996). "Association between tumor hypoxia and malignant progression in advanced cancer of the uterine cervix." Cancer Res **56**(19): 4509-4515.

Hockel, M., B. Vorndran, et al. (1993). "Tumor oxygenation: a new predictive parameter in locally advanced cancer of the uterine cervix." Gynecol Oncol **51**(2): 141-149.

Howe, F. A., S. P. Robinson, et al. (2001). "Issues in flow and oxygenation dependent contrast (FLOOD) imaging of tumours." NMR Biomed **14**(7-8): 497-506.

Hu, M. and K. Polyak (2008). "Microenvironmental regulation of cancer development." Curr Opin Genet Dev **18**(1): 27-34.

Huang, L. E., J. Gu, et al. (1998). "Regulation of hypoxia-inducible factor 1alpha is mediated by an O2-dependent degradation domain via the ubiquitin-proteasome pathway." Proc Natl Acad Sci U S A **95**(14): 7987-7992.

Jansen, J. F., W. H. Backes, et al. (2006). "1H MR spectroscopy of the brain: absolute quantification of metabolites." Radiology **240**(2): 318-332.

Jezzard, P. and R. S. Balaban (1995). "Correction for geometric distortion in echo planar images from B0 field variations." Magn Reson Med **34**(1): 65-73.

Jones, R. A., M. Ries, et al. (2002). "Imaging the changes in renal T1 induced by the inhalation of pure oxygen: a feasibility study." Magn Reson Med **47**(4): 728-735.

Kastrup, A., G. Kruger, et al. (2001). "Assessment of cerebrovascular reactivity with functional magnetic resonance imaging: comparison of CO(2) and breath holding." Magnetic Resonance Imaging **19**(1): 13-20.

Katz-Brull, R., P. T. Lavin, et al. (2002). "Clinical utility of proton magnetic resonance spectroscopy in characterizing breast lesions." J Natl Cancer Inst **94**(16): 1197-1203.

Kim, J. K., D. Y. Kim, et al. (1998). "In vivo differential diagnosis of prostate cancer and benign prostatic hyperplasia: localized proton magnetic resonance spectroscopy using external-body surface coil." Magnetic Resonance Imaging **16**(10): 1281-1288.

Kreis, R. and C. Boesch (2003). Bad spectra can be better than good spectra. In: Proceedings of the 11th Meeting of the International Society for Magnetic Resonance in Medicine., Berkeley, Calif.

Krieg, M., R. Haas, et al. (2000). "Up-regulation of hypoxia-inducible factors HIF-1alpha and HIF-2alpha under normoxic conditions in renal carcinoma cells by von Hippel-Lindau tumor suppressor gene loss of function." Oncogene **19**(48): 5435-5443.

Kvistad, K. A., I. J. Bakken, et al. (1999). "Characterization of neoplastic and normal human breast tissues with in vivo (1)H MR spectroscopy." J Magn Reson Imaging **10**(2): 159-164.

Li, D., P. Dhawale, et al. (1996). "Myocardial signal response to dipyridamole and dobutamine: demonstration of the BOLD effect using a double-echo gradient-echo sequence." Magn Reson Med **36**(1): 16-20.

Listerud, J., S. Einstein, et al. (1992). "First principles of fast spin echo." Magn Reson Q **8**(4): 199-244.

Ljungkvist, A. S., J. Bussink, et al. (2007). "Dynamics of tumor hypoxia measured with bioreductive hypoxic cell markers." Radiat Res **167**(2): 127-145.

Longo, R., P. Pollesello, et al. (1995). "Proton MR spectroscopy in quantitative in vivo determination of fat content in human liver steatosis." J Magn Reson Imaging **5**(3): 281-285.

Look, D., Locker, DR. (1970). "Time Saving in Measurement of NMR and EPR Relaxation Times. ." Rev. Scientific Instrum. **41**(2): 2.

Lu, H., R. A. Forbes, et al. (2002). "Hypoxia-inducible factor 1 activation by aerobic glycolysis implicates the Warburg effect in carcinogenesis." J Biol Chem **277**(26): 23111-23115.

Mahon, M. M., I. J. Cox, et al. (2004). "(1)H magnetic resonance spectroscopy of preinvasive and invasive cervical cancer: in vivo-ex vivo profiles and effect of tumor load." J Magn Reson Imaging **19**(3): 356-364.

Mahon, M. M., N. M. deSouza, et al. (2004). "Preinvasive and invasive cervical cancer: an ex vivo proton magic angle spinning magnetic resonance spectroscopy study." NMR Biomed **17**(3): 144-153.

Matsumoto, K., M. Bernardo, et al. (2006). "MR assessment of changes of tumor in response to hyperbaric oxygen treatment." Magn Reson Med **56**(2): 240-246.

Michaely, H. J., L. Metzger, et al. (2012). "Renal BOLD-MRI does not reflect renal function in chronic kidney disease." Kidney Int **81**(7): 684-689.

Miller, K. L., S. M. Smith, et al. (2007). "Signal and noise characteristics of SSFP FMRI: a comparison with GRE at multiple field strengths." Neuroimage **37**(4): 1227-1236.

Moeller, B. J., Y. Cao, et al. (2004). "Radiation activates HIF-1 to regulate vascular radiosensitivity in tumors: role of reoxygenation, free radicals, and stress granules." Cancer Cell **5**(5): 429-441.

Moeller, B. J. and M. W. Dewhirst (2006). "HIF-1 and tumour radiosensitivity." Br J Cancer **95**(1): 1-5.

Mukherji, S. K., S. Schiro, et al. (1997). "Proton MR spectroscopy of squamous cell carcinoma of the extracranial head and neck: in vitro and in vivo studies." AJNR Am J Neuroradiol **18**(6): 1057-1072.

Naressi, A., C. Couturier, et al. (2001). "Java-based graphical user interface for the MRUI quantitation package." Magnetic Resonance Materials in Physics Biology and Medicine **12**(2-3): 141-152.

National Cervial Cancer Coalition http://www.nccc-online.org/.

Negendank, W. G. (1995). "MR spectroscopy of musculoskeletal soft-tissue tumors." Magn Reson Imaging Clin N Am **3**(4): 713-725.

Nestle, N., T. Baumann, et al. (2003). "Oxygen determination in oxygen-supersaturated drinking waters by NMR relaxometry." Water Res **37**(14): 3361-3366.

Neuhaus, D. W., M. (1989). The nuclear Overhauser effect in structural and conformational analysis. New York, VCH.

Noh, D. Y., S. J. Ahn, et al. (2000). "Overexpression of phospholipase D1 in human breast cancer tissues." Cancer Lett **161**(2): 207-214.

Nordsmark, M. and J. Overgaard (2000). "A confirmatory prognostic study on oxygenation status and loco-regional control in advanced head and neck squamous cell carcinoma treated by radiation therapy." Radiother Oncol **57**(1): 39-43.

O'Connor, J. P., A. Jackson, et al. (2007). "Organ-specific effects of oxygen and carbogen gas inhalation on tissue longitudinal relaxation times." Magn Reson Med **58**(3): 490-496.

O'Connor, J. P., J. H. Naish, et al. (2009). "Comparison of normal tissue R1 and R*2 modulation by oxygen and carbogen." Magn Reson Med **61**(1): 75-83.

Ogawa, S., T. M. Lee, et al. (1993). "The sensitivity of magnetic resonance image signals of a rat brain to changes in the cerebral venous blood oxygenation." Magn Reson Med **29**(2): 205-210.

Ogawa, S., T. M. Lee, et al. (1990). "Brain magnetic resonance imaging with contrast dependent on blood oxygenation." Proc Natl Acad Sci U S A **87**(24): 9868-9872.

Ogawa, S., D. W. Tank, et al. (1992). "Intrinsic signal changes accompanying sensory stimulation: functional brain mapping with magnetic resonance imaging." Proc Natl Acad Sci U S A **89**(13): 5951-5955.

Olive, P. L., J. P. Banath, et al. (2001). "Measuring hypoxia in solid tumours--is there a gold standard?" Acta Oncol **40**(8): 917-923.

Pacheco-Torres, J. Z. D., ; Contero A,; Peschke P, and Mason RP (2008). DOCENT-Dynamic Oxygen Challenge Evaluated by NMR T1 and T2* of Tumors. Proc. Intl. Soc. Mag. Reson. Med.: 450.

Padhani, A. (2010). "Science to practice: what does MR oxygenation imaging tell us about human breast cancer hypoxia?" Radiology **254**(1): 1-3.

Posse, S., S. Wiese, et al. (1999). "Enhancement of BOLD-contrast sensitivity by single-shot multi-echo functional MR imaging." Magn Reson Med **42**(1): 87-97.

Powell, M. E., D. R. Collingridge, et al. (1999). "Improvement in human tumour oxygenation with carbogen of varying carbon dioxide concentrations." Radiother Oncol **50**(2): 167-171.

Preibisch, C. and R. Deichmann (2009). "Influence of RF spoiling on the stability and accuracy of T1 mapping based on spoiled FLASH with varying flip angles." Magn Reson Med **61**(1): 125-135.

Preul, M. C., Z. Caramanos, et al. (1996). "Accurate, noninvasive diagnosis of human brain tumors by using proton magnetic resonance spectroscopy." Nat Med **2**(3): 323-325.

Pruessmann, K. P., M. Weiger, et al. (1999). "SENSE: sensitivity encoding for fast MRI." Magn Reson Med **42**(5): 952-962.

Pruijm, M., L. Hofmann, et al. (2010). "Effect of sodium loading/depletion on renal oxygenation in young normotensive and hypertensive men." Hypertension **55**(5): 1116-1122.

Ramirez de Molina, A., A. Rodriguez-Gonzalez, et al. (2004). "From Ras signalling to ChoK inhibitors: a further advance in anticancer drug design." Cancer Lett **206**(2): 137-148.

Rasey, J. S., W. J. Koh, et al. (1996). "Quantifying regional hypoxia in human tumors with positron emission tomography of [18F]fluoromisonidazole: a pretherapy study of 37 patients." Int J Radiat Oncol Biol Phys **36**(2): 417-428.

Recio, F. O., B. I. Sahai Srivastava, et al. (1998). "The clinical value of digene hybrid capture HPV DNA testing in a referral-based population with abnormal pap smears." Eur J Gynaecol Oncol **19**(3): 203-208.

Remmele S, V. T., ; Keupp J,; Stehning C, and Senegas J. (2008). Simultaneous ΔR1 and ΔR2* Quantification in 5s to Monitor Blood and Tissue Oxygenation with Dynamic (C)O2 Enhanced MRI. Proc. Intl. Soc. Mag. Reson. Med: 5121.

Rijpkema, M., J. H. Kaanders, et al. (2002). "Effects of breathing a hyperoxic hypercapnic gas mixture on blood oxygenation and vascularity of head-and-neck tumors as measured by magnetic resonance imaging." Int J Radiat Oncol Biol Phys **53**(5): 1185-1191.

Rodrigues, L. M., F. A. Howe, et al. (2004). "Tumor R2* is a prognostic indicator of acute radiotherapeutic response in rodent tumors." J Magn Reson Imaging **19**(4): 482-488.

Rofstad, E. K., K. Sundfor, et al. (2000). "Hypoxia-induced treatment failure in advanced squamous cell carcinoma of the uterine cervix is primarily due to hypoxia-induced radiation resistance rather than hypoxia-induced metastasis." Br J Cancer **83**(3): 354-359.

Rostrup, E., I. Law, et al. (2000). "Regional differences in the CBF and BOLD responses to hypercapnia: a combined PET and fMRI study." Neuroimage **11**(2): 87-97.

Roth, K., B. Hubesch, et al. (1989). "Noninvasive Quantitation of Phosphorus Metabolites in Human-Tissue by Nmr-Spectroscopy." Journal of Magnetic Resonance **81**(2): 299-311.

Roughton, F. J. and J. W. Severinghaus (1973). "Accurate determination of O2 dissociation curve of human blood above 98.7 percent saturation with data on O2 solubility in unmodified human blood from 0 degrees to 37 degrees C." J Appl Physiol **35**(6): 861-869.

Rudkin, T. M. and D. L. Arnold (1999). "Proton magnetic resonance spectroscopy for the diagnosis and management of cerebral disorders." Arch Neurol **56**(8): 919-926.

Ruiz-Cabello, J. and J. S. Cohen (1992). "Phospholipid metabolites as indicators of cancer cell function." NMR Biomed **5**(5): 226-233.

Sadowski, E. A., S. B. Fain, et al. (2005). "Assessment of acute renal transplant rejection with blood oxygen level-dependent MR imaging: initial experience." Radiology **236**(3): 911-919.

Salceda, S. and J. Caro (1997). "Hypoxia-inducible factor 1alpha (HIF-1alpha) protein is rapidly degraded by the ubiquitin-proteasome system under normoxic conditions. Its stabilization by hypoxia depends on redox-induced changes." J Biol Chem **272**(36): 22642-22647.

Scheffler, K. and S. Lehnhardt (2003). "Principles and applications of balanced SSFP techniques." Eur Radiol **13**(11): 2409-2418.

Seagroves, T. N., H. E. Ryan, et al. (2001). "Transcription factor HIF-1 is a necessary mediator of the pasteur effect in mammalian cells." Mol Cell Biol **21**(10): 3436-3444.

Semenza, G. L. (1999). "Regulation of mammalian O-2 homeostasis by hypoxia- inducible factor 1." Annual Review of Cell and Developmental Biology **15**: 551-578.

Semenza, G. L. and G. L. Wang (1992). "A nuclear factor induced by hypoxia via de novo protein synthesis binds to the human erythropoietin gene enhancer at a site required for transcriptional activation." Mol Cell Biol **12**(12): 5447-5454.

Serganova, I., J. Humm, et al. (2006). "Tumor hypoxia imaging." Clin Cancer Res **12**(18): 5260-5264.

Shah, N., A. Sattar, et al. (2006). "Magnetic resonance spectroscopy as an imaging tool for cancer: a review of the literature." J Am Osteopath Assoc **106**(1): 23-27.

Sidwell, A. E., R. H. Munch, et al. (1938). "The salt effect on the hemoglobin-oxygen equilibrium." Journal of Biological Chemistry **123**(1): 335-350.

Sitter, B., T. Bathen, et al. (2004). "Cervical cancer tissue characterized by high-resolution magic angle spinning MR spectroscopy." MAGMA **16**(4): 174-181.

Slichter, C. (1990). Principles of Magnetic Resonance. . Berlin, Springer-Verlag.

Soher, B. J., R. E. Hurd, et al. (1996). "Quantitation of automated single-voxel proton MRS using cerebral water as an internal reference." Magn Reson Med **36**(3): 335-339.

Star-Lack, J., S. J. Nelson, et al. (1997). "Improved water and lipid suppression for 3D PRESS CSI using RF band selective inversion with gradient dephasing (BASING)." Magn Reson Med **38**(2): 311-321.

Star-Lack, J. M., E. Adalsteinsson, et al. (2000). "In vivo 1H MR spectroscopy of human head and neck lymph node metastasis and comparison with oxygen tension measurements." AJNR Am J Neuroradiol **21**(1): 183-193.

Statistics analysis: T-TEST (http://www.graphpad.com/quickcalcs/ttest1.cfm).

Steen, R. G., S. A. Gronemeyer, et al. (1994). "Precise and accurate measurement of proton T1 in human brain in vivo: validation and preliminary clinical application." J Magn Reson Imaging **4**(5): 681-691.

Swindle, P., S. McCredie, et al. (2003). "Pathologic characterization of human prostate tissue with proton MR spectroscopy." Radiology **228**(1): 144-151.

Tadamura, E., H. Hatabu, et al. (1997). "Effect of oxygen inhalation on relaxation times in various tissues." J Magn Reson Imaging **7**(1): 220-225.

Tatum, J. L., G. J. Kelloff, et al. (2006). "Hypoxia: importance in tumor biology, noninvasive measurement by imaging, and value of its measurement in the management of cancer therapy." Int J Radiat Biol **82**(10): 699-757.

Taylor, N. J., H. Baddeley, et al. (2001). "BOLD MRI of human tumor oxygenation during carbogen breathing." J Magn Reson Imaging **14**(2): 156-163.

Thomlinson, R. H. and L. H. Gray (1955). "The Histological Structure of Some Human Lung Cancers and the Possible Implications for Radiotherapy." British Journal of Cancer **9**(4): 539-&.

Thomlinson, R. H. and L. H. Gray (1955). "The histological structure of some human lung cancers and the possible implications for radiotherapy." Br J Cancer **9**(4): 539-549.

Ting, Y. L., D. Sherr, et al. (1996). "Variations in energy and phospholipid metabolism in normal and cancer human mammary epithelial cells." Anticancer Res **16**(3B): 1381-1388.

Vaupel, P. and A. Mayer (2007). "Hypoxia in cancer: significance and impact on clinical outcome." Cancer Metastasis Rev **26**(2): 225-239.

Venkatesan, R., W. Lin, et al. (1998). "Accurate determination of spin-density and T1 in the presence of RF-field inhomogeneities and flip-angle miscalibration." Magn Reson Med **40**(4): 592-602.

Wakisaka, N. and J. S. Pagano (2003). "Epstein-Barr virus induces invasion and metastasis factors." Anticancer Res **23**(3A): 2133-2138.

Wang, C. K., C. W. Li, et al. (2004). "Characterization of bone and soft-tissue tumors with in vivo 1H MR spectroscopy: initial results." Radiology **232**(2): 599-605.

Wang, G. L., B. H. Jiang, et al. (1995). "Hypoxia-Inducible Factor-1 Is a Basic-Helix-Loop-Helix-Pas Heterodimer Regulated by Cellular O-2 Tension." Proc Natl Acad Sci U S A **92**(12): 5510-5514.

Warburg, O. (1956). "On the origin of cancer cells." Science **123**(3191): 309-314.

Warburg, O. (1956). "Origin of Cancer Cells." Science **123**(3191): 309-314.

West, J. (2005). Respiratory physiology: the essentials. Philadelphia, Lippincott Williams & Wilkins.

Wheeler-Kingshott, C. A., G. J. Parker, et al. (2002). "ADC mapping of the human optic nerve: increased resolution, coverage, and reliability with CSF-suppressed ZOOM-EPI." Magn Reson Med **47**(1): 24-31.

Winter, J. D., M. K. Akens, et al. (2011). "Quantitative MRI assessment of VX2 tumour oxygenation changes in response to hyperoxia and hypercapnia." Phys Med Biol **56**(5): 1225-1242.

Zaharchuk, G., R. F. Busse, et al. (2006). "Noninvasive oxygen partial pressure measurement of human body fluids in vivo using magnetic resonance imaging." Acad Radiol **13**(8): 1016-1024.

Zaharchuk, G., A. J. Martin, et al. (2005). "Measurement of cerebrospinal fluid oxygen partial pressure in humans using MRI." Magn Reson Med **54**(1): 113-121.

Zeng, L., G. Ou, et al. (2008). "TS-1 enhances the effect of radiotherapy by suppressing radiation-induced hypoxia-inducible factor-1 activation and inducing endothelial cell apoptosis." Cancer Sci **99**(11): 2327-2335.

Zhao, D., L. Jiang, et al. (2009). "Comparison of 1H blood oxygen level-dependent (BOLD) and 19F MRI to investigate tumor oxygenation." Magn Reson Med **62**(2): 357-364.
Zhong, H., A. M. De Marzo, et al. (1999). "Overexpression of hypoxia-inducible factor 1 alpha in common human cancers and their metastases." Cancer Research **59**(22): 5830-5835.
Ziyeh, S., J. Rick, et al. (2005). "Blood oxygen level-dependent MRI of cerebral CO2 reactivity in severe carotid stenosis and occlusion." Stroke **36**(4): 751-756.